NANOSTRUCTURED HYDROXYAPATITE AND TRICALCIUM PHOSPHATE BASED CERAMICS FOR BOVINE SERUM ALBUMIN PROTEIN DELIVERY AND BONE IMPLANTS USING MICROWAVE SINTERING

By

SUDIP DASGUPTA

A dissertation submitted in partial fulfillment of

the requirements for the degree of

DOCTOR OF PHILOSOPHY

WASHINGTON STATE UNIVERSITY

Materials Science Program

August 2008

To the Faculty of Washington State University:

The members of the Committee appointed to examine the dissertation of SUDIP DASGUPTA find it satisfactory and recommend that it be accepted.

_____
Chair

_____

_____

_____

ACKNOWLEDGEMENT

I express my sincere thanks and acknowledgements to all those great personalities with whom I have interacted both actively and passively during my entire tenure to pursue my Doctorate of Philosophy (Ph. D.) in Materials Science. My sincere thanks and gratitude goes to my advisor, Dr. Susmita Bose for providing me opportunity to work in her research group. My thanks also go to her for her support and valuable suggestions she gave me throughout my career as a graduate student at Washington State University. Her valuable advices and constructive criticism have motivated me to cater the right path in achieving a set goal.

I convey my sincere thanks to Prof. Amit Bandyopadhyay for his valuable suggestions and guidance during my research work. My heartiest thanks go to Prof. Howard Hosick, who has been kind enough to give me opportunities to use his laboratory at all convenient time to pursue my studies in the field of cell biology. I also want to convey my sincere thanks and gratitude to my other committee members Prof. Kirk Peterson and Prof. Katie Zhong for their valuable suggestions.

I would like to thank the National Science Foundations (NSF) for the financial support under the Presidential CAREER Award for Scientists and Engineers (PECASE) grant to Dr. S. Bose (CTS # 0134476). I would also like to express my sincere gratitude to Dr. Christine Davitt and Dr. Valerie Lynch at Electron Microscopy Center (EMC) and Brena Holman and Jessica Moore at School of Biological Sciences for assisting me in microscopic analysis and cell culture study. I am thankful to all my group members for assisting me in different ways in my academic and research endeavors during the tenure of my Ph.D.

My sincere thank and heartiest gratitude to all my family and friends, for all their inspiration and support in every step of my life. No word is enough to acknowledge the sacrifices and commitments from my beloved mother, Smt. Lakshmi Dasgupta and my wife Mrs Sarmila Dasgupta (Chatterjee) during my entire PhD. I would like to convey my heartiest love to my little daughter, Samadrita, for her constant smile to make my everyday beautiful. Finally, I would like to dedicate this thesis to my late father, Mr. Abinas Dasgupta from whom I learnt the philosophy of life. It was his dream that I reach here and I feel very proud about it.

Thank you once again to all my good friends at Washington State University.

NANOSTRUCTURED HYDROXYAPATITE AND TRICALCIUM PHOSPHATE BASED CERAMICS FOR BOVINE SERUM ALBUMIN PROTEIN DELIVERY AND BONE IMPLANTS USING MICROWAVE SINTERING

Abstract

by, Sudip Dasgupta, Ph. D.

Washington State University

August, 2008

Chair: Susmita Bose

The objective of this study was to investigate the potential of nanocrystalline hydroxyapatite [$Ca_{10}(PO_4)_6(OH)_2$, HA] and β-tricalcium phosphate [β-$Ca_3(PO_4)_2$, β-TCP] for controlled protein release and bone implant material. HA and β-TCP nanopowders were synthesized using reverse micelle as template system. By varying synthesis parameters, β-TCP nanopowders were synthesized with a particle size between 32 and 135 nm, different aspect ratios, and BET specific average surface area varying between 57 and 103 m^2/g.

Bovine serum albumin protein (BSA) release from β-TCP and CDHA nanopowders was studied by *ex situ* adsorption of bovine serum albumin (BSA) onto nanoparticle surface. HA-BSA nanopowders were also synthesized by *in situ* co-precipitation technique. 2 mol% Zn^{2+} and Mg^{2+} were used as dopants to synthesize Zn^{2+} /Mg^{2+} doped HA-BSA nanopowders by *in situ* synthesis route. BSA release rate from *ex situ* synthesized β-TCP-BSA nanopowders found to be faster compared to that from CDHA-BSA nanopowders. For *in situ* synthesized HA-BSA nanopowders, BSA release rate from Zn doped HA nanopowder found to be the highest, whereas

undoped HA nanopowder found to release BSA at the slowest rate. BSA release from *ex situ* synthesized β-TCP and CDHA nanocarriers found to be very fast, whereas much slower and sustained protein release was observed from *in situ* synthesized HA-BSA nanocarriers.

Nanostructure HA compacts were processed using microwave sintering with ultrafine microstructures and improved mechanical properties for orthopedic implant applications. Nanostructured sintered HA compact showed superior compressive strength (395 ±36 MPa), indentation hardness (8.4 ± 0.4 GPa) and indentation fracture toughness (2.0 ± 0.1 MPa $m^{1/2}$). HA compacts were assessed for cell material interaction using SEM, MTT assay and confocal microscopy after culturing human osteoblast cell line on HA disc surface for 1, 5 and 11 days. MTT assays showed higher number of living cell and faster proliferation on nano HA surface. Also osteoblast cells on nano HA surface expressed significantly higher amount of vinculin and alkaline phosphatase (ALP) protein markers for adhesion and differentiation respectively.

This study showed that BSA release rate can be controlled by varying particle size, surface area, phase composition of HA and β-TCP nanocarriers. Nanostructured HA exhibited superior mechanical strength and bioactivity compared to micron grained HA compacts.

TABLE OF CONTENTS

III CHAPTER THREE: NANOTECHNOLOGY AND DRUG DELIVERY

IV. CHAPTER FOUR: SYNTHESIS OF NANOCRYSTALLINE HYDROXYAPATITE AND TRICALCIUM PHOPHATE POWDERS

LIST OF TABLES

LIST OF FIGURES

Dedication

This dissertation/ thesis is dedicated to my late father who taught me the philosophy of life.

CHAPTER ONE

GENERAL INTRODUCTION

1.1 Motivation

1.1.1 Bone implants as biomedical devices

Musculoskeletal injuries have a substantial impact on the health and quality of life of millions of Americans. More than $10 billion per year is spent in the U.S. on hospital care associated with fracture treatment as reported at the annual meeting of American Academy of Orthopedic Surgeons (AAOS), 2004.[1] The percentage of the population older than 65 years of age is expected to increase from 12.4% to 23% between the years 2000 and 2010 in the US (US Bureau of Census 2003).[3] In phase with this, the number of cases for debilitating age-related disease like osteoporosis, will rise from 10.1 million in 2002 to 13.9 million in 2020 (NOF 2003).[2] Approximately 1.5 million bone fractures per year are attributed to osteoporosis (NOF 2003).[2] Unfortunately, almost one-third of patients with hip fractures are forced to reside in nursing homes within one year of fracture and approximately 24% of hip fracture patients aged 50 and over die in the year following the fracture (NOF 2003).[2] Due to the above statistics, the increase in osteoporotic bone fractures worldwide for the next 60 years is projected to be over 300%.

In addition to the above mentioned debilitating osteoporotic fractures, trauma and other bone-related diseases, such as osteoarthritis, require substitute materials to serve as artificial bone. It is expected that these materials will restore the structures and functions of disordered bone quickly and effectively so that the patient can return to a normal healthy lifestyle. However, of the144 400 hip implant surgeries performed in 1997 in the US to heal bone fractures, 37 000 (or 25%) were simply revision surgeries to retrieve a failed implant.[2,4] Moreover, it has been

speculated that the materials (including titanium, CoCrMo alloy, etc) used today as bone fixation devices have an overall average implant lifetime of only 10–15 years.[5] Such a limited lifetime may be appropriate for older patients who may not live past this time frame, but for an aging active population this will not suffice.

In spite of enormous magnitude of this problem, there is still a lack of bone replacement material that is appropriate for restoring lost structure and function, particularly for load bearing applications. Hydroxyapatite (HA) is a biocompatible and bioactive material with a similar crystal structure to that of bone mineral. Hence there is a considerable interest in the development of synthetic HA to cope with such increasing demand**.** Although HA exhibits osteoconductivity and allows new bone to form along its surface the medical applications of HA are limited owing to its relatively low fracture strength and toughness. The mechanical properties of brittle materials, especially flexural strength and fracture toughness are critically dependent upon microstructural features such as grain size and flaw size. Highly dense nanocrystalline HA compacts possess greater reliability, better mechanical properties compared to conventional HA with a coarser microstructure and can be used in spinal fusion and other low load bearing applications. Also since crystal sizes of biological apatite are in the order of tens of nanometers, it has been suggested that better osteoconductivity would be achieved if HA implants were closer to bone mineral in crystal structure, crystal size, and morphology.[6]

Bone is a dynamic tissue and it is obvious that the long-term maintenance of a rigid implant requires continuous remodeling of the bone-implant interface. Maintenance of a viable bone-implant interface involves relatively high rates of continuous remodeling activity. This constant activity renews interfacial and supporting bone by replacing the oldest bone and repairing foci of fatigue damage while maintaining the overall structural integrity of the

osseointegrated implant. Osseointegration is defined as a direct structural and functional connection between ordered living bone and the surface of a load carrying implant without intervening fibrous tissue.[7] As natural bone always undergoes bone remodeling, consisting of osteoclastic bone resorption and osteoblastic bone formation, it is likely that ceramic implants also undergo cell-mediated resorption and bone substitution processes. The osteoclastic resorption process controls bone formation on the ceramic surface since bone resorption and bone formation occur together during natural bone remodeling processes. Conventional micron grained HA implants suffer from very slow rate of resorption and osseointegration with surrounding hard tissues. Nanostructured HA is much more bioresorbable and hence promotes faster mineralization at the bone tissue-implant interface. Thus activities of osteoclast and osteoblast cells are much more enhanced in contact with nanostructured HA implant, which results in faster bone remodeling and subsequently quicker osseointegration.

1.1.2 Nanotechnology and nanomaterials in protein or drug delivery

Nanotechnologies have already brought about a change in the scale and methods of drug delivery and show huge potential for future developments. New formulations and routes for drug delivery have shown the promise for the delivery of new types of medicine to previously inaccessible sites in the body. In addition to developing completely new therapeutic value, introducing upgraded formulations greatly reduces the risk, time and capital invested in new drug development. Nanoparticle based drug delivery technology allows reformulation of existing drugs to increase product lifecycle, increase profitability, and expand intellectual property estate.

The total market for nanotechnology-enabled drug delivery is projected to be $26 billion by 2012 from its current size of $3.39 billion, which corresponds to annual growth rate of 37%.[8] Furthermore; the market could steeply rise after 2012, reaching potentially $220 billion by 2015.

With such enormous growth anticipated, over 60 different companies in U.S, including 38 drug formulation companies and 23 drug delivery companies, are analyzing where they are in their product pipeline, the available market, and the value that their products add to drug delivery.

Different bone growth factors, such as transforming growth factors (TGF β-1), insulin like growth factors (IGF-1), bone morphogenetic protein (BMP), and antiresorptive drug like bisphosphonate can enhance the rate of osseointegration of HA implant.[9-12] Bisphosphonates are particularly effective in the treatment of Paget's disease, tumor associated bone disease and osteoporosis. These kinds of osteoinductive proteins and anti resorptive drug require appropriate carrier material as delivery vehicle.

Calcium phosphate (CaP) nanoparticles found to be potentially good candidate for carrying biocompatible drugs and biomolecules to targeted site, since they can be resorbed by cells and promote new bone formation by releasing Ca^{2+} and PO_4^{3-} ions. CaP nanoparticles possess versatile properties suitable for cellular delivery. These are widely available with variable stoichiometry and functionality. Because of high surface charge density, surface functionalization of CaP nanoparticles is relatively easy which attributes to their potential capability of targeted delivery of drugs and biomolecules to specific sites with controlled release property.

Bone implant materials have a significant economic and clinical impact on the biomaterials field. The global orthopedics market is forecast to drive total revenues to $3.1 billion by the end of 2010. In view of this huge market and anticipated growth in the application of nanotechnology in bone implant and drug delivery, the current study was to investigate the use of nanostructured CaP materials in controlling protein release and osteoblast cell –material interactions at the implant surface.

Preliminary investigations support the potential of nanobiomaterials in orthopedic applications; however, significant advancements are necessary to achieve its clinical use. The research is motivated by the growing market demands for nanobiomaterials and challenges in understanding and improving the tissue-materials interactions for long-term stability and shorter healing time. To understand the bone –cell material interaction at nanosurface of biomaterial and also to fabricate implant material which can mimic natural bone in terms of its mechanical and biological properties it is very important to have some basic understanding about human bone.

1.2 Human Skeletal System

The human skeleton consists of both fused and individual bones supported and supplemented by ligaments, tendons, muscles and cartilage. It serves as a scaffold which supports organs, anchors muscles, and protects internal organs of human body from mechanical damage. The longest and heaviest bone in the body is the femur and the smallest is the stapes bone in the middle ear. There are a total of 206 bones in a matured human body and the skeleton comprises around 20% of the total body weight.

1.2.1 Bone

Bones are rigid tissues composed of cells and a blood supply encased in a strong, interwoven composite structure. Bone tissue can be classified into two categories: (1) cortical or dense and (2) cancellous or spongy. The main difference between cancellous and cortical bone is the open-spaced and trabecular nature of the former as compared to later. The solid framework and pore network are continuous and interconnected domains. There are three types of cells that contribute to bone formation. Osteoblasts are bone-forming cells, osteoclasts resorb or break

down bone, and osteocytes are mature bone cells. The dynamic equilibrium between osteoblasts mediated bone formation and osteoclasts mediated bone resorption maintains bone tissue.

Compact bone consists of closely packed osteons or haversian systems.[13] The osteon consists of a central canal called the osteonic (haversian) canal, which is surrounded by concentric rings (lamellae) of matrix. Between the rings of matrix, the bone cells (osteocytes) are located in spaces called lacunae. Small channels (canaliculi) radiate from the lacunae to the osteonic (haversian) canal to provide passageways through the hard matrix. In compact bone, the haversian systems are packed tightly together to form what appears to be a solid mass. The osteonic canals contain blood vessels that are parallel to the long axis of the bone. These blood vessels are interconnected, by way of perforating canals, with vessels on the surface of the bone.

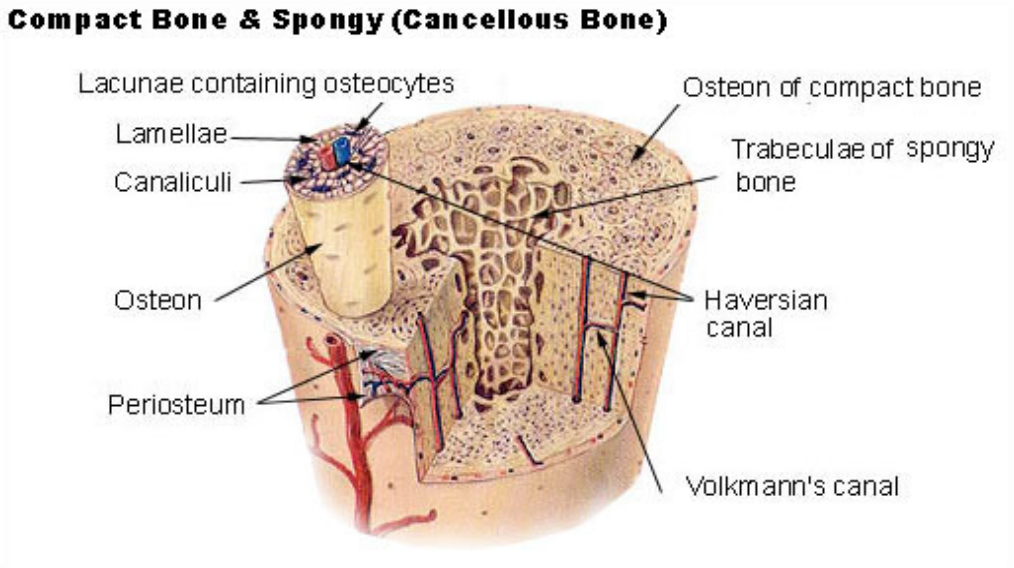

Figure 1.1: Structure of human bone[14]

The main constituents of human bone are 20 wt% collagen (a natural polymer) and 69 wt% CaP (main inorganic component) and 9 wt% water. Additionally, other organic materials such as proteins, polysaccharide and lipids are present in small quantities. Collagen, in the form

of small microfibers, forms the matrix of bone structure by 3-dimensional network formation. The diameter of collagen microfibers varies from 100 to 2000 nm. Presence of CaP in the form of crystalline hydroxyapatite (HA) and/or amorphous calcium phosphate (ACP) provides stiffness to the bone. HA crystals are present in the collagen matrix in the form of platelets or needles, which are 40–60 nm long, 20 nm wide and 1.5-5 nm thick. These crystals are deposited parallel to the collagen fibers such that the larger dimensions of the crystals are along the long axis of the polymer fiber. The deposited HA crystals are connected to each other and form a 3-D network structure.

Bone performs several functions in the human body. It provides a rigid support to human body structure, and protects internal organs of the human body from mechanical damage. Bone assists in the movement of human body parts with the help of muscles and tendons; and serves as a storage area for minerals such as calcium and phosphorus. The excess minerals present in the blood deposits in the bones to maintain optimum mineral concentration in the blood stream. In case, the supply of these minerals in the blood is low, the minerals are leached out from the bones to replenish the supply and thereby blood cells are produced by bone marrow located in the bones. An average of 2.6 million red blood cells is produced each second by the bone marrow to replace those worn out and destroyed by the liver.

Table 1.1. Chemical composition of human bone[13]

Composition	*Enamel*	*Dentine*	*Bone*
Ca^{2+}	36.5	35.1	34.8
P	17.7	16.9	15.2
Ca/P molar ratio	1.63	1.61	1.71
Na^{+}	0.5	0.6	0.9
Mg^{2+}	0.44	1.23	0.72
K^{+}	0.08	0.05	0.03
CO_3^{2-}	3.5	5.6	7.4
F^{-}	0.01	0.06	0.03
Cl^{-}	0.30	0.01	0.13
$P_2O_7^{4-}$	0.02	0.10	0.07
Total inorganic	97	70	65
Total organic	1.5	20	245
Adsorbed H_2O	1.5	10	10

Mechanical properties of human bone are given in **table 1.2**. Because of its lower density, cancellous bone has a lower modulus of elasticity, and lower compressive and tensile strength than cortical bone.

Table 1.2. Mechanical properties of human bone[13]

Properties	*Cortical bone*	*Cancellous bone*	*Enamel*	*Dentine*
Compressive strength (MPa)	130-180	2-12	95-370	250-350
Tensile strength (MPa)	60-160	10-20	10	21-53
Young's (tensile) modulus (GPa)	3-30	0.05-0.5	-	11- 19
Fracture toughness (K_{Ic})	2-12	-	-	-
Hardness (Knoop)	132-166	-	-	-

1.3 Biomaterials

A biomaterial is a nonviable material used in a medical device, intended to interact with biological systems (William 1987). Biomaterial by definition is "a non-drug substance suitable

for inclusion in systems which augment or replace the function of bodily tissues or organs". These materials are capable of being in contact with bodily fluids and tissues for prolonged periods of time, exhibiting very little or no adverse reactions to body.

1.3.1 Historical Background

Use of biomaterials did not become practical until the advent of the aseptic surgical technique developed by Dr. J. Lister in the 1860s. Earlier surgical methods involved in tissue replacement were generally unsuccessful as a result of infection. The earliest successful implants, as well as a large fraction of modern implants, were in the skeletal system. Bone plates were introduced in the early 1900s to aid in long bone fracture. Many of these implants did not work well due to poor material properties and poor design. Several improvements and research studies have been done to get better performance of the implant structure. **Table 1.3** shows the notable developments of implant research and applications.[15]

Table 1.3: Notable development relating to implants[15]

Year	***Investigators***	***Development***
Late 18th - 19th century	-	Various metal devices to fix bone fractures; wires and pins from Fe, Au, Ag and Pt
1860-1870	J. Lister	Aseptic surgical technique
1866	H. Hansmann	Ni-plated steel bone fracture plate
1912	W. D. Sherman	Vanadium steel plates first developed for medical use
1924	A. A. Zierold	Introduced Stellites (CoCrMo alloy)
1931	M. N. Smith-Peterson	First femoral neck fracture fixation device made of stainless steel
1936	C. S. Venable, W .G Stuck	Introduced Vitallium (19-9 stainless steel), later changed the material to CoCr alloy
1938	P. Wiles	First total hip replacement
1946	J. and R. Judet	First biomechanically designed femoral head replacement prosthesis. First plastic (PMMA) used in joint replacement
1947	J. Cotton	Introduced Ti and its alloy

The development and application of surgical and orthopedic implants made it necessary to give increasing attention to the materials used to manufacture such implants. These materials, which are also referred to as biomaterials, must meet certain chemical, physical and biological requirements, in order to ensure optimum and lasting function of implants and success of the implantation procedure.

1.3.2 Biocompatibility

Biomaterials science is the physical and biological study of materials and their interaction with the biological environment. When the material is placed inside the body, within a few milliseconds, a biolayer consisting of water, proteins and other biomolecules from the physiological liquid is formed on the implant surface. Subsequently, stimulated by cytokines and growth factors in the biolayer, cells from the surrounding tissue migrate to the area around the implant. The interaction between an implant surface and the cells is thus mediated through this biolayer. Biocompatibility is the ability of a material to perform with an appropriate host response in a specific application (William, 1987). Examples of appropriate host responses include resistance to blood clotting, resistance to bacterial colonization and normal, uncomplicated healing. Biocompatibility is determined by the extent of chemical and biological interaction between host and implant, and stability (mechanical integrity) of the implant. A compatible implant would have no effect on the adjacent tissue, the nearby cells would show no abnormalities, no variant cell types would appear, there would be no inflammatory reactions, and there would be no cell necrosis. Biocompatibility of devices must be established and approved by regulatory agencies, for example Food and Drug Administration (FDA), International

Organization for Standardization (ISO) before any biomedical devices are marketed and used clinically. **Table 1.4** lists a few applications for synthetic materials in the body.

Table 1.4: Some biomedical applications of synthetic materials[14]

Applications	***Types of materials***
Skeletal systems	
Joint replacements (hip, Knee)	Titanium, Ti-Al-V alloy, Stainless steel.
Bone plate for fracture fixation	Stainless steel, cobalt-chromium alloy
Bone cement	Poly(methyl methacrylate)
Artificial tendon and ligament	Teflon, Dacron
Dental implant for tooth fixation	Titanium, Ti-Al-V alloy, Stainless steel. Titanium, alumina, calcium phosphate
Cardiovascular system	
Heart valve	Stainless steel, carbon, reciprocated tissue
Catheter	Teflon, silicone rubber, polyurethane
Organs	
Artificial kidney	Cellulose, polyacrylonitrile
Skin repair template	Silicone-collagen composite
Senses	
Contact lens	Silicone-acrylate, hydrogel
Intraocular lens	Poly(methyl methacrylate), hydrogel, silicone rubber

1.3.3 Biomaterials classifications

A. Based on material-tissue interactions

Depending on the nature of biomaterial, tissue reacts towards the implant in a variety of ways. The tissue response to the implant biomaterial surface ultimately governs activity and efficiency of implant material inside the body. In general, biomaterials may be described in or classified into three categories such as bioinert, bioactive and bioresorbable depending on their interaction with tissues and cells.

Bioinert materials when placed inside the human body exert minimal interaction with its surrounding tissue. Generally a fibrous capsule is formed around the bioinert implants and hence biofunctionality of this kind of material depends on tissue integration through the implant. Examples of bioinert biomaterials are stainless steel, titanium, alumina, partially stabilized zirconia, ultra high molecular weight polyethylene etc.

Bioactive material, when placed inside the human body interacts with the surrounding bone and soft tissues through the time dependent kinetic modification of the implant surface. A biologically active carbonate apatite (CHA) layer is formed on the bioactive implant surface by the ion exchange reaction between the bioactive implant and surrounding body fluids. This biologically active carbonate apatite (CHA) layer is chemically and crystallographically equivalent to the mineral phase in bone. Prime examples of these bioactive materials are synthetic hydroxyapatite [$Ca_{10}(PO_4)_6(OH)_2$], glass ceramic A-W and bioglass.

Bioresorbable materials are the one which is dissolved or resorbed and slowly replaced by advancing tissues, such as bone, when used as an implant material inside the body. Common examples of bioresorbable materials are tricalcium phosphate [$Ca_3(PO_4)_2$] and polylactic–polyglycolic acid copolymers.

B. Based on type of materials

Depending on the type of materials, biomaterials can primarily be divided into three categories- metals, ceramic and polymer. Sometimes a combination of these materials is used as composite structure. Application of these materials include replacement of hips, knees, teeth,

tendons and ligaments; repair of periodontal disease; maxillofacial reconstruction; spinal fusion, and bone repair.

(i) Metal as biomaterial

Metals have been extensively used for load-bearing implants, such as hip and knee prostheses and fracture fixation wires, pins, screws, and plates. Metals also find application as parts of artificial heart valves, as vascular stents, and as pacemaker leads. Metallic alloys with improved materials properties, such as strength and corrosion resistance, are sometimes used as implant instead of pure metal. The main considerations in selecting metals and alloys for biomedical applications are biocompatibility, appropriate mechanical properties, corrosion resistance, and reasonable cost.

The mechanical properties of materials are of great importance when designing load-bearing orthopedic and dental implants. Mechanical properties of some of the most commonly used metallic implants are listed in **table 1.5**.

Table 1.5: Select Properties of Metallic Biomaterials[14]

Material	***Young's Modulus E (GPa)***	***Yield Strength*** σ_y ***(MPa)***	***Tensile Strength*** σ_{UTS} ***(MPa)***	***Fatigue Limits*** σ_{end} ***(MPa)***
Stainless steel	190	221-1,213	586-1,351	241-820
Co-Cr alloys	210-253	448-1,606	655-1,896	207-950
Ti	110	485	760	300
Ti-6Al-4V	116	896-1,034	965-1,103	620
Cortical bone	15-30	30-70	70-150	

The elastic moduli of the metals listed in **table 1.4** are at least seven times greater than that of natural bone. This mismatch of mechanical properties can cause stress-shielding of either condition characterized by bone resorption (loss of bone) in the vicinity of implants. Compared to the elastic moduli of either stainless or cobalt-chromium molybdenum alloys, Ti and Ti-6Al-

4V have much lower moduli that are still almost an order of magnitude higher that of bone. Another advantage of Ti-based metals as bone implants is their favorable strength-to-density ratio.

(ii) Polymer as biomaterial

The structures of polymers determine their application in various medical domains. Their selection for subsequent employment in surgery, dermatology, ophthalmology, pharmacy, etc. is mainly determined by their chemical and physical properties. Biomedical polymers can be classified into either elastomers or plastics. Elastomers are able to withstand large deformations and return to their original dimensions after releasing the stretching force. Plastics on the other hand are more rigid materials and can be classified into two types: thermoplastics and thermosetting. Thermoplastic polymers can be melted, reshaped and reformed. Thermosetting plastics cannot be remelted and reused because of the irreversible nature of the chemical reaction during the formation of it. Current applications of biomedical polymers include vascular grafts, heart valves, artificial hearts, contact lenses, intraocular lenses, sutures, adhesives. **Table 1.6** shows some of the polymers and their uses.

Table 1.6 Examples of Biomedical Applications of Polymers[14]

Applications	***Polymers***
Cardiovascular implants	Polyethylene, Polyvinyl chloride (PVC), polyester, silicone rubber, polytetrafluoroethylene
Orthopedic implants	Ultra-high-molecular-weight polyethylene (UHWMPE), polymethylmethacrylate
Drug release	Polylactide-co-glycolide
Tissue engineering	Polylactic acids, polyglycolic acid, Polylactide-co-glycolide

The mechanical properties of polymers depend on several factors, including the composition and structure of the macromolecular chains and their molecular weight. Compared

to ceramic and metals, polymers have much lower strength but they can be deformed to a greater extent before failure. **Table 1.7** shows some of the mechanical properties of selected polymeric biomaterials. Ultra high molecular weight polyethylene is used for bearing surface in hip and knee replacements.

Table 1.7: Mechanical Properties of Polymers[16]

Polymers	***Tensile strength σ_{UTS} (MPa)***	***Young's Modulus E (GPa)***	***% Elongation***
Polymethylmethacrylate	30	2.2	1.4
Nylon 6/6	76	2.8	90
Polylactic acid	28-50	1.2-3	2-6
Polypropylene	28-36	1.1-1.55	400-900
Polytetrafluoroethylene	17-28	0.5	120-350
Silicone rubber	2.8	Up to 10	160
Collagen	141.2-85.7	5-11.5	250-450

(iii) Ceramic as biomaterial

Bioceramics are employed as components of hip implants, dental implants and heart valves. They are also designed and fabricated for repair and reconstruction of diseased, damaged or "worn out" parts of the body. Some of the ceramics that have been used for biomedical applications are listed in **table 1.8**.

Table1.8. Ceramics Used in Biomedical Applications[14, 17]

Ceramic	*Chemical Formula*	*Types of Attachment*	*Comment*
Alumina	Al_2O_3	Mechanical interlock (morphological fixation)	Bioinert
Zirconia	ZrO_2		
Pyrolytic carbon			
Bioglass	Na_2O $CaOP_2O_3$-SiO	Interfacial bonding with tissues (Bioactive fixation)	Bioactive
Highly dense pure Hydroxyapatite	$Ca_{10}(PO_4)_6(OH)_2$		
Hydroxyapatite (sintered low temperature)	$Ca_{10}(PO_4)_6(OH)_2$	Ingrowths of tissues in pores (Biological fixation)	Biodegradable
Tricalcium phosphate	$Ca_3(PO_4)_2$	Replacement with tissues	

The major drawback of bioceramics is that they fail catastrophically due to the presence of cracks or other defects. Although some of the bioceramics exhibit outstanding strength when loaded in compression, they fail at low stress in tensile or bending environment. The mechanical properties of CaPs and bioactive glasses make them unsuitable as load-bearing implants. **Table 1.9** shows some of the mechanical properties of ceramic biomaterials. Among the biomedical ceramics, alumina has the best mechanical properties, but its tensile properties are still below those of metallic biomaterials. Additional advantageous properties of alumina are its low coefficients of friction and wear rate. Because of these properties, alumina has been used as a bearing surface in joint replacements.

Table 1.9 Mechanical properties of ceramic biomaterials[17]

Bioceramics	*Young's Modulus E (GPa)*	*Compressive Strength, σ_{UCS} (MPa)*	*Tensile Strength, σ_{UCS} (MPa)*
Alumina	380	4500	350
Bioglass-ceramics	22	500	56-83
Calcium Phosphate	40-117	510-896	69-193
Pyrolytic carbon	18-28	517	280-560

Bioceramics are corrosion resistant, but susceptible to other forms of degradation when exposed to a physiological environment. The mechanism and rate of degradation vary depending on the type of bioceramic. Even alumina, a predominantly bioinert ceramic, suffers from time-dependent deterioration in strength when placed in physiological environment *in vitro* and *in vivo.* CaP based bioactive ceramics are also degraded in the body by virtue of its dissolution in physiological fluid and osteoclasts mediated bioresorption. The rate of degradation of CaP ceramics will vary depending on their phase, chemical composition, and crystal structure.

Table 1.10 shows different types of CaP compound.

Table 1.10 Calcium Phosphate Ceramics[18]

Chemical Name	**Abbreviation**	**Chemical formula**	**Phase**	**Ca/P**	**Solubility Product at 37 ^{o} C in H_2O**
Monocalcium Phosphate	MCP	$Ca(H_2PO_4)$, H_2O	--------	0.50	$1X\ 10^{-3}$
Dicalcium Phosphate Hydrate	DCPD	$CaHPO_4$, H_2O	Brushite	1.00	$1.87X\ 10^{-7}$
Dicalcium Phosphate Anhydrous	DPCA	$CaHPO_4$	Monetite	1.00	$1.26\ X\ 10^{-7}$
Octacalcium Phosphate pentahydrate	OCP	$Ca_8H_2(PO_4)$. $5\ H_2O$		1.33	$5.1\ X\ 10^{-15}$
Tricalcium Phosphate	α-TCP	$Ca_3\ (PO_4)_2$		1.50	
	β-TCP	$Ca_3\ (PO_4)_2$	Whitlockite	1.50	$2.83\ X\ 10^{-30}$
Pentacalcium Hydroxyal Apatite	HA	$Ca_{10}\ (PO_4)_6(OH)_2$	Hydroxyapatite		$2.35\ X\ 10^{-59}$
Tetracalcium Phosphate monoxide	TTCP	$Ca_4O(PO_4)_2$	Hilgenstockite	2.00	

The solubility of different CaP minerals changes in the following order.

ACP>DCP>TTCP>α-TCP>β-TCP>>HA

The slowest rate of dissolution of HA among all the CaP ceramics is not surprising, because it is the only stable CaP compound at and above pH 4.2. The applications of CaP based bioresorbable ceramics include drug delivery vehicle, repairing damaged bone, repairing and fusion of spinal and lumbo-sacral vertebrae, repairing maxillofacial and dental defects.

Bioactive ceramics mostly include CaP based materials and bioactive glasses. A common characteristic of all bioactive implant is the formation of a hydroxya carbonated apatite (HCA) layer on their surface when implanted. Depending on the nature of bioactive ceramics, the formation of HCA layer may take from days to weeks. The application of bioactive ceramics includes coating on prostheses, reconstruction of dental defects, bone plate and screws, replacements of middle ear ossicles and correcting periodontal defects.

CHAPTER TWO

NANO BIOMATERIALS IN ORTHOPEDIC APPLICATION

2.1 Introduction

Due to the increase in average life time and consequent increase in the aging population, the market for orthopedic implants is growing at a rapid rate. Each year, more than 600,000 joint replacements are performed in the USA alone with an estimated worldwide cost in excess of 3 billion dollars.[1] Metals are most commonly used for total bone replacement or implant fixations, primarily because of its excellent mechanical properties necessary for load-bearing applications.[14] The versatility in chemical and mechanical properties of polymeric materials has led to the development of biodegradable, biocompatible polymeric implants for orthopedic applications.[18] However, both metal and polymeric implants suffer from stress-shielding, joint loosening due to wear, and limited compatibility with bone tissue, which ultimately leads to failure of implants.[13] Failed implants require several challenging revision surgeries with consequent increase in cost and recovery time.

One of the key factors identified in the failure of orthopedic implants was insufficient tissue regeneration around the biomaterial immediately after implantation, mainly because of poor surface interaction of biomaterials with the host tissue.[14] It is known that implantation of biomaterials into a living organism causes specific reactions in the biological environment.[19] The biomolecules and cells together with the intrinsic as well as surface properties of the biomaterials determine the biocompatibility and longevity of the implants.[20] Since the biomolecule or cell – material interaction at the surface of biomaterial is an important phenomenon in the evaluation of the biomaterial, biomaterial scientists investigate the pertinent host–cell interactions in order to design materials that facilitate favorable interactions and enhance tissue regeneration.

Research results indicate that all living systems are governed by molecular behavior at nanometer scales. The properties of proteins, nucleic acids, lipids, and carbohydrates, which are molecular building blocks of life, are determined by their size, folding, and patterns at the nanoscale. Specifically, cellular organization and corresponding tissue properties are found to be highly dependent on the structure of the extracellular matrix (ECM).[20] ECM is characterized with a complex hierarchical structure with spatial organization spanning several orders of magnitude from nm to cm scale. That is why; cells in our body are predisposed to interact with nanostructured surfaces.[21] Indeed, research evidence shows that a biomaterial substrate composed of nanometer-scale components is biologically preferred.[22] Structural components with nanoscale features are thus being considered as promising biomaterials.

2.2 Cellular recognition of nanoscale structure

A common objective in orthopedic research is to design biomaterial compatible to cell and tissue growth. Cell functions such as proliferation, migration, and ECM production are determined by nanoscale protein interactions in native tissues.[23] Surface features of biomaterials such as roughness, charge, chemistry, wettability etc. in turn control protein adsorption characteristics onto implanted biomaterial.[24] The particulate or grain size of the biomaterial influences these surface properties and the corresponding protein interactions. Recent reports suggest that the unique properties of nanobiomaterials promote favorable interactions with the proteins that control cellular function.[25, 26] Nanobiomaterials possess a higher surface area to volume ratio than conventional microscale biomaterials due to the presence of increased number of atoms and crystal grains at their surfaces. The corresponding surface energy for protein adsorption onto nanobiomaterial is greatly changed due to the differences in surface topography. In particular, the interaction of four proteins such as fibronectin, vitronectin, laminin, and

collagen, which are known to enhance osteoblast function, was found to increase greatly on nanobiomaterials as compared to conventional micron grained biomaterials. Webster et al. correlated enhanced vitronectin adsorption, conformation, and bioactivity to the increased osteoblast adhesion on nanophase alumina.[25]

Osteoblasts have been shown to adhere to select amino acid sequences (such as Arginine-Glycine-Aspartic Acid or RGD) in proteins adsorbed onto biomaterial surfaces. Since the foremost condition for orthopedic implant to synthesize bone on its surface is osteoblast adhesion, optimization of initial protein adsorption is integral to implant success. Two other factors, which are extremely important for orthopedic implant, are its ability to ECM production and mineralization. Thus, optimization of biomaterial surfaces for ECM production and subsequent mineralization are essential criteria for orthopedic implant that promote cell adhesion. It is evident that the key to modulating these critical protein interactions, and subsequent cellular behavior and tissue regeneration, lies in utilizing nanobiomaterials as orthopedic implant.

2.3 Nano Biomaterials as Bone Implant

The advent of nanobiomaterials has generated significant opportunities to modulate cellular function at the surface of orthopedic implant. Depending on design strategies nanomaterilas can be used in various ways in different orthopedic applications which are described below.

2.3.1 Biomimetic Nanocomposites

The nanoscale structure of ECM motivates scientists and engineers to tailor orthopedic implant surfaces with nanoscale features. Nanoscale CaP crystallites similar to hydroxyapatite are the main inorganic component of bone ECM. That is why, CaP materials are natural choices

as biomaterials. Indeed, CaP ceramics exhibit good biological properties because of their ability to form a chemically bonded interface with bone.[27] However, due to poor mechanical properties the bulk synthetic CaP materials are not used at load-bearing, orthopedic sites. Consequently, CaPs are mostly used as coatings on metallic (mostly titanium and its alloys) bulk materials. In a recent study, osteointegration was observed in tantalum porous scaffolds coated with nano hydroxyapatite particles within 6 weeks of implantation into rat calvaria.[28]

Several techniques are available for the deposition of CaP-coatings on metals, including plasma spraying,[29] biomimetic deposition,[30] laser deposition,[31] ion beam deposition,[32] radiofrequency (RF) magnetron sputter deposition,[33] and electrostatic spray deposition (ESD).[34] Although plasma spraying is frequently used to deposit CaP coatings on orthopedic and dental implants, this technique suffers from lack of controlling coating structure, relatively low cohesion within the thick coatings (~50 μm), and the limited bond strength with the metallic implant substrate.[29] Biomimetic deposition of CaP-coatings results in the deposition of CaP crystals with nanoscale dimensions.[30] An interesting aspect of the biomimetic process of CaP deposition is that it can be combined with the deposition of biologically active compounds.[35] Through this co-precipitation process, the resulting CaP coatings do not only introduce bioactivity but can also actively influence cellular processes and reduce bacterial infections.

2.3.2 Nanostructured Biomaterials

Several literature reports suggest that decrease in ceramic grain size results in enhanced bone cell function. Specifically, compared to conventional micron grained ceramic, nanostructured alumina, titania, and hydroxyapatite show enhanced *in vitro* adhesion of osteoblasts. Osteoblast functions were also found to be increased at ceramic spherical grain sizes below 60 nm.[36] Studies further reported enhanced in vitro calcium deposition by osteoblasts as

well as increased functions of osteoclasts on nanophase alumina and titania.[37] Particle aspect ratio is another important feature for orthopedic nanomaterials. Compacts of nanofibrous alumina (diameter: 2 nm, length >50 nm) exhibited significantly enhanced *in vitro* osteoblast functions in comparison to similar alumina compacts formulated from nanospherical particles.[38]

Not only ceramics, but nanophase metals (such as titanium, Ti_6Al_4V, and CoCr alloys) and polymers have also demonstrated promising properties for enhanced bone cell functions. In a disease-specific study, researchers have reported increased *in vitro* osteoblast functions on nanophase compared to conventional selenium.[39] The anticancer properties of selenium has explored the potential use of nanophase selenium in implants for the treatment of bone cancer.

Nanotopographies on metal surfaces have been found to be advantageous for osteoblast cell adhesion and growth. Compared to unanodized titanium, greater *in vitro* osteoblast adhesion and mineral deposition were observed on anodized titanium possessing TiO_2 nanotubes on surface.[40] The similar behaviors of osteoblast cells have also been observed for anodized aluminum.[41] Similarly, increased *in vitro* osteoblast functions were observed on poly(lactic-co-glycolic acid) (PLGA) cast from nanophase titania compared to conventional titania.[42] The results suggest that the proactive surface roughness of nanophase materials can be transferred to polymers to enhance the efficiency of orthopedic implant.

2.3.2.1 Nanostructured Hydroxyapatite

Apatite-related compounds, which are CaP based compounds, have crystallographic and chemical characteristics similar to various hard tissues such as bones and teeth of vertebrata, and thus strongly bind to biotissues when they are transplanted in a body. HA $[Ca_{10}(PO_4)_6(OH)_2]$ is known as a representative apatite. Taking advantage of its bioactivity there have been efforts to replace impaired teeth and bones with HA. It is sensitive to nonstoichiometry and impurities due

to its complex composition and crystal structure ($Ca_{10}(PO_4)_6(OH)_2$, (P63/m). As a result, conventionally processed HA materials lack phase purity and homogeneity. Densification typically requires high temperatures, which results in grain growth and decomposition into undesired phases with poor mechanical and chemical stability.[43] To avoid densification at high temperature, glassy additives can be introduced to promote liquid phase sintering at a lower temperature. However, the presence of a secondary glassy phase gives rise to poor mechanical strength.[44] Since mechanical properties such as strength and fracture toughness of micron grained HA are poor, its use is limited to non load-bearing implants, coatings and low loaded porous implant.

Bone is a composite material consisting of biological apatite (length. 50 nm, breadth. 25 nm and thickness up to 4 nm) and a matrix of collagen fibers (50–70 nm in diameter).[45] Nanocrystalline HA would be more interesting than micro-sized HA from a biological and medical viewpoint because of its similarity to minerals in natural bone. Compared to conventional microscale HA, which lacks phase purity and homogeneity, nano HA offers the possibility to enhance the rate of bone-bonding formation and possess greater reliability, improved mechanical properties to be applied as load bearing implant. With minimized flaw sizes, nanocrystalline HA can be densified without sintering additives at substantially lower temperature and demonstrate unusual strength and ductility compared to the conventional polycrystalline HA. The nanostructured HA not only provide superior mechanical properties but also offer the potential for net-shape forming for inexpensive rapid prototyping.

2.4 Objectives and Research Plan

The objective of this research was to understand the influence of grain size on mechanical properties and bioactivity of HA compacts. The efficiency of HA ceramics as orthopedic implant

greatly depends on its grain size. Not only the osteoblast cells show grain size dependent activities on HA compacts, but mechanical properties of HA compacts also greatly vary with change in grain size in sintered HA microstructure. Particularly, as already been discussed earlier, orthopedic implant exhibits remarkably different bioactivities and mechanical reliability at nanoscale. Thus it is interesting to investigate how one can monitor the biological as well as mechanical properties of HA ceramics by changing its grain size. The research has been focused on following different areas.

1. Consolidation and sintering of HA compacts: HA nanopowders were synthesized by reverse microemulsion based template system. The synthesized HA nanopowders were calcined for different time and then ball milled to get rid of agglomerates. The ball milled HA nanopowders were mixed with ammonium polymethacrylate dispersant, freeze dried, and then consolidated by uniaxial pressing at 50 MPa followed by cold isostatic pressing at 345 MPa. The green HA compacts were sintered in microwave furnace at 1000 C, 1100 C and 1150 C for different time from 20 minutes to 45 minutes. HA compacts with variation in average grain size from 150 nm to 12.5 μm were prepared.

2. Evaluation of mechanical properties of HA compacts: Mechanical properties such as compressive strength, indentation hardness, and fracture toughness of HA compacts were evaluated with variation in grain size in sintered HA microstructure. The mechanical property data of these nano HA compacts will be compared with trabecular and cortical bone. 3. Study of biological and surface properties: Biological properties of these different grained HA compacts were evaluated with an *in vitro* hFOB 1.15 human osteoblast cell line cultured for 1, 5 and 11 days. Protein expression with vinculin molecules and enzymatic behavior with alkaline

phosphatase both were evaluated on different grain sized HA compacts. Surface properties like surface energy and contact angles were also measured on different grain sized HA compact

CHAPTER THREE

NANOTECHNOLOGY AND DRUG DELIVERY

3.1 Introduction

The nanotechnology based drug delivery system offers an extraordinary opportunity to make significant advances in medical diagnosis and treatment. Corporate investment for nano technological development in the fields of drug delivery and medical diagnostics is increasing year by year and a lot of companies have already commercialized some of the nanotechnology-based drug delivery systems.

Traditionally nanotechnology based drug delivery system mainly focuses on utilizing nanoscale vehicles to transport the drug molecules to desired locations. Recently, new nanoscale platforms are under development for not only therapeutic purpose, but also diagnostics applications.[46] Apart from functioning as a nanoscale drug carrier, these nanotools can also be used for medical diagnostics via fluorescent imaging [47] or magnetic resonance imaging. [48] Multifunctional nanoparticles with the combination of therapeutic, targeting, and imaging functions for advanced drug delivery systems have drawn more and more attention from current researchers. [49, 50]

3.2 Advantages of nanostructured delivery systems

The common ways of administration of active pharmaceutical ingredient (API) are oral, transdermal, and nasal delivery methods.[51] Though oral delivery pathway is the most sought after delivery method, it has many limitations from reduced bioavailability and ineffectiveness to deliver protein and peptides due to the effects of pH in the digestive system, and the effects of stress from the intestines.[52] The nasal and transdermal methods cause patient discomfort and also

have reduced efficiency and availability in the system.[53] Other challenges with the conventional drug delivery systems involve difficulties for targeting specific regions without affecting healthy tissues.[54] Nanotechnology-based drug delivery systems have potential to address all those challenges associated with conventional drug delivery systems.

3.2.1 Localized and targeted delivery

Nanotechnology based drug delivery systems can be utilized to control drug delivery to specific sites and target cells only, without affecting the neighboring healthy cells.[55, 56] Several external stimuli such as ultrasound and magnetic field have been effective in drug targeting in nanocarriers for tumor eradication. Several biologically relevant molecules such as transferin,[57] folate [58] and antibodies [59] play important roles in internal targeting and internalization of drugs. The localized and targeted delivery greatly helps in reducing side effect and increases effectiveness of the therapeutic ingredients.[52]

3.2.2 Controlled delivery

The nanotechnology based drug delivery systems have enabled researchers with options of deliver highly toxic drug intermediates and complexes, as well as DNA and viral vectors at optimum dosage at controlled time periods. [53] Release profile from materials largely depends upon the nature of the delivery system. By choosing the correct type of materials for preparation of nanoparticles, the release profile can be modified.[60] In addition, nanotechnology opens the door for atomic scale modification in materials for the creation of nanosystems with extremely controllable delivery rates. [61]

3.2.3 Enhanced circulation time and biodistribution

Nanocarriers may increase the circulation time of drugs within the body. Particle size is intrinsically related to rate of clearance from the circulation. Larger particles tend to be removed

much faster than smaller particles. Not only the enhanced circulation time, nanoparticles also exhibit improved biodistribution over their larger counterparts. In animal study, it was found that larger particles tend to accumulate in high concentrations in spleen and liver rather than in the target locations. Smaller particles are more likely to be distributed to other cells within the body, including target cells.

3.2.4 Drug solubility

Nanotechnology allows for the delivery of all types of drugs. Particularly, the drugs exhibiting poor solubility in water can be effectively transferred to living tissues when loaded on a nanocarrier. Micelles are composed of a hydrophobic core surrounded by a hydrophilic outer layer, known as corona. Hydrophobic drug molecules can be easily encapsulated in the microenvironment of the core. The hydrophilic corona facilitates travel of the nanoparticles through water –based solutions. This ensures delivery of hydrophobic therapeutic compounds in aqueous environments of the human body.

3.2.5 Intracellular drug delivery

Intracellular drug delivery helps in reducing toxicity and improving dosage efficiency. Hydrophobic drug carriers at nanoscale are able to easily pass through the membrane. Endocytosis in cells is limited by particle size and targeting tissues. The maximum size of material that can penetrate the cell membrane is about 500 nm. The ability of nanocarriers to be internalized into cell also enables drugs or biomolecules to be activated and targeted to specific cell organelles such as the nucleus or the mitochondria.

The delivery of hydrophilic or genetic components into cell possesses the greatest challenge. The mechanisms for cellular internalization of the nanoparticles include direct diffusion through the cell membrane owing to concentration gradients, crossing the voltage-gated

channels and receptor-mediated endocytosis. Lipid and micelle based delivery systems provide various opportunities to encapsulate or to bind to specific hydrophilic and hydrophobic constituents, hence producing nanoparticles that can be modified on the surface to cause endocytosis.

3.2.6 Ability to cross biological membranes

The difficulties in crossing the biological membranes like the blood-brain barrier (bbb), gastrointestinal system and the vascular endothelial system have posed great challenges to drug delivery. Conventional delivery methods such as intravenous delivery, oral delivery or transdermal delivery of microparticles have failed in regions that need to penetrate the BBB or the gastrointestinal systems because of various physiological environment aspects including the pH dependence and the size properties. Nanotechnology based drug delivery devices have the ability to cross biological membranes when tailored with appropriate properties. Metallic nanomaterials, polymeric drug carriers, and lipid based delivery systems have provided the researchers with opportunities to drive the drug through biological membranes.

3.2.7 Enhanced surface areas

It is a well known fact that due to size reduction per unit volume the surface area of materials increases. As compared to the conventional drug delivery systems, nanotechnology based drug delivery systems have improved surface areas. This increased surface area per unit volume leads to improvement on loading and releasing efficiency of drug.

3.3 Nanoparticles used in drug delivery

The nanoparticles used in drug delivery application are mostly less than 1 μm in diameter, spherical, and either porous or core-shell type particles. Typically, the API is entrapped within the particle during synthesis or can be uptaken after synthesis. [62] All kinds of therapeutics

like hydrophobic anticancer drugs doxorubicin [63,64], daunorubicin[65] and paclitaxel [66] as well as hydrophilic dexamethasone phosphate,[67] ribonuleases,[68] and proteins[69] can be encapsulated inside the nanoparticles. Controlled release of entrapped API from nanocarriers takes place over time or upon an external trigger such as pH,[70] focused magnetic fields,[71] ultrasound,[72] or temperature.[73]

Nanomaterials in various forms are used in drug delivery. These include hydrogels, [74] lipids/liposomes/micelles, [75-78] virosomes,[79] polymers (PLGA, [80] PMMA,[81]cyanoacrylates,[82] and PAA,[83] biopolymers (collagen[84] and chitosan[85]), paramagnetic alginate beads,[86] colloidal gold[87, 88] porous hollow silica,[89] calcium carbonate, [90] and core-shell types (liquid filled nanoparticles,[91] polymer nanocapsules[92]). Of these, continuous polymers and liposomes have got the most attention and widely been investigated.

Most of the polymeric nanoparticles being porous spheroids entrap API in their polymeric matrix and release their contents through either diffusion or matrix swelling. PLGA is highly biocompatible and biodegradable and can encapsulate anticancer agents, antihypertensive agents, immunomodulators, hormones, and macromolecules, but short term stability is the issue which restricts its wide application as drug delivery vehicle. [80] Also some organic solvent is required during synthesis of these materials which can pose a problem for some biomolecules.

Liposomes have long been used as drug delivery vehicles [93-97]and the fact that no organic solvent is required for its synthesis renders them slightly more biofriendly than polymer nanoparticles, but they also suffer from stability and leaking issues due to their thin lipid membrane.[98] They can also encapsulate a wide range of both hydrophilic and hydrophobic API by encapsulating them within their aqueous compartments and lipid membranes.[99, 100]

Recently inorganic nanoparticles as new non-viral carriers have attracted much attention. Many inorganic materials, such as CaP, gold, carbon materials, silicon oxide, iron oxide and layered double hydroxide (LDH), have been studied. Viral carriers are to date the most effective, but severe side effects limit their successful application in cellular delivery. Liposome and polymer nanocarriers may avoid such problems but are often found to be toxic to living cells. In contrast, inorganic nanoparticles show low toxicity and significant promise for controlled delivery properties, thus presenting a new alternative to viral and organic carriers. However, at the present form, cellular transfer efficiency with existing inorganic nanoparticles is relatively low.

3.4 Targeted drug delivery using nanoparticles

For localized delivery of API within the body the nanoparticles need to be conjugated to a targeting molecule that attaches to specific cells with the receptor. This technique is referred to as receptor mediated delivery.[101] There are a number of molecules, can be used for targeting labels, that includes carbohydrates,[76] ligands,[102] peptides, [103] antibodies [68, 104] selectins,[105] folate[106] and lectins[76, 107] oligosaccharides. Glycoconjugates are emerging as versatile targeting molecules because the surface of cells is rich in carbohydrates and attached glycolipids/glycoproteins.[108] Folate is the most commonly utilized for targeting tumor cells. It has been found that folate functionalized particles localize selectively at the tumor molecule as many tumors over express the folate receptor.[106, 109, 110] Attachment of these receptor molecules to the nanoparticles is accomplished through covalent, electrostatic, or biotynilated conjugation techniques. [111]

3.5 Potential for calcium phosphate (CaP) nanoparticles in drug delivery

CaP nanoparticles possess versatile properties suitable for cellular delivery, including rich functionality, exceptional biocompatibility, and potential capability of targeted and controlled delivery of carried API. Nano and microparticles of CaP are employed in the delivery of antibiotics,[112]proteins,[113] plasmids,[114] ocular drugs,[115,116] nucleic acid-based drugs,[117] as nonviral vectors for gene transfection into cells,[118-120]and other applications.[121] Nanoparticles of CaP are used as a bioactive component in pastes and injectable cements[122,123] for the reconstruction of orthopedic and dental defects. [124] Rigid combinations of nanoparticles[125] and nanoparticle/polymer composites[126] are applied as biodegradable/resorbable[127,128] scaffolds for the guided regeneration of bone tissue.[129, 130] Trehalose delivery from microneedles coated with porous CaP has been reported.[131] Alginate–CaP microspheres are used as enzyme delivery matrices *in vivo*.[132] As a bioactive coating, CaP also aids the osseointegration of titanium based orthopedic implants.[133-138].

Core-shell type nanoparticles are very demanding in the field of drug delivey.[139-141] Due to the complexity in synthesis, with the exception of liposomes, very few of them have aqueous cores. The fluid compartment of the shell can also be used to entrap fluorophores, drugs, proteins, and genes. A CaP coating can provide structural rigidity to an otherwise fragile liposome or emulsion. Solid CaP nanoparticles donot exhibit any immune response. Thus coating a liposome with this material could functionalize them to avoid reticulo endothelial system (RES) without the use of PEG.

3.6 Toxicological effect of nanoparticles used in drug delivery

Nanotechnology shows remarkable promises in the fields of medical sciences. However, the same properties, such as small size, chemical composition, structure, large surface area and

shape, which are so attractive in medicine, may influence their toxicological profile in biological systems. In fact, the smaller particles with higher surface area make them very reactive in the cellular environment. Because of this increased reactivity, the intrinsic toxicity of nanoparticle surface will be enhanced .[142] The respiratory system, blood, central nervous system (CNS), gastrointestinal (GI) tract and skin have been shown to be targeted by nanoparticles.

Nanoparticles can induce increased lung toxicity compared to larger particles with the same chemical composition at equivalent mass concentration. [144] It has been also shown that nanoparticles of different diameters can induce inflammatory reactions in the lungs of experimental animals. [145] Various types of nanoparticles can induce different inflammatory reactions. In fact, SWCNT has been found to be more toxic compared to other nanoparticles in inducing dose-dependent epithelioid granuloma and interstitial inflammation in lungs. [146] In addition, nanoparticle-induced pro-inflammatory reactions have been demonstrated in several *in vitro* models of exposure.[145] Therefore, these results indicate that nanoparticles can lead to inflammatory and granulomatous responses in lungs and this could have important implications for human risk assessment.

3.6.1 Nanoparticle translocation to the blood stream and central nervous system (CNS)

Nanoparticles can avoid normal phagocytic defenses in the respiratory system and gain access to the systemic circulation or even to the CNS. Once inhaled and deposited, nanoparticles can translocate to extrapulmonary sites and reach other target organs by different mechanisms. The first mechanism involves passing of nanoparticles across epithelia of the respiratory tract into the interstitium and access to the blood stream directly or via lymphatic pathways, resulting in systemic distribution of nanoparticles. Berry *et al*. showed for the first time that nanoparticles can be rapidly observed in rat platelets after intratracheal instillation of particles of colloidal gold

(30 nm).[147] Nemmar *et al*. (2002) also found that inhaled (99 m) Tc-labelled carbon particles (<100 nm) pass to the blood circulation 1 min after exposure. [148] In contrast, Brown *et al*. (2002) did not find an accumulation of the same radiolabel in the liver after exposure.[145] However, once nanoparticles are translocated into the blood stream they could induce adverse biological effects. The ability of mixed carbon nanoparticles and nanotubes, both MWCNT and SWCNT, to induce platelet aggregation *in vitro* has already been established.[149] Furthermore, it has been found that nanoparticles can directly induce cytotoxic morphological changes in human umbilical vein endothelial cells, induction of proinflammatory responses, inhibition of cell growth and reduction of endothelial nitric oxide synthase.[150] Inhibition of cell function and induction of apoptosis have also been reported *in vitro* in kidney cells treated with SWCNT.[151] The translocation of nanoparticles to CNS may not only take place as a result of systemic distribution. The other mechanism involves the uptake of nanoparticles by sensory nerve endings embedded in airway epithelia, followed by axonal translocation to ganglionic and CNS structures. In addition, nanoparticles can be taken up by the nerve endings of the olfactory bulb and translocated to the CNS. It has been found that C_{60} fullerenes can induce oxidative stress in the brain of large mouth bass via the olfactory bulb.[152] Recent studies have indicated that this translocation pathway is operational for inhaled nanoparticles. It has been shown that the exposure of rats to ^{13}C ultrafine particles (35 nm) for 6 h resulted in a significant increase of ^{13}C in the olfactory bulb on day 1 and this increase was even greater on day 7 post-exposure.[153] This result contrasts with 15-day inhalation of larger-sized MnO_2 particles in rats (1.3 and 18 μm median diameter) where no significant increase in olfactory Mn was found.[154] The latter observation could have been expected given that the individual axons of the fila olfactoria (forming the olfactory nerve) are only 100–200 nm in diameter. However, there are substantial

differences between humans and rodents and therefore, these results should be interpreted with caution. In humans, the olfactory mucosa comprises only 5% of the total nasal mucosal surface, whereas in rats this amounts to 50%. Interestingly, human studies have shown that elevated levels of Mn could be associated with increased rate of Parkinson's disease.[155] Recently, it has been found that exposure of PC-12 neuroendocrine cell line to nanosized Mn induced an increase in reactive oxygen species and dopamine depletion.[156] However, further studies are required to evaluate whether Mn nanoparticles can induce dopamine depletion *in vivo*.

3.6.2 Gastrointestinal tract (GI) and skin

GI tract and skin are the other two port of entries through which nanoparticles can get into the body. Nanoparticles can be ingested into the gut by many ways. For example, nanoparticles can be ingested directly from the food, water, drugs and cosmetics, but inhaled nanoparticles can also be ingested by GI tract once they are cleared by respiratory tract. It is known that the kinetics of particle uptake in GI tract depends on diffusion and accessibility through mucus, initial contact with enterocytes, cellular trafficking and post-translocation events. The smaller the particle diameter is the faster they could diffuse through GI secretion. Following uptake by GI tract nanoparticles can translocate to the blood stream and distribute all over the body. Recently, it has been shown that Cu nanoparticles administered via oral gavage can induce adverse effects and heavy injuries in the kidney, liver and spleen of experimental mice compared to micro-Cu particles.[157]

As with lungs, GI tract is easily exposed to stimuli that can induce an inflammatory response. Inflammatory bowel disease (IBD) that includes both ulcerative colitis and Crohn's disease (CD) is an inflammatory chronic condition whose aetiology remains still unclear.

However, several lines of evidence suggest that IBD can result from a combination of Genetic predisposition and environmental factors .[158] It has been shown that a diet low in Ca^{2+} and exogenous microparticles alleviated the symptoms of human CD with a significant improvement in the CD activity index.[159] These results are particularly relevant to CD as an abnormal intestinal permeability has been found in this disease. However, to our knowledge, no studies published to date showed direct toxicological effects of nanoparticles in GI tract.

Nanoparticles can be also taken up by lymphatic nodes at skin level, translocating to the blood been found that SWCNT can induce oxidative stress and pro-inflammatory responses in human keratinocyte cells *in vitro*.[151] However, no studies *in vivo* have been performed and therefore, more research is needed to investigate the effects of nanoparticles on skin.

3.6.3 Toxicological effects of CaP nanoparticles

Despite having many advantages, the use of CaP nanoparticles as controlled drug delivery system may involve some potential risks and health hazards. Increase in intercellular Ca^{2+} concentration can cause oxidative glutamate toxicity and ultimately leads to mitochondrial dysfunction. The impairment of mitochondrial function and perturbation of calcium homeostasis can cause cell death. Thus introduction of CaP nanoparticles into cell can lead to apoptotic cell death since it has been described that apoptosis is characterized by depolarization of mitochondrial membrane, [160] generation of reactive oxygen species (ROS) and increase of intracellular Ca^{2+} levels. [161]

Delivery of CaP nanoparticles into cells can promote formation of nanobacterium. Nanobacterium is a nano-organism that synthesizes a shell of CaP to cover itself, and resembles an inorganic CaP nanoparticle. The shell ranges in size between 20 to 300 nm. It allows the flow of a slimy substance through its pores in CaP shell. This slime promotes the adhesion to

biological tissues and the formation of colonies. Nanobacteria are very resilient, being temperature- and gamma radiation- resistant.[162] No other particle is known to manufacture such a calcified coating under human blood conditions, and until now medical science has never been able to prove why such calcification occurs in disease. Aside from being toxic on its own, the CaP layer binds proteins that have been implicated in disease. Calcifying nanoparticles have been detected in urine and kidney stones, bile and gall bladder stones, atherosclerotic plaques, heart valves, polycystic kidney disease cysts, liver cysts and human & fetal bovine serum.

3.7 Research objectives and plan

The objective of this research was to investigate whether protein loading and release from CaP nanoparticles can be controlled by varying particle size, morphology, specific surface area, and phase composition of CaP nanoparticles. The purpose behind controlling the drug delivery is to achieve more effective therapies while eliminating the potential for both under and overdosing. Other advantages of using controlled-delivery systems can include the maintenance of drug levels within a desired range, the need for fewer administrations, optimal use of the drug in question, and increased patient compliance.

Bovine serum albumin (BSA) was used as a model protein in this study. BSA loaded CaP nanoparticles were synthesized using both *ex situ* and *in situ* synthesis routes to see the effect of synthesis parameters in controlling protein release for longer period of time. The effect of dopant incorporation to *in situ* synthesized HA-BSA nanoparticles on the release of BSA was also investigated. Since bioresorbability and thus crystal dissolution of CaP nanoparticles depends on phase composition and crystallinity, efforts were made to control protein release from CaP nanoparticles by modifying their phase composition and crystallinity. The research has been focused on two different areas:

1. Synthesis of BSA loaded CaP nanopowders by *ex situ* and *in situ* process: CaP nanopowders with Ca:P molar ratio fixed at 1.5:1, were synthesized using reverse micelle as template system. Powders were calcined from 600 to 800 ^{o}C and characterized for phase composition, particle size, morphology, specific surface area. BSA was loaded onto CaP nanoparticle surface and adsorptive property of BSA was investigated with change in specific surface area of CaP nanoparticles and the pH of BSA-nanoparticle suspension.

2 mol% Zn and Mg doped HA-BSA nanopowders were synthesized by *in situ* precipitation route. Incorporation of BSA into HA nanopowders with change in dopant was investigated.

2. Study of BSA release from *ex situ* and *in situ* synthesized BSA-CaP nanoparticles: BSA loaded CaP nanoparticles were immersed in buffer solution of pH 7.2, 6 and 4, and then BSA release from these nanoparticles was evaluated as a function of elapsed time by BCA protein assay.

CHAPTER FOUR

SYNTHESIS OF NANOCRYSTALLINE HYDROXYAPATITE AND TRICALCIUM PHOPHATE POWDERS

4.1 Introduction

Hydroxyapatite ($Ca_{10}(PO_4)_6(OH)_2$, HA) and β-tricalcium phosphate (β-$Ca_3(PO_4)_2$, β-TCP) are the two calcium phosphate ceramics (CPCs) which have been mostly researched among the CPCs due to their promising biological responses to physiological environments.[163-167] HA is considered as a bioactive ceramic as chemically HA resembles closely to the inorganic part of human bone and shows excellent osteoconductivity.[165,166] β-TCP and HA implants become surrounded by new bone within a few weeks after implantation at bony sites in *vivo*.[168] β-TCP is considered as a bioresorbable ceramic. It gets gradually replaced by new, natural, fully functional bone by virtue of its extraordinary bioresorbability in biological environments.[168] TCP exists in two phases, namely α and β. The low temperature phase β is stable up to 1150 ^oC and structurally rhombohedral in its most abundant form, whereas α phase exists from 1150 ^oC to1430 ^oC and has monoclinic crystal structure. Synthesis of CaP powder in nanoscale is relevant in biological fields, because the dimensions of large biomolecules such as proteins and DNA as well as those of many important subcellular structures fall in the size range between 1 and 1000 nm.[169, 170]

4.1.1 Synthesis of CaP powders by different synthesis routes

A number of synthesis techniques have been used for the preparation of CaP powders, that can be divided into two broad categories, such as, solid-state process [171–174] and wet-chemical method.[175–179] Powder synthesized by solid-state process suffers from stoichiometrical inhomogeneity, wide particle size distribution and hard agglomeration which motivated

researchers to study wet chemical process for their synthesis. CaP nanopowders can be synthesized using different wet chemical synthesis routes which include wet precipitation[180], sol gel,[181] hydrothermal,[182] microemulsion [183] and surfactant based template system.[184]

Sol gel synthesis process of amorphous HA using calcium salts, ethanol and phosphoric acid was reported by Layrolle et al.[185] They showed that after calcination at 600 ^{o}C , amorphous calcium phosphate (ACP) was converted to crystalline HA. The average crystallite size of ACP was 22 nm, and that of HA was 200 nm. Water based sol gel synthesis of HA was investigated by Liu et al using calcium nitrate and triethyl phosphate. [186,187] The crystallite size was in the range of 8 to 10 nm and increase in temperature increased the crystallite size. Citrate nitrate combustion method for synthesis of nanocrystalline HA was reported by Han et al.[188] The reaction between citric acid and nitrate gives exothermic reaction which led to the formation of HA. They found a particle size in the range of 80 to 150 nm. Destainville et al. has investigated synthesis of β-TCP nanopowders by aqueous precipitation method using a solution of calcium nitrate, $Ca(NO_3)_2$, and ammonium dihydrogen phosphate, $(NH_4)_2HPO_4$, at neutral and alkaline pH with average specific surface area ranging from 89±2 to 95±2 m^2/g.[189] Pena et al. studied the synthesis of β-TCP by Pechini based liquid-mix technique using $CaNO_3.4H_2O$, $(NH_4)_2HPO_4$ and citric acid as precursor materials.[190] In these wet chemical synthesis routes the precipitate derived from aqueous solution is not of pure TCP, but apatitic TCP $Ca_9(HPO_4)(PO_4)_5(OH)$, which requires further calcination at temperatures between 700 and 800 ^{o}C to produce β–TCP phase. Bow et al. used anhydrous 99.5% methanol, instead of water to synthesize spherical β–TCP powders with an average particle size of 50 nm at 80 ^{o}C using calcium acetate and phosphoric acid.[191] In all those cases the synthesized β–TCP nanopowder showed agglomerated morphology with wide particle size distribution that affected powder properties.

Synthesis of nanocrystalline CaP powders using different surfactants and template system have been reported.[192-193] Uota et al. reported synthesis of HA nanopowders with very high surface area of 364 m^2/g using a mixed surfactant system.[192] Synthesis of HA nanocrystals using amino acid-capped gold nanoparticles has been studied by Rautaray et al.[193] A novel method of preparation of HA nanopowder was reported by Bose et al using sucrose templated sol gel technique.[184] Average particle size of synthesized HA nanopowders was 30 nm at 650 ^{o} C and increase in temperature increased the particle size. None of the aforementioned methods showed precise control over particle morphology as well as agglomeration. In the present case we report synthesis of CaP nanopowders using microemulsion technique with reverse micelle as template system.

4.1.1.1 Microemulsion

Microemulsions are true dispersions of liquid droplets, water or oil, in the size range between 10 nm and 100 nm within another immiscible liquid, oil or water, stabilized by a surfactant. Thus they are named as oil-in-water or water-in-oil microemulsion. In case of water-in-oil (w/o) microemulsion the heads and tails of surfactants orient themselves into water droplets and continuous hydrocarbon phase respectively, a phenomenon called reverse microemulsion. Micelles are perhaps the smallest of self assembled organic structures at approximately 4-5 nm in diameter. In an aqueous environment, micelles are formed when two ampiphiles with large head groups and narrow tails come in proximity and form a sphere with the tails pointing inwards as shown in **figure 4.1**. Conversely, in hydrophobic solvents the heads point inward, forming a reverse micelle. Reverse (or inverted) micelles are small, dynamic aggregates of surfactant molecules surrounding a polar (typically aqueous) core dispersed in a nonpolar continuous (oil) phase. Reverse micelle solutions are clear and thermodynamically

stable; as water is added to a reverse micelle solution, reverse microemulsion is formed that contains nanometer-sized water droplets dispersed in a continuous oil phase.

The apparent loss in entropy due to the ordering of ampiphilic surfactants is more than compensated by significant gain in entropy of solvent molecules. The increase in conformational and orientational degrees of freedom of solvent molecules due to the ordering of surfactant molecules is responsible for total gain in entropy in the system. This makes the process thermodynamically feasible. These spatially and geometrically restricted, self-assembling media of reverse micelles can be used in the synthesis of nanophase materials without much agglomeration to achieve high surface area as well as controlled particle size and morphology in final nanoparticle system.

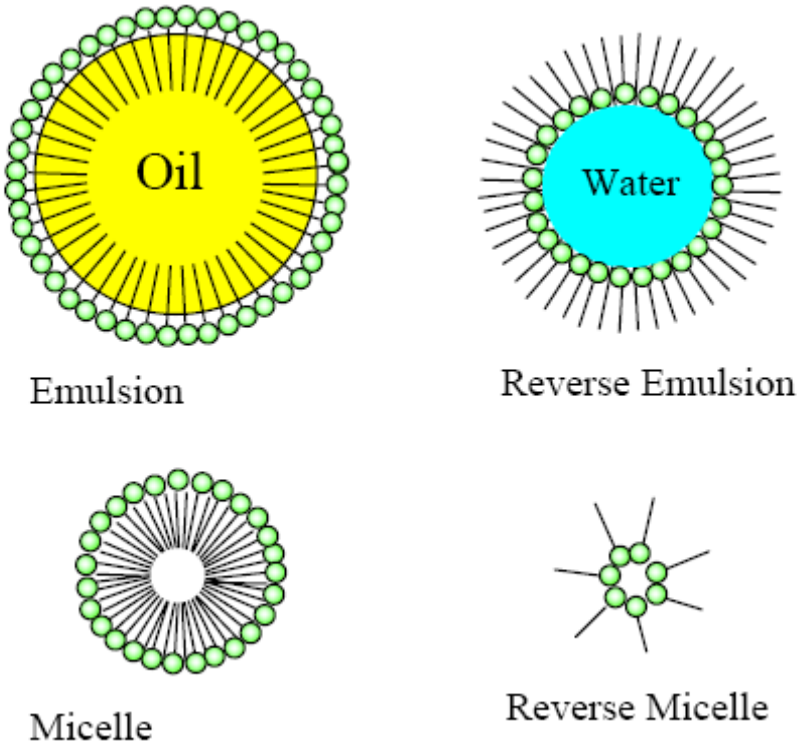

Figure 4.1 Cartoon of self assembled surfactant systems that form in an oil-in-water or a water-in-oil (reverse) system.

Synthesis of HA nanopowder using nonionic surfactant organized in a micelle based template was reported by Lim etal [194,195] Ultrahigh-aspect-ratio HA nanofibers using reverse micelles system consisting of cetyltrimethylammonium bromide (CTAB)/cyclohexane/n-pentanol/water have been synthesized by Cao et al.[196] Sun et al. studied reverse microemulsion directed synthesis of HA nanoparticles crystallized under hydrothermal conditions using cetyltrimethylammonium bromide (CTAB) surfactant.[197] They found significant effect of surfactant (CTAB) on morphology of synthesized HA nanoparticles. Bose et al. reported both micelle and reverse micelle based microemulsion templated synthesis of HA nanopowders.[184, 198,

Here we report synthesis of nanocrystalline HA and β-TCP powders with different aspect ratio using reverse micellization technique. The surfactant that was used to stabilize the microemulsion, was an ether based neutral surfactant chemically named as polyoxyethylene(n) nonylphenyl ether. The structural formula of polyoxyethylene(n) nonylphenyl ether is shown in **figure 4.2**. Depending on the number of carbon (n=5, 12) in the ether chain it is termed as NP-5 or NP12. The molecular chain linked to ether linkage was hydrophilic and formed the head of the surfactant oriented towards the center of the aqueous core. The hydrocarbon chain attached to cyclohexane ring was hydrophobic and projected toward continuous oil phase of cyclohexane.

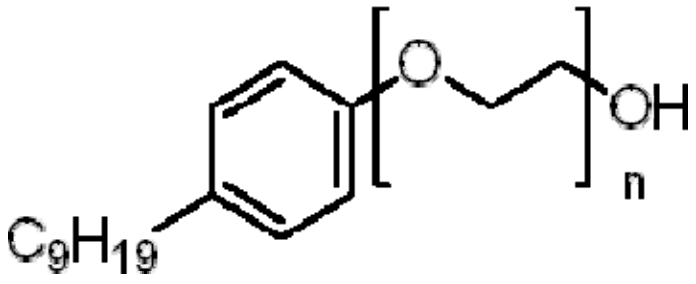

Figure 4.2 Structural formula of the surfactant, polyoxyethylene(n) nonylphenyl ether, used to prepare reverse micelle. when n=5, NP-5; when n=12, NP-12.

Powder particle size and morphology were controlled by varying different synthesis parameters such as aqueous to organic phase volume ratio, nature of surfactant, pH of the reaction mixture, aging or ripening time of the reaction. Powders were characterized using X-ray diffraction (XRD), Fourier transformation infrared (FTIR) spectroscopy, dynamic light scattering (DLS) technique, transmission electron microscopy (TEM) and Brunauer, Emmett and Teller (BET) surface area analysis.

4.2 Experimental

4.2.1 Materials:

For synthesis of HA and β-TCP nanopowder, calcium nitrate ($Ca(NO_3)_2.4H_2O$, J. T. Baker, Phillipsburg, NJ) and orthophosphoric acid (H_3PO_4, Fisher Scientific, Fair Lawn, NJ) were used as source of Ca^{2+} ion and PO_4^{3-} ion, respectively. Cyclohexane (J. T. Baker, Phillipsburg, NJ) was used as organic solvent. Poly $(oxyethylene)_5$ nonylphenol ether (NP-5, Sigma Aldrich, St. Louis, MO) poly$(oxyethylene)_{12}$ nonylphenol ether (NP 12) (Sigma-Aldrich, St. Louis, MO) were used as surfactant. Ammonium hydroxide (NH_4OH, J. T. baker, Phillipsburg, NJ) was used to adjust the pH of the emulsion system.

4.2.2 Synthesis of HA nanopowders:

HA nanopowders were synthesized using a standard method established in our laboratory.[183] 5 M aqueous solution of Ca^{2+}-ion was prepared by dissolving 0.01 moles (2.362 g) of $Ca(NO_3)_2$, $4H_2O$ in 2 ml distilled water. 0.006 moles (0.686 g) of phosphoric acid (H_3PO_4) (85.7%) was added to the system to maintain Ca to P molar ratio 1.67. Organic phase was prepared by addition of 10 vol% surfactant (NP12) in cyclohexane with vigorous stirring. HA nanopowder was synthesized at aqueous to organic ratio (A/O) of 1:15 by mixing aqueous and organic phase in that proportion and pH of the medium was adjusted to 9 with dropwise addition

of NH_4OH to initiate reaction between $Ca(NO_3)_2$, $4H_2O$ and H_3PO_4 to form HA nanocrystals. All reactions were aged for 24 h at room temperature to grow non-agglomerated HA nanocrystals with high crystallinity. After aging, the emulsion was evaporated on the hot plate at 150 ^oC followed by complete drying at 450 ^oC. Dry precursor powder was calcined at 650 ^oC for 4 h to get carbon free crystalline HA nanopowder.

4.2.3 TCP nanopowder synthesis:

First a 5 M Ca^{2+} solution was prepared by dissolving 0.01 moles (2.632 g) of $Ca(NO_3)_2.4H_2O$ in 2 ml distilled water. The mole ratio of Ca to P was maintained at1.5:1.0 by dropwise addition of 0.0066 moles (0.767 g) of H_3PO_4 into it. Surfactants, poly $(oxyethylene)_5$ nonylphenol ether (NP-5) and /or poly $(oxyethylene)_{12}$ nonylphenol ether (NP-12) were added dropwise to the extent of 10 volume% to cyclohexane with constant stirring to prepare the organic phase. The aqueous phase was then mixed with the organic phase in different aqueous to oil volume ratio (1:05, 1:10,1:15) by constant stirring for 30 min on a hot plate to make a water-in- oil emulsion. The pH of the emulsion was adjusted to 10 by slow addition of 90% concentrated NH_4OH to the reaction mixture to initiate the reaction between $Ca(NO_3)_2.4H_2O$ and H_3PO_4. The emulsion was converted into a transparent gel during mixing. The reaction mixture was aged at room temperature for 12 h and dried on a hot plate at 300 ^oC followed by calcination at 800 ^oC for 4 h in a muffle furnace to obtain carbonaceous residue free nanocrystalline TCP powders.

4.2.4 Phase composition, particle size, morphology, and surface area of the CaP nanoparticles

4.2.4.1. Powder x-ray diffraction (XRD) of the nanoparticles

The phases of synthesized CaP nanoparticles calcined at 600, 650, 700 and 800 ^{o}C were determined using a Philips fully automated x-ray diffractometer with Cu-K_{α} radiation (1.54018 A) and a Ni- filter. The diffractometer was operated at 35 kV and 30 mA. The XRD data were collected at room temperature over the 2θ range of 20^{o}-60^{o} at a step size of 0.02^{o} and a count time of 0.5 s/step. The crystallite size was determined from the x-ray peak broadening at half maxima. If the peak in XRD has a width B_o at half maxima and width due to instrumental broadening is B_i, then the remaining width B_r is due to crystallite size and lattice strain. When the nature of the peak is not clear i.e. whether the peak has Lorentzian or Gaussian profile, the following equation can give a more correct value of B_r.

$B_r = [(B_o - B_i)(B_o^2 - B_i^2)^{1/2}]^{1/2}$

The value of B_r depends on crystallite size and lattice strain. But at smaller value of θ, the value of B_r mostly depends on crystallite size. Therefore at lower value of θ, the crystallite size (L) can be directly calculated using the equation $L = K\lambda / B_r \cos(\theta)$, where K is constant equal to 0.9, λ is the wavelength of X-ray and θ is the half of the diffraction angle. In the present case, the crystallite size of synthesized β-TCP nanopowders was calculated from (0210) peak.

4.2.4.2. Dynamic light scattering (DLS)

Particle size of synthesized CaP nanoparticles was measured by DLS technique using NICOMP^{TM} 380 (Santa Barbara, CA, USA) particle size analyzer. 0.002 gm CaP powder was added to 50 ml of water at pH-10 and ultrasonicated for 15 min to minimize the degree of agglomeration. The aqueous suspension of CaP nanoparticles at pH-10 was stable against

flocculation for long time under the influence of strong electric double layer repulsion around the negatively charged particle surface. The particle suspension was filled in a 6 x 50 mm size borosilicate glass tube and inserted in NICOMP^{TM} 380 chamber for particle size analysis. The particle sizes were automatically determined from the autocorrelation function using the Stokes–Einstein equation: $r = kT/ 6D\pi\eta$, where r is the particle radius, k is the Boltzmann constant, T is the absolute temperature, D is the diffusion coefficient, and η is the viscosity of the liquid in which the particles were suspended. The values for the above parameters at room temperature were[199], k =1:38 x 10^{-23} m^2 kg s^{-2} K^{-1}, T = 293K, η= 0:891 cP.

4.2.4.3. Transmission electron microscopy

A very dilute aqueous suspension of CaP nanoparticles in water was prepared following aforementioned method. One drop, approximately 5 µl, of particle suspension was deposited onto a formvar coated Cu grid (Ted Pella, Inc.) and allowed to equilibrate for 3 min. The grids were then allowed to air dry. Images were taken using a JEOL, JEM 120 (MA, USA) transmission electron microscope (TEM) set to an accelerating voltage of 100 kV.

4.2.4.4. Brunauer, Emmett and Teller (BET) surface area analysis:

The BET theory is the most popular model used to determine surface area. Samples are commonly prepared by heating while simultaneously evacuating or flowing gas (N_2) over the sample to remove moisture and organic impurities from the surface of the particles. The samples are then cooled with liquid nitrogen and analyzed by measuring volume of gas (typically N_2 or Ar) adsorbed on particle surface at specific pressures. The volume (V) of gas adsorbed is measured at a fixed temperature for different pressures P. A graph of V vs P, referred to as adsorption isotherm, is plotted. If the gas is at pressure below its saturation vapor pressure P_o, then the relative pressure P/ P_o is used instead of P. Further manipulation of the adsorption data

gives monolayer capacity V_m, defined as the amount of gas required to cover the surface of the powder with a monolayer, from which surface area is obtained. The important equation for the BET adsorption isotherm is expressed in the form of $1/ (V(P/ P_o -1) = 1/V_mC + (C-1)/ V_mC (P/ P_o)$, where C is a constant. A plot of $1/ (V(P/ P_o -1)$ vs P/ P_o gives a straight line with slope (S) and intercept (I) are given by, $S= (C-1)/ V_mC$ and $I= 1/V_mC$.

Therefore, the monolayer volume V_m can be calculated as $V_m= 1/(S+1)$.

Finally, the specific surface area S_w is obtained from the equation $S_w= N_A \sigma Vm/ V_o$, where N_A is the Avogadro's number, s is the area of adsorbed nitrogen gas molecule and V_o is volume of 1 mol of gas at STP.

In this experiment approximately 0.5 gm of CaP nanopowders was taken in a round bottom glass tube and heated at 350 C for 4 h to drive out any moisture in it. After cooling in air tight condition the round bottom glass tube containing CaP nanopowders was put inside a chamber three quarter filled with liquid nitrogen. Specific average surface area of powders was determined by the BET method (5 points analyzer, Tristar Micromeritics, USA) with a continuous flow of nitrogen. Three samples from each powder were used for BET surface area measurement and data were represented as mean ± standard deviation.

4.2.4.5. FTIR analysis of CaP nanoparticles

Fourier transform infrared spectroscopy (FTIR) was conducted on CaP nanoparticles synthesized at different calcination temperature. For this, 1mg of each of the synthesized powders was put on an ATR (attenuated total reflection) diamond crystal and pressed with an indenter so that powder could remain in contact with ATR diamond crystal. The FTIR spectra of these samples were then obtained using a FTIR spectrophotometer Nicolet 6700 FTIR (Madison,

WI, USA). Before every measurement a background FTIR spectra was taken and deducted from the sample spectra. All of the spectra were collected in the 400–4000 cm $^{-1}$ wavenumber range.

4.2.4.6 Statistical Analysis

Aspect ratio data for all powders were analyzed with SAS 9.1 statistical package (Cary, NC , USA)[200] using one way analysis of variance (ANOVA) and Tukey's method for pairwise multiple comparison was carried out at a significance level of p=0.05 to find out the differences in aspect ratio of β-TCP nanopowders with variation in synthesis parameters.

4. 3 Results

4.3.1 Characterization of HA nanopowders

Figure 4.3 shows the x-ray diffraction pattern of synthesized HA nanopowders. The synthesized HA nanopowders exhibited phase pure HA according to JCPDS 09-0432.

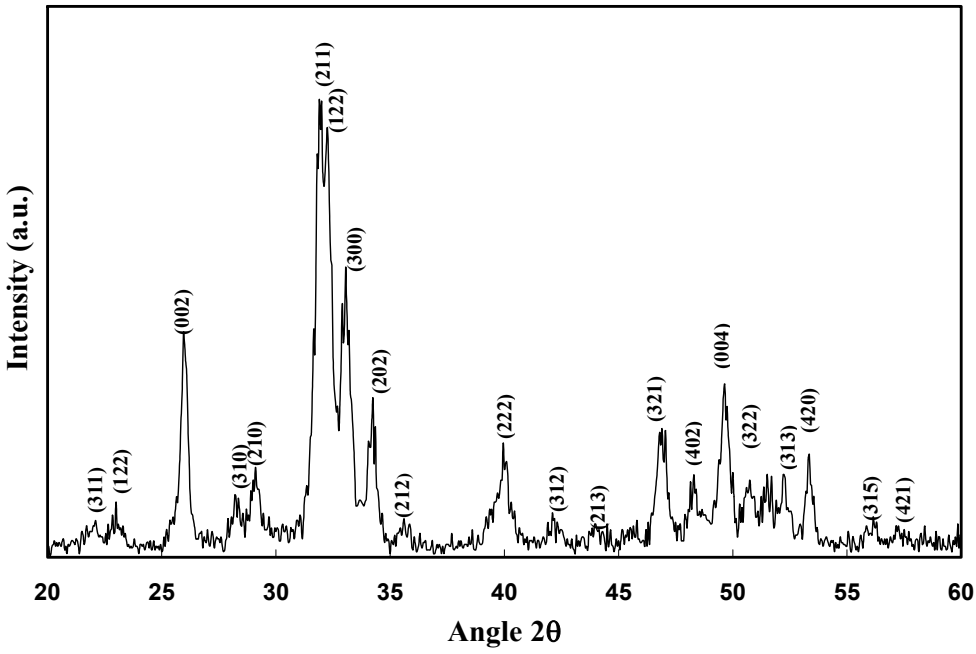

Figure 4.3: X –ray diffraction pattern of synthesized HA nanopowders

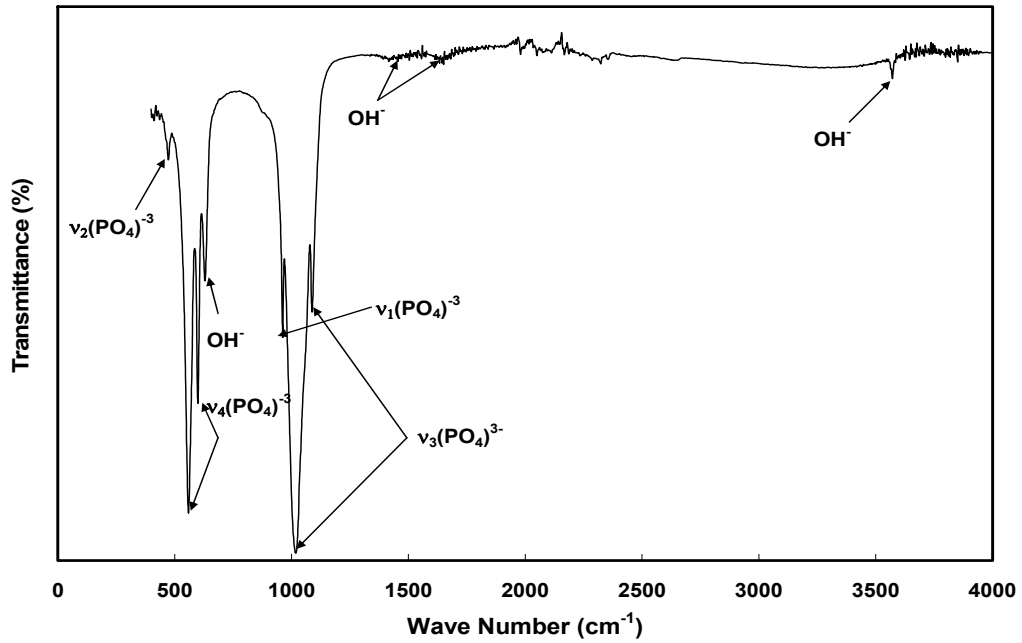

Figure 4.4: FTIR spectra of synthesized HA nanopowders

The FTIR spectra for HA nanopowders contained various bands from the respective phosphate and hydroxyl groups of HA as indicated in **figure 4.4**, which were in agreement with other reported results.[201, 202] The bands at 1020 and 1085 cm^{-1} were assigned to the components of the triply degenerate ν_3 antisymmetric P–O stretching mode. P–O symmetric stretching mode was detected at 962 cm^{-1}. The bands at 599 and 563 cm^{-1} were attributed to components of the triply degenerate ν_4 O–P–O bending mode and the doubly degenerate ν_2 O–P–O bending mode was evident at 475 cm^{-1}. Characteristic bands corresponding to the hydroxyl group was observed at 631, 1457, 1668 and 3572 cm^{-1}.

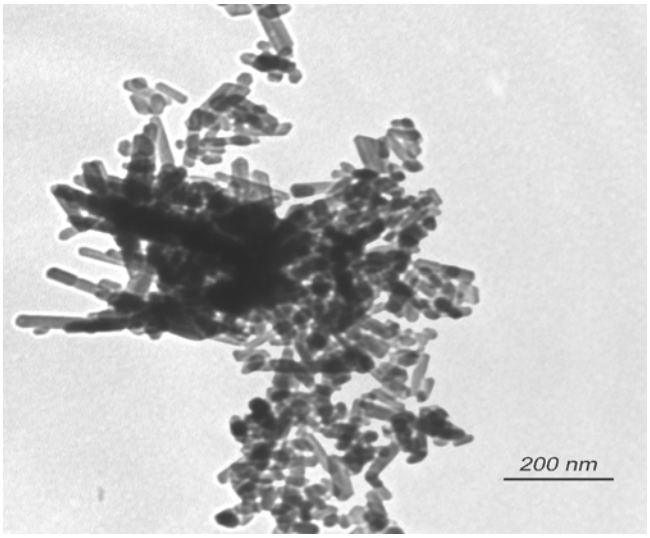

Figure 4.5: TEM micrograph of synthesized HA nanopowders

Figure 4.5 shows the TEM micrograph of synthesized HA nanopowders. The aspect ratio of synthesized HA nanoparticle was found to be 4.28±0.59. The size distribution of synthesized HA nanoparticles was between 35 to 90 nm. The number average particle size from DLS measurement was found to be 52 nm as depicted in **figure 4.6**.

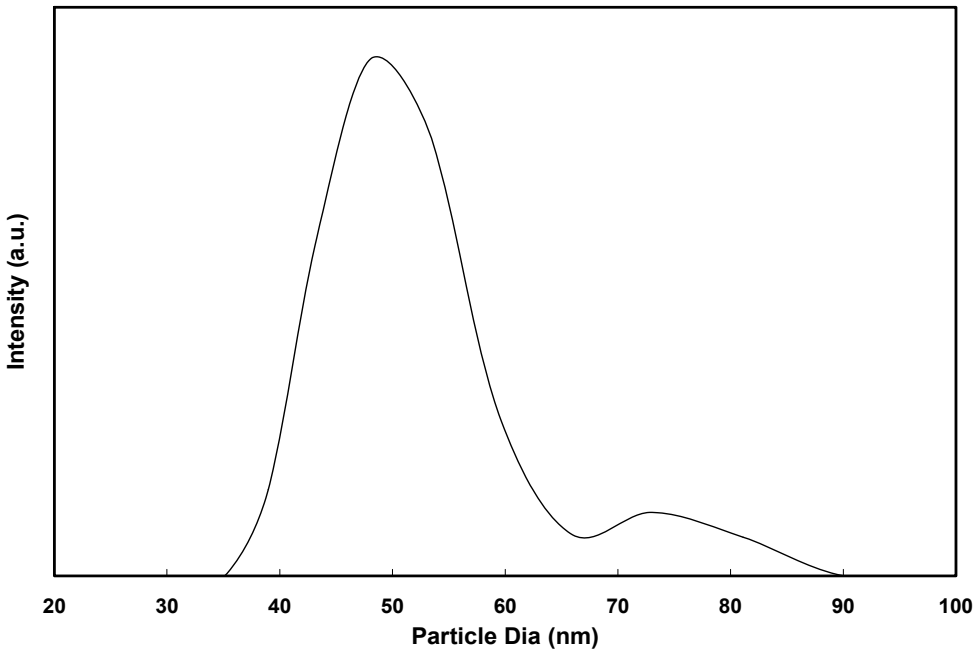

Figure 4.6: Particle size distribution of synthesized HA nanopowders

4.3.2 Characterization of β-TCP nanopowders

4.3.2.1 Phase identification and evolution

Figure4.7 shows the x-ray diffraction (XRD) pattern of synthesized nanopowders using NP-12 surfactant with aqueous to organic ratio (aq:org ratio) of 1:15 in the reaction mixture, calcined at different temperatures at 600, 700 and 800 ^{o}C for 3 h. The XRD patterns obtained from the powders calcined at 600 and 700 ^{o}C mostly resembled with that of calcium deficient hydroxyapatite (CDHA) phase which is consistent with the earlier reports.[203]

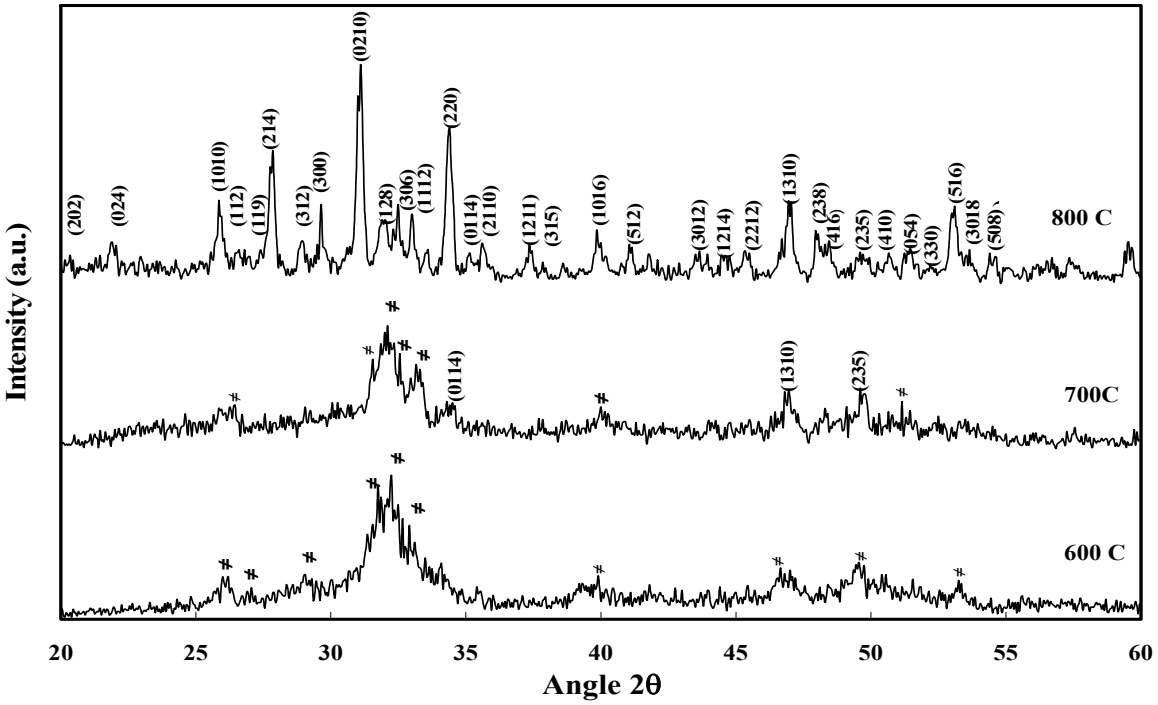

Figure 4.7: XRD pattern of synthesized powders calcined at different temperatures. # - CDHA, ( )- β-TCP

All powders were calcined at 800 ^{o}C and their XRD exhibited β-TCP as the major phase (JCPDS No 9-169), shown in **figure 4.8**. The crystallite size was calculated using the (0210) peak of highest intensity in the XRD patterns on the basis of Debye-Scherrer equation.

Irrespective of the nature of surfactant used, with decrease in aqueous content in the reaction mixture the (0210) peak of the synthesized powders became broader.

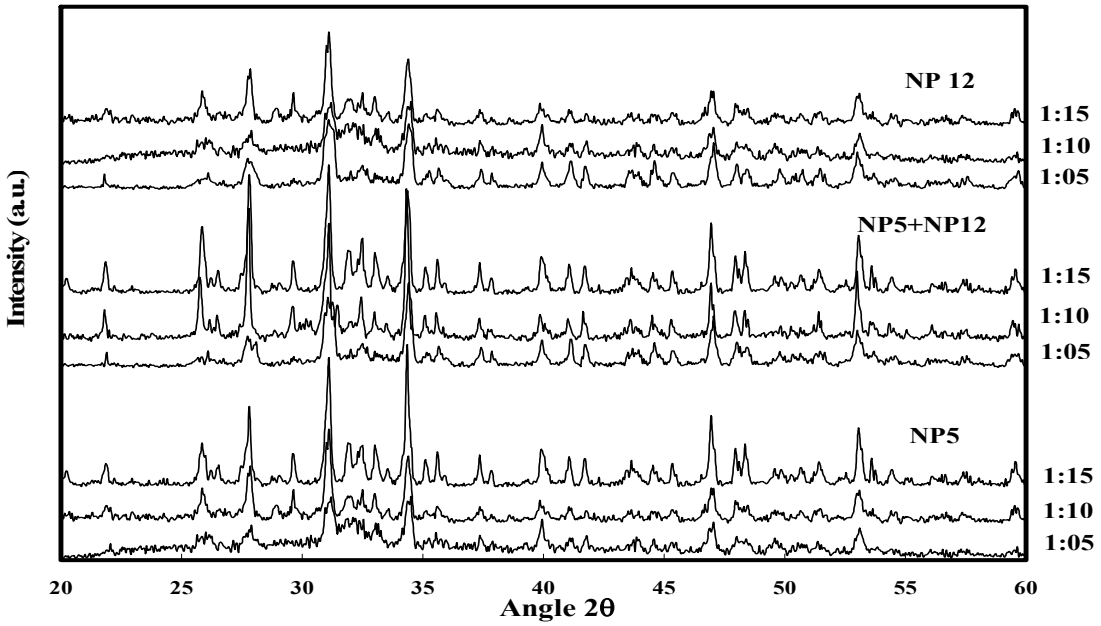

Figure 4.8: XRD pattern of the synthesized powders calcined at 800 ^{o}C for 4 h

Figure 4.9 shows the change in powder crystallite size with aq:org ratio in the reaction mixture. Crystallite size of synthesized β-TCP powder decreased with increase in organic content in the reaction mixture.

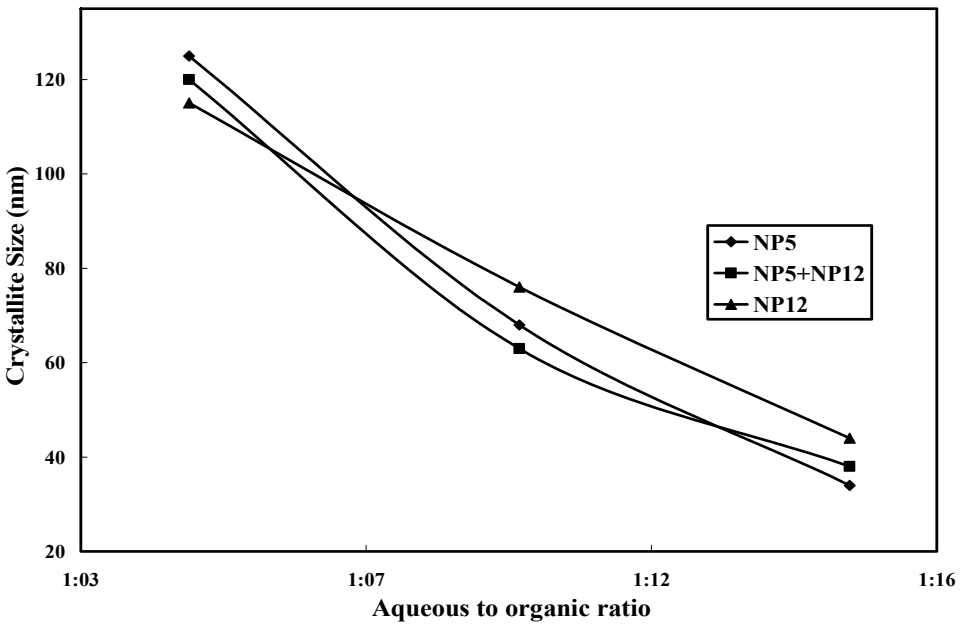

Figure 4.9: Change in crystallite size of synthesized β-TCP nanopowders with variation in aqueous to organic phase ratio in the microemulsion

The nature of surfactant did not have significant effect on the phase formation of calcined β-TCP powders. This is also revealed from FTIR analysis. **Figure 4.10** illustrates the FTIR spectroscopy of synthesized nanoscale TCP powders using different surfactants at a fixed aq:org ratio of 1:15 and calcined at 800 ^{o}C. β-TCP phase can be identified by the large band at 900–1200 cm^{-1}.[201, 203] The bands at 1022 and 1120 cm^{-1} are assigned to the components of triply degenerate ν_3 antisymmetric P–O stretching mode. ν_1, the non degenerate P–O symmetric stretching mode, is detected at 972 cm $^{-1}$. The bands at 606 and 544 cm^{-1} are attributed to components of the triply degenerate ν_4 O–P–O bending mode and the doubly degenerate ν_2 O–P–O bending mode is evident at 438 and 498 cm^{-1}. The absence of any characteristic bands at 631 and 3572 cm $^{-1}$ corresponding to the hydroxyl group denies the presence of any hydroxyapatite phase in 800 ^{o}C calcined powders.[202, 203]

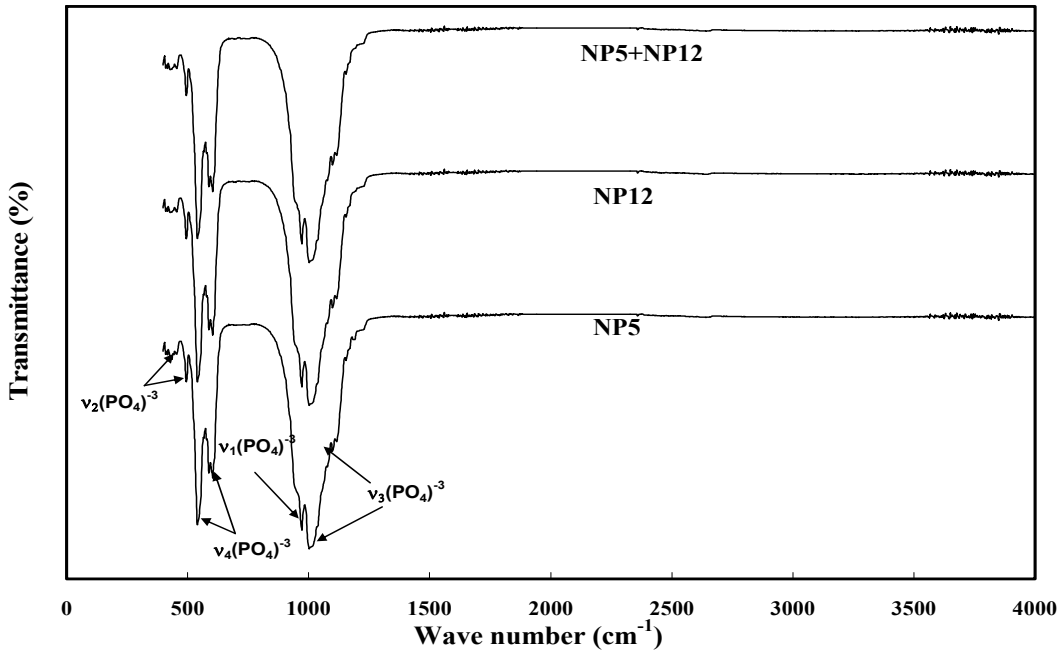

Figure 4.10: FTIR spectroscopy of powders synthesized using surfactant at a fixed aqueous to organic phase ratio of 1:15 in the reaction mixture.

4.3.2.2 Change in particle size, morphology and surface area

To study the effect of synthesis parameters on particle size, morphology and BET surface area, TCP powders were synthesized by varying aq:org ratio from 1:05 to 1:15 using surfactants NP5, NP12 and a mixed type, NP5+NP12 in 1:1 volume ratio, maintaining a constant aging time of 12 hours and pH 10 in the reaction mixture. **Figure 4.11** illustrates the NICOMP number average particle size distribution of nanopowders as a function of aq:org ratio and calcined at 800 ^{o}C for 4 h.

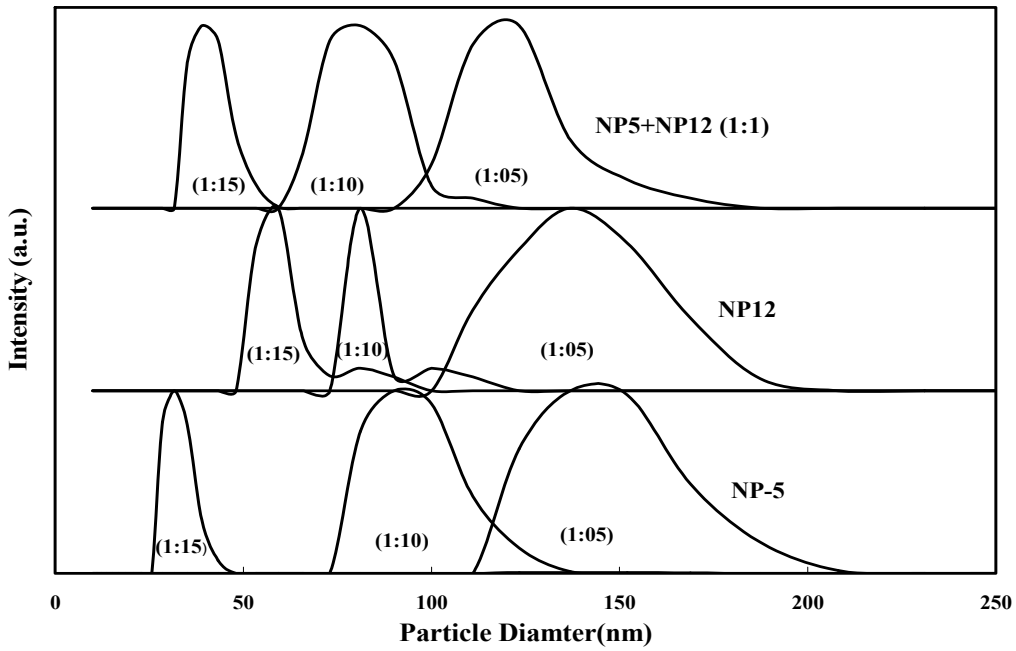

Figure 4.11: Variation in Particle Size of the synthesized powders with change in aqueous to organic ratio in the reaction mixture.

Change in BET specific average surface area of TCP nanopowders synthesized using different surfactants and aq:org ratio is shown in **figure 4.12**. The lowest particle size of 32 nm with NP-5 surfactant and 1:15 aq:org ratio showed the highest BET surface area of 103 m^2/g. Both figures 4.11 and 4.12 show that the synthesized powders had a gradual decrease in particle size and an increase in BET surface area with increase in organic content in the reverse micelle. Powders synthesized with fixed aq:org ratio of 1:05 using NP-5 surfactants showed the highest number average particle size of 135 nm ,but not necessarily the lowest BET surface area of all the synthesized powders. BET surface area was the lowest, ~57 m^2/g, for the powders with number average particle size of ~110 nm synthesized with NP5+NP12 a mixed surfactant system at aq:org ratio of 1:05.

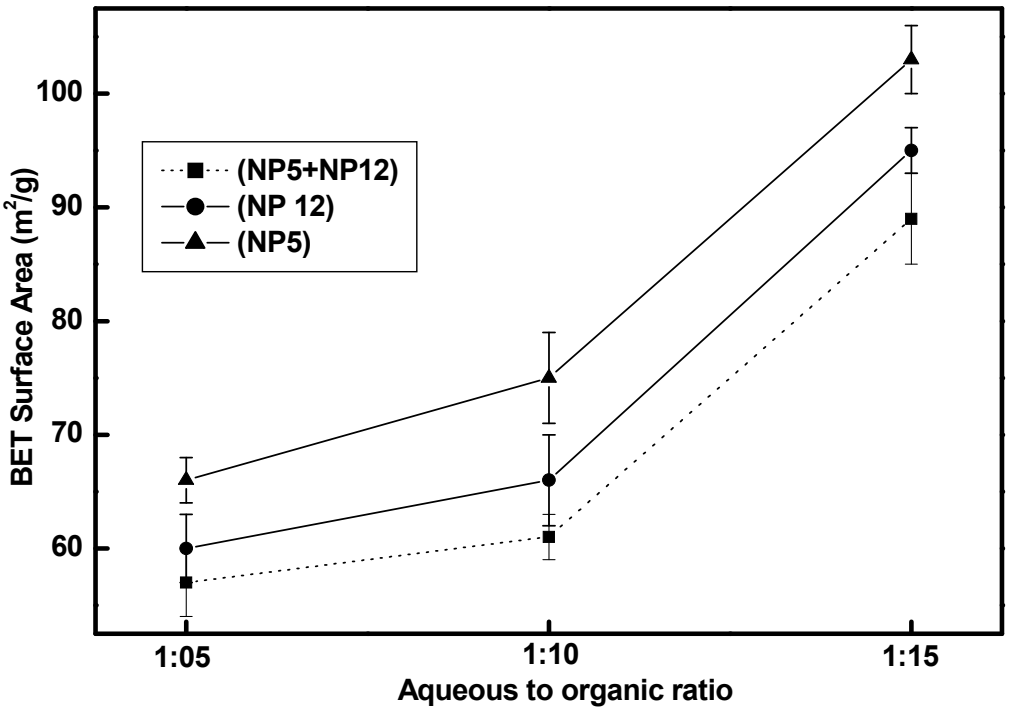

Figure 4.12: Change in surface area of the synthesized powders as function of aqueous to organic ratio in the reaction mixture.

TEM micrographs of TCP nanoparticles synthesized at a fixed aq: org ratio of 1:15 using surfactants NP5, NP12 and 1:1 mixture of NP5 and NP12 by volume are shown in **figures 4.13 a, b and c** respectively. The aspect ratio of particles was calculated from TEM images and shown in **tables 4.1 and 4.2**. No outlier was found within $\pm\sigma$ for any powder. Powders synthesized using NP5 and mixed surfactant of NP5 + NP12 gave particles with lower aspect ratio of 1.1 ± 0.15 and 1.3 ± 0.2 respectively which were not ($p=0.6714$) significantly different. Elongated β-TCP particles with aspect ratio of 3.9 ±0.4 were obtained for powders synthesized using NP12 surfactant which were significantly different in aspect ratio from β-TCP particles synthesized using NP5 ($p < 0.0001$) and NP5+NP12 ($p < 0.0001$).

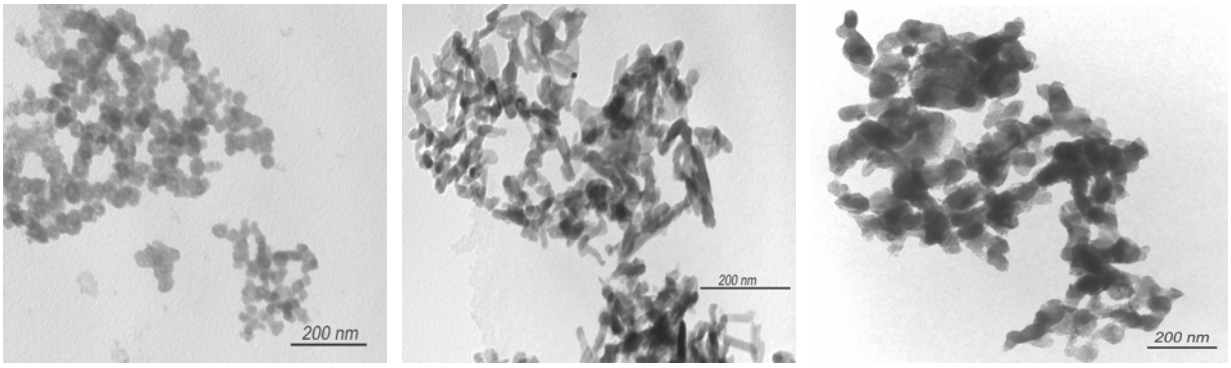

(a) (b) (c)

Figure 4.13: TEM micrographs of β-TCP particles synthesized at fixed aqueous to organic phase composition using different surfactant (a) NP-5 (b) NP-12 and (c) NP5+NP12

Table 4.1: Aspect ratio of synthesized TCP nanopowders using different surfactant at a fixed aq:org ratio of 1:15 in reaction mixture

Surfactant	**Aspect Ratio**
NP5	1.1 ± 0.15
NP12	3.9 ± 0.4
NP5+NP12	1.3 ± 0.2

(a) $p < 0.0001$ for NP5 Vs NP12 (b) $p < 0.0001$ for NP12 Vs NP5 + NP12 and (c) $p = 0.6714$ for NP 5 Vs NP5 + NP12

Figures 4.14a, b and c show the TEM micrographs of β-TCP powders synthesized using NP-12 surfactant varying aqueous to organic phase composition in microemulsion. It is evident from table 2 that with increase in aqueous content in reaction mixture the particles became more and more spherical. The aspect ratio of β-TCP nanopowders synthesized at aqueous to organic phase composition of 1:15, 1:10, and 1:05 were 3.9± 0.4, 2.4 ± 0.5 and 1.5 ± 0.4 respectively. In this case, significant variation aspect ratio of β-TCP nanopowders was found as the aqueous to organic phase composition in microemulsion was varied from 1:15 to 1:10 ($p=0.0002$), 1:15 to 1:05 ($p < 0.0001$) and 1:10 to 1:05 ($p=0.0044$).

Table 4.2: Aspect ratio of TCP nanopowders synthesized using NP12 surfactant varying the composition of microemulsion

Aqueous to organic ratio	Aspect ratio
1:15	3.9 ± 0.4
1:10	2.4 ± 0.5
1:05	1.5 ± 0.4

(a) p =0.0002 for 1:15 Vs 1:10 (b) p <0.0001 for 1:15 Vs 1:05 and (c) p =0.0044 for 1:10 Vs 1:05

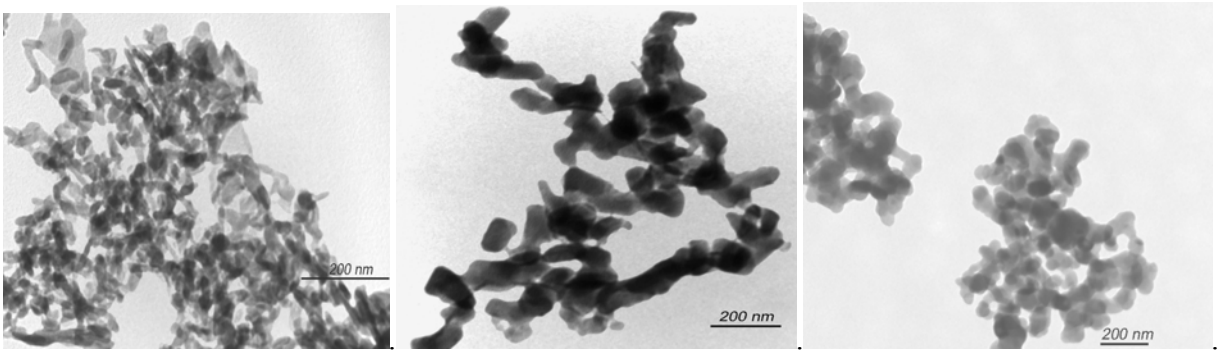

(a) (b) (c)

Figure 4.14: TEM micrographs of β-TCP particles synthesized by using NP-12 surfactant with varying aqueous to organic phase ratio in the reaction mixture (a) 1:15 (b) 1:10 and (c) 1:05.

4.4 Discussion

The precipitates obtained from the aqueous solution was a non-stoichiometric apatite with chemical formula of $Ca_{10-x}(HPO_4)_x(PO_4)_{6-x}(OH)_{2-x}$ $(0 \le x \le 1)$ where Ca/P molar ratio can vary from 1.33 to 1.65. Ca:P molar ratio of 1.5:1 represents TCP. When x=1 the above mentioned general formula becomes $Ca_9(HPO_4)(PO_4)_5(OH)$ which is called calcium deficient apatite (CDHA) phase. This CDHA transformed into β-TCP on heating at and above 800 ^oC according to following equation.[175]

$Ca_9(HPO_4)(PO_4)_5(OH) \rightarrow 3\ Ca_3(PO_4)_2 + H_2O$……..(1)

.

In reverse micelle based synthesis, powder morphology is directly related to the shape of nuclei formed during reverse micellization and it's change during synthesis. The shape of the polar core in the reverse micelle domain is governed by two mutually opposing forces (a) an attractive force due to the hydrophobic attraction of the hydrocarbon chain units at the hydrocarbon-water interface, and (b) a repulsive force between the adjacent head groups with similar charge characteristics due to hydrophilic, steric and ionic repulsion. The droplets of water that were stabilized by surfactants act as nanoreactors where hydroxyl ions from NH_4OH decreased the solubility product of calcium deficient apatite [$Ca_9(HPO_4)(PO_4)_5(OH)$] which gradually grew on aging. The chemical reaction that occurred inside the nanodroplets of water is as follows.

$$Ca(NO_3)_2 + 6\ H_3PO_4 + 18\ NH_4OH = Ca_9(HPO_4)(PO_4)_5(OH) \downarrow + 18\ NH_4NO_3 + 17\ H_2O \ldots\ldots (2)$$

With increase in organic content in microemulsion the size of polar core in reverse micelle domain decreased resulting in a decrease in crystallite size as well as particle size of synthesized β-TCP powders. Surface area of synthesized nanopowders depended not only on particle size, but also on particle morphology and inherent porosity of particles, the fact is well reflected in the finding that synthesized β-TCP powders with the lowest particle size didnot show the lowest surface area.

Both hydrocarbon chain length of surfactant and aq:org ratio in the reaction mixture had effect on morphology or aspect ratio of synthesized powders. Polar core size in the reverse micelle domain was smaller for the lowest aqueous content in the reaction mixture. Separation distance between the hydrocarbon chain units was minimum when they oriented themselves around the spherical hydrophilic core. This caused an increased hydrophobic attraction between C5, C5+C12 hydrocarbon tails of NP5 and NP5 + NP12 surfactants and dominated over the ionic

or hydrophilic repulsion between the closely packed heads groups. Thus the nuclei formed during reverse micellization synthesis process using NP5 and NP5 + NP12 surfactants became more spherical with the lowest water content in microemulsion resulting in β-TCP nanoparticles with lower aspect ratio as shown in **Figure 4.13a and 4.13c**. In case of powders synthesized using only NP 12 surfactant, long C12 carbon chains needed bigger surface area to orient them around hydrophilic core of reverse micelle. This may result in formation of nuclei with higher aspect ratio and thus particle morphology became elongated for powders synthesized using NP12 surfactant at the lowest aqueous content in microemulsion. As water content in the microemulsion increased both steric hindrance from C-12 hydrocarbon chains and repulsion between the hydrophilic head groups decreased and by doing so, reverse micelle domain became more and more spherical. As a result, with change in aq:org ratio from 1:15 to 1:10 and then to 1:05 in the reaction mixture the aspect ratio of β-TCP nanopowders synthesized using NP12 surfactant gradually decreased, as reflected in **Table 4.2** and **Figure 4.14**.

4.5 Summary

The key objective of this work was to synthesize nanocrystalline HA and β-TCP powders using reverse micelle as template system. In the previous work in our laboratory, Saha et al. studied the effect of different parameters in reverse microemulsion on physicochemical properties of HA nanopowders.[183] He extensively studied the effect of composition of microemulsion, chemical nature of surfactant, aging time of reaction mixture, pH, and calcination temperature on particle size, morphology, surface area, phase composition and crystallinity of synthesized HA nanopowders. My present work was an extension to his research results for TCP nanopowder synthesis using microemulsion system. The stiochiometric Ca to P molar ratio of HA is 1.67:1, whereas that for TCP is 1.5:1. Though I have synthesized HA

nanopowders using the same synthesis route for fabrication of sintered nanostructured HA comapcts, the primary objective of my work was to study physicochemical properties of synthesized β-TCP nanopowders with variation in reaction parameters, such as aqueous to organic composition in reaction mixture, hydrocarbon chain length of the surfactant in reverse microemulsion. The key conclusions from this works are as follows.

- Phase pure HA nanoparticles with size varying between 35 and 90 nm were synthesized.
- Nanocrystalline β-TCP powders were synthesized with number average particle size between 30 nm to 135 nm and average aspect ratio between 1.1 and 3.85 by varying aqueous to organic phase composition and hydrocarbon chain length of the ether based surfactant.
- At a fixed aqueous to organic composition of 1:15, the β-TCP nanoparticles synthesized using NP-5 surfactant showed the lowest particle size, whereas the nanoparticles synthesized using NP-12 surfactant showed the highest aspect ratio.
- Depending on synthesis parameters, average specific surface area of synthesized β-TCP powders varied between 57 and 103 m^2/g.
- Particle size of synthesized TCP powders decreased with increase in organic cyclohexane content in the reaction mixture irrespective of the nature of surfactant used.

β-TCP being a bioresorbable ceramic, offers significant opportunities in the fields of tissue engineering and drug or biomolecule delivery system. Bioresorbability of β-TCP nanopowders can be tailored by varying particle size, morphology, surface area, and crystallinity. Thus synthesis of β-TCP nanopowders with different particle size, morphology and surface area finds validity for hard tissue regeneration and carrier for controlled release of biomolecule and drugs.

CHAPTER –FIVE

PROTEIN DELIVERY USING DOPED AND UNDOPED TCP, CDHA AND HA NANOPARTICLES

5.1. Introduction

The prospect of cellular delivery involving the transfer of various drugs and bio-active molecules, such as peptides, proteins and DNAs, through the cell membrane into cells has opened up many promises in the field of medicine and drug delivery. Inorganic nanoparticles as new non-viral carriers have immense potential as drug and biomolecule carrier system. Risk of immune response, a common problem with viral vectors, [204] is manifold reduced with inorganic nanoparticle based carrier system. Most of the inorganic nanoparticles are non-toxic or mildly toxic to living cells. Inorganic nanoparticles are resistant to degradation in contact with bile salts and lipases in contrast to liposomes.[205] Above all, surface fictionalization in inorganic nanoparticle is relatively easy which attributes to their potential capability of targeted delivery and controlled release of carried drugs and biomolecules. Many inorganic materials, such as CaP,[206] silicon oxide,[207] gold,[208-211] carbon materials, [212, 213] iron oxide,[214,215] and LDH,[216] have been studied as a carrier for biomolecules. CaP nanoparticles found to be most promising among them primarily because of their excellent biocompatibility and biodegradability [217–219] in physiological environment. Most commonly used synthetic CaPs in orthopedic and dentistry are bioactive hydroxyapatite (HA, $Ca_{10}(PO_4)_6(OH)_2$) and bioresorbable tricalcium phosphate (TCP,$Ca_3(PO_4)_2$).

HA has long been recognized as having excellent affinity to biological substances, such as collagen, proteins, enzymes, cells, and viruses.[218, 219] HA scaffold impregnated with growth factors has been investigated for bone regeneration.[220 ,221] Ono et al. used HA granules with bone

morphogenetic protein (BMP) and revealed new bone formation around HA granules.[222] However, low efficiency of drug encapsulation due to limited surface area and lack of control over the drug release primarily because of very limited and unpredictable bioresorbability of HA implant have been the issues remained to be resolved. To address these problems, in past decade much research efforts have been directed towards the synthesis of HA micro-carriers or nano-carriers delivering antibiotics and growth factors with controlled release kinetics. Ijntema et al. employed HA microcrystals as microcarriers to load bovine serum albumin (BSA) of 5–10 wt.% and concluded that these can be used for a variety of biomedical purposes such as drug delivery, orthopedics and dentistry.[223] Liu et al. studied BSA loaded calcium deficient HA nanocarriers for controlled drug delivery.[224] The effect of powder crystallinity and surface area on loading and release of cytochrome-c from HA nanoparticles was investigated by Matsumoto et al.[225]

TCP being much more bioresorbable than HA offers significant opportunities to be used as a carrier for controlled release of drug and biomolecules. Cho et al found recombinant human bone morphogenetic protein-4 (rhBMP-4) loaded β-TCP particles with particle size between 50 to 500 μm did not exert any particle size effect on bone formation in rat calvarial defects.[226] Groot et al studied porous CaP ceramic, impregnated with 0, 1, 10 and 40 mg of bone morphogenetic protein (rhBMP-2), as an osteoinductive biomaterial in dorsal muscles of rabbits for five weeks.[227] Takaoka et al studied bone forming ability of porous β-TCP implants coated with PLA-DX-PEG polymer containing more than 0.0025% (w/w) of rhBMP-2 in the dorsal muscles of mouse.[228] Recombinant human transforming growth factor-b 1 (rhTGF-b 1) carrying capability of collagen-hydroxyapatite/ tricalcium phosphate (Col-HA/ TCP) microspheres was investigated by Hsu et al.[229] Active bone with mature marrow tissue formation was observed in the bone defect treated with Col-HA/TCP microspheres containing rhTGF-b1. Even though

within our scope, no literature was found to study the use of TCP nanocarriers as controlled release system. We want to investigate the possibility of using CaP nanoparticles as a controlled release carrier of growth factors for bone regeneration. Growth factors such as bone morphogenetic protein (BMP), basic fibroblast growth factor (bFGF), transforming growth factor b (TGF-b) are basic proteins, so bovine serum albumin (BSA) was selected as the model growth factor protein in this study.

5.1.1 Bovine Serum Albumin (BSA): Serum albumin is one of the most the most abundant protein in plasma with a typical concentration of 5g/100ml. It is chiefly responsible for the maintenance ofblood pH .[230] Albumins contain high amount of charged amino acids like aspartic and glutamic acids, lysine, and arginine, but low amount of tryptophan and methionine. It is also characterized with high content of cystine. The glycine and isoleucine content of BSA are lower than in the average protein.[231] **Table 5.1** shows the amino acid composition of BSA.

Table 5.1: Amino Acid composition of BSA[231, 232,234]

Ala 48	Cys 35	Asp 41	Glu 58
Phe 30	Gly 17	His 16	Ile 15
Lys 60	Leu 65	Met 5	Asn 14
Pro 28	Gln 21	Arg 26	Ser 32
Thr 34	Val 38	Trp 3	Tyr 21

The BSA molecule consists of three homologous domains (I, II, III). Each domain is divided into nine loops (L1-L9) by 17 disulphide bonds. Each domain in turn is the product of two subdomains (IA and IB). There are 17 disulphide bonds in each BSA molecule. Location of different disulphide bonds in BSA is shown in **figure 5.1**.

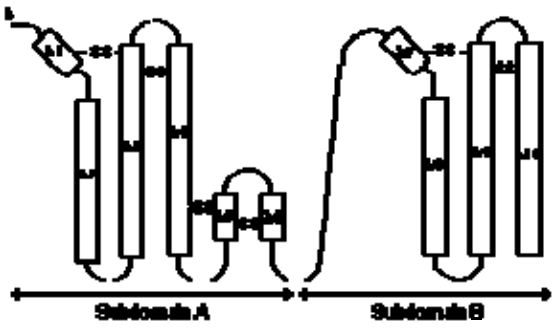

Figure 5.1: Location of disulphide bonds.[233]

The albumin molecule is not uniformly charged within the primary structure. At neutral pH, Peter et al. calculated a net charge of -10, -8, and 0 for domains I, II, and III for bovine serum albumin.[235] Serum albumin undergoes reversible conformational change with changes in pH as depicted in **figure 5.2**.

E <-------> F <-------> N <-------> B <-------> A

pH of transition:	**2.7**	**4.3**	**8**	**10**	
Name:	**Expanded**	**Fast**	**Normal**	**Basic**	**Aged**

Figure 5.2: Relationship of isomeric forms of bovine serum albumin with change in pH.[216]

The N-F transition involves the unfolding of domain III. At pH values lower than 4, albumin undergoes another expansion with a loss of the intra-domain helices. This expanded form is known as the (E) form. At pH 9, albumin changes conformation to the basic form (B). If solutions of albumin are maintained at pH 9 and low ionic strength at 3 °C for 3 to 4 days, another isomerization occurs which is known as the (A) form.[233, 234, 236]

5.1.2 Protein loading onto CaP nanoparticles by different technique

5.1.2 1 *Ex situ* process: Bovine serum albumin (BSA) is a protein with well defined primary structure and high content of charged amino acids. Thus depending on the zeta potential on nanoparticle surface there will be electrostatic attraction between BSA and CaP particles.

Gauckler et al. studied the influence of zeta potential on the amount of BSA adsorption on alumina, silica, titania, and zirconia nanoparticles and found that the extent of electrostatic interaction determined the amount of BSA adsorption on particle surface.[237] BSA can easily be adsorbed on CaP nanoparticle surface by electrostatic interaction, because of wide difference between the isoelectric points of CaP and BSA molecule.

Bioresorbability of CaP nanoparticle varies depending on its phase composition and crystallinity. CaP nanoparticles synthesized from aqueous precipitation route at a fixed Ca: P molar ratio of 1.5:1 showed different phase composition depending on the calcination temperature. Not only the phase composition, but particle size, surface area and crystallinity of CaP nanoparticles also changed with variation in calcination temperature. Since dissolution of CaP nanoparticles vary with change in particle size, surface area, crystallinity and phase composition, protein release from CaP nanoparticle surface can be controlled by controlling its physical and chemical properties.

Here we have synthesized nanocrystalline β-TCP and CDHA powders using reverse micelle based template system in microemulsion with surface area varying between 57 m^2/g and 73 m^2/g. The variation in BSA adsorption with change in particle size, surface area, phase composition, and pH of BSA- nanoparticle suspension was evaluated. The release behaviors of resulting BSA-loaded CaP nanoparticles were evaluated and correlated with the dissolution kinetics of CaP nanoparticles under the same experimental conditions.

5.1.2 2 *In situ* process: The protein loaded nanocarriers synthesized by *ex situ* process show a short term protein release because of lack of control over the protein release for longer period of

time. However, for a carrier system to be therapeutically effective, it should ensure prolong and steady protein release to function as a sustained protein delivery system. Liu et al. synthesized *in situ* BSA-loaded CDHA nanocarriers varying synthesis parameters and observed a continued steady protein release for 4 days from such system.[238] Boonsongrit et al studied protein release from BSA-loaded HAp microspheres encapsulated with poly(lactic acid-co-glycolic acid) (PLGA) and found that the BSA release could be made remarkably prolonged by PLGA encapsulation on HA.[239]

Though a number of literature reports are available on studying the effect of crystallinity, particle size, and surface area of HA micro and nanocarriers on protein loading and release from carrier system, the role of dopants in modifying protein release from HA nanocarriers has seldom been studied. Modification of crystallinity of HA nanocarrier by heat treatment is undesirable in many cases, as heating may lead to denaturation and inactivation of many biomolecules loaded on the nanocaarriers. Addition of dopant generates defects and disorder in HA crystal lattice and thus changes the crystallinity of HA nanocarriers without any application of heat. In this case we studied BSA- HA nanocarriers for the processing of a prolonged and steady protein delivery system and investigate the role of magnesium (Mg) and zinc (Zn) in controlling the protein release from HA nanocarriers. Mg and Zn are well known as two of the main cationic substitutes for calcium in the HA lattice.[240, 241] Biological apatites in enamel, dentin and bone contain trace amount of Mg and Zn.[241] Therefore, Mg and Zn-substituted HA nanoparticles are expected to have excellent biocompatibility and biological properties. Furthermore, the importance of Zn in medicine is well established because of its role in as many as 200 enzymes.[242] Incorporation of Mg and Zn in HA lattice results in decrease in crystallinity, and hence increase in extent of

dissolution.[243] Our hypothesis is that we can modify the rate of dissolution of HA nanocrystal by doping it with Zn and Mg and thus can control the protein release from doped and undoped HA nanocarriers.

Here we report synthesis of 2 mol % Mg and Zn doped BSA-HA nanopowders by *in situ* precipitation process. The cation doped and undoped BSA-HA nanopowders were characterized by X-ray diffraction (XRD), dynamic light scattering (DLS) technique, transmission electron microscopy (TEM), and Fourier transform infra-red (FTIR) spectroscopy. To understand the effect of dopants on the interaction between BSA and HA nanocrystal the nanopowders were studied using differential scanning calorimetry (DSC). The protein release behaviors of the BSA-loaded HA nanoparticles were studied in phosphate buffer solution at pH 7.2±0.2.

5. 2. Protein release from ex-situ synthesized CaP-BSA nanoparticles

5.2.1 Materials and Methods

5.2.1.1 Synthesis of TCP and CDHA nanoparticles

The synthesis of CaP nanoparticles with Ca: P molar ratio of 1.5:1 has already been discussed in Chapter 4. After calcination at different temperature from 600 to 800 °C phase pure CDHA and β-TCP nanoparticles were obtained. The CaP nanopowders were characterized by following techniques.

5.2.1.2 Physico-chemical properties of TCP and CDHA nanoparticles

The synthesized CaP nanoparticles calcined at 600,700 and 800 ^{o}C were characterized for phases, particle size, morphology and specific surface area as described in chapter 4 in section 4.2.4.

5.2.1.3 BSA loading on TCP and CDHA nanoparticles

Stock suspension of CaP nanoparticles (10 mg/ml) in water was prepared. Separately, a BSA (Sigma-Aldrich, St. Louis, MO) stock solution (5 mg/ml) in water was prepared and diluted in water to various concentrations of BSA (0.5, 1.5, 2.5, 3.5, 5 mg/ml). 1 ml of each of the above BSA solutions was mixed with 4 ml of nano particle suspension at pH 7.5 on a shaker for 6 h at 37 ^{o}C. Then samples were centrifuged at 8000 rpm, washed with water and the supernatants were analyzed for the BSA concentration using UV spectrophotometer at 570 nm on comparison to established standard curves. The amount of BSA adsorption per unit mass of CaP nanoparticles were then determined using the equation $(BSA)_{adsorbed} = ([BSA]_o-[BSA]_s) / W_{CaP}$, where $[BSA]_o$ represented total amount (μg) of BSA initially present in the suspension, $[BSA]_s$ represented total amount (μg)of BSA present in the supernatant, and W_{CaP} represented the total amount (mg) of CaP nanoparticles present in the suspension. After washing the BSA adsorbed CaP nanoparticles were dried at room temperature and stored at -10^{o} C in a freezer.

Background-corrected FTIR spectra of BSA loaded CaP nanopowders were analyzed in the amide I band regions for their component compositions and peak frequencies using Microcal origin 7.0 software. Gaussian curve-fitting, using GRAMS/ 386, was performed on the original (non-smoothed) amide I band region. The number of components and their peak positions were used as starting parameters. In all cases, linear baseline was fitted. The secondary structure content was calculated from the areas of the individual assigned bands and their fraction of the total area in the amide I region.[244] The determined areas were averaged, and standard deviations were calculated.

5.2.1.4 Study of release kinetics of BSA from TCP and CDHA nanoparticles

Twenty mg of BSA loaded CaP nanoparticles were suspended in 20 ml buffer solution in three separate vials containing phosphate buffer solution (PBS) at pH 7.2±0.2, bis-tris HCl buffer solution at 6.1±0.1 and acetate buffer solution at 4.1±0.1. Sample vials were incubated at 37 ^{o}C with continuous shaking. In this study, we selected pH 4.1 solution on the assumption that the local pH around the ruffled border of osteoclasts varies between 4.0 and 5.0 during the bone remodeling period.[245, 246] At early stage of inflammation the pH of blood remains around 5.0 to 6.0 which justifies the selection of pH 6.1, while PBS solution of pH 7.2 was chosen because of its resemblance to the pH of homeostatic body fluid. The vials were centrifuged and 0.5 ml of supernatants were removed at each time point, kept in cryovials and frozen at -10 ^{o}C. The sample vials were vortexed to resuspend the BSA-CaP nanoparticles, and placed back in the incubator. The released amount of BSA in the supernatant was measured by BCA protein assay at 0.5, 1, 2, 4, 6, 12 and 24 hours of time period. The rate of dissolution of CaP nanoparticles calcined at 600, 700 and 800 ^{o}C was evaluated by measuring Ca^{2+} ion concentration in buffer solution at different pH using atomic absorption spectrophotometer (AAS). Twenty milligrams of CaP nanopowders calcined at different temperature was suspended separately in 10ml of pH 4.0, 6.0 and 7.2 buffer solutions. The suspension was centrifuged at different time interval and the supernatant was analyzed for Ca^{2+} ion concentration by AAS. The blank solution was prepared by adding 90.0 ml double distilled deionized water to 10.0 ml 1% NaCl, 20% HNO_3. Samples were prepared by combining 2.0 ml of sample from dissolution media to 0.2 ml of 1% NaCl and 20% HNO_3. Samples were diluted with 0.1% NaCl and 2.0% HNO_3. The samples were measured at 422.7 nm using a Vapan FS 220 (Mulgrave, Victoria, Australia) AAS with a VWR (San Diego, CA, USA) calcium lamp with a slit of 0.5 and a current of 10 mA.

5.2.1.5 Statistical Analysis

Statistical analysis of data was performed using the same software package and following the same procedure as described in chapter 4 in section 4.2.4.6**.**

5. 2.2. Results

5.2.2.1 Physical properties of synthesized powders

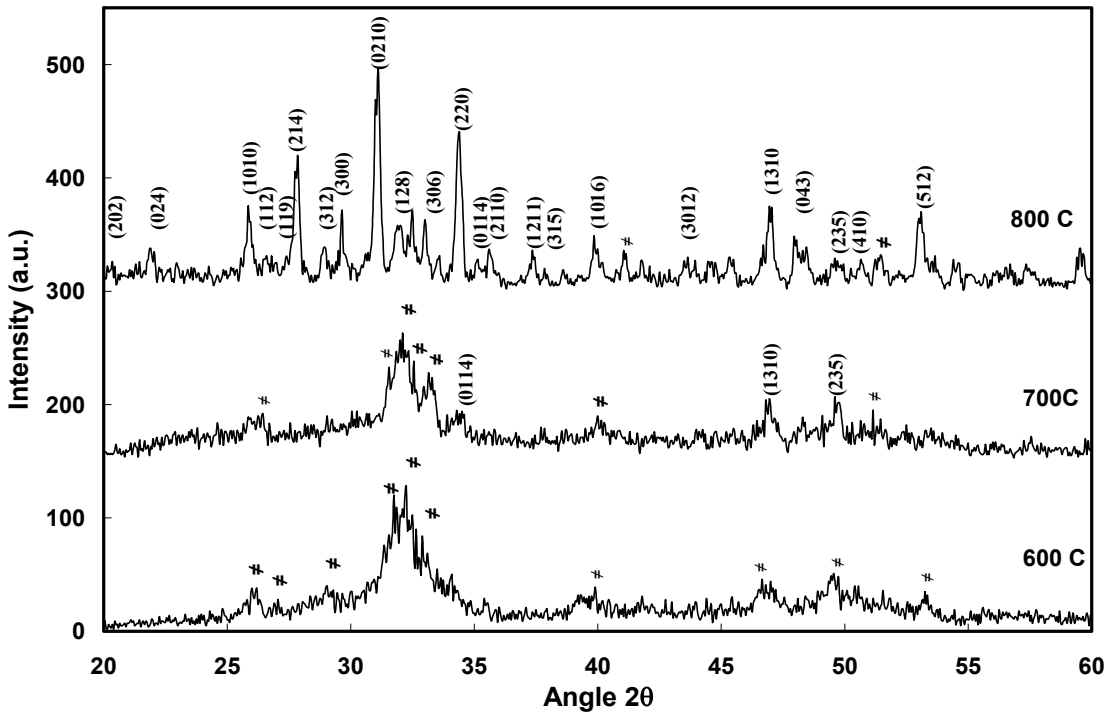

Fgure5.3: X-ray diffraction pattern of synthesized CaP nanopowders calcined at different temperature. ≠ indicates CDHA and ( ) indicates β-TCP.

Figure 5.3 shows XRD pattern of CaP nanopowders synthesized using NP-12 surfactant at a fixed aqueous to organic composition of 1:15 in the microemulsion and then calcined at 600,700 and 800 ^{o}C for 4 h. The nanopowders calcined at 600 and 700 ^{o}C consisted primarily of CDHA phase, but β-TCP was the major phase (JCPDS No 9-169) in CaP powder calcined at 800 ^{o}C which is consistent with the earlier reports.[175]

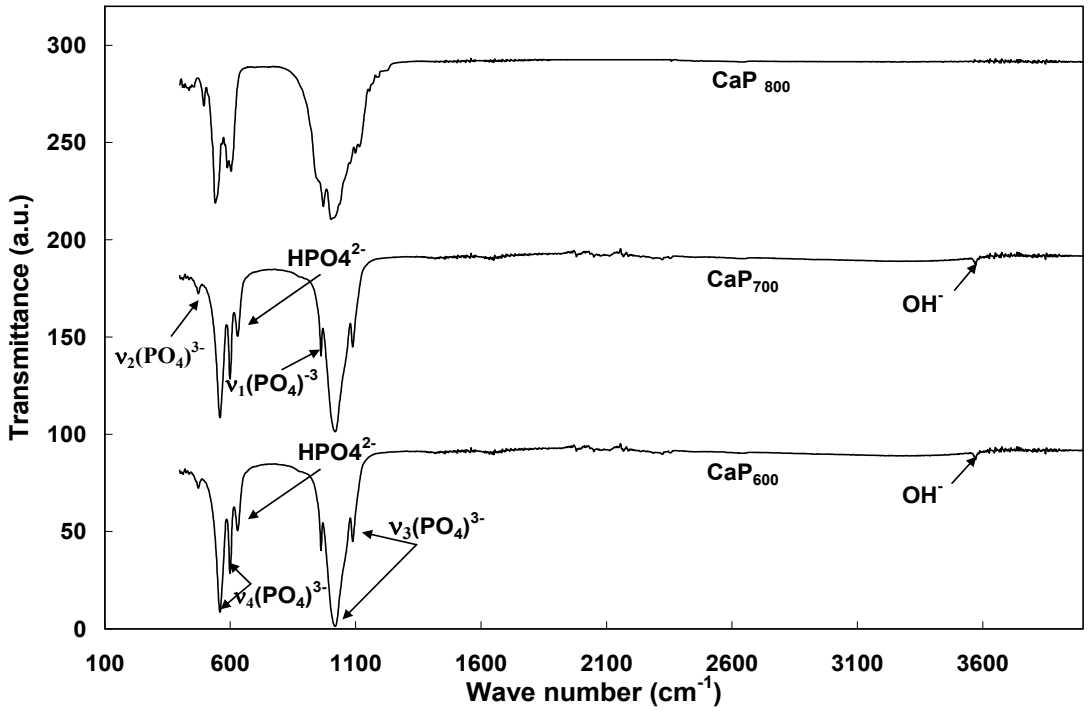

Figure 5.4: FTIR spectra of synthesized CaP nanopowders calcined at different temperature.

The change in phase composition of synthesized CaP nanopowders with increase in calcination temperature was also evident from the FTIR spectroscopy of the powders as shown in **figure** 5.4. Characteristic bands of phosphate group were detected at wave numbers 476, 563, 601, 985, 1025, and 1091 cm^{-1} for all the CaP nanopowders.[201, 202] The bands at 1025 and 1091 cm^{-1} were assigned to the components of triply degenerate ν_3 antisymmetric P–O stretching mode. The non degenerate P–O symmetric stretching mode ν_1 was detected at 985 cm^{-1}. The bands at 601 and 563 cm^{-1} were attributed to components of the triply degenerate ν_4 O–P–O bending mode and the doubly degenerate ν_2 O–P–O bending mode was evident at 476 cm^{-1}. [247] The most noticeable change in the FTIR spectra with increasing calcination temperature was the disappearance of HPO_4^{2-} band at 870 cm^{-1} and hydroxyl band at 3569 cm^{-1} which corresponded to the transformation observed by XRD. CaP nanopowders calcined at 800 ^oC showed a broader

band at 900–1200 cm^{-1} as compared to CaP nanopowders calcined at lower temperature, which is characteristic to β-TCP phase. The absence of ν_4 PO_4^{3-} band at 600 cm^{-1} confirmed the absence of α–TCP phase in the synthesized powders calcined at 800 ^oC.[248]

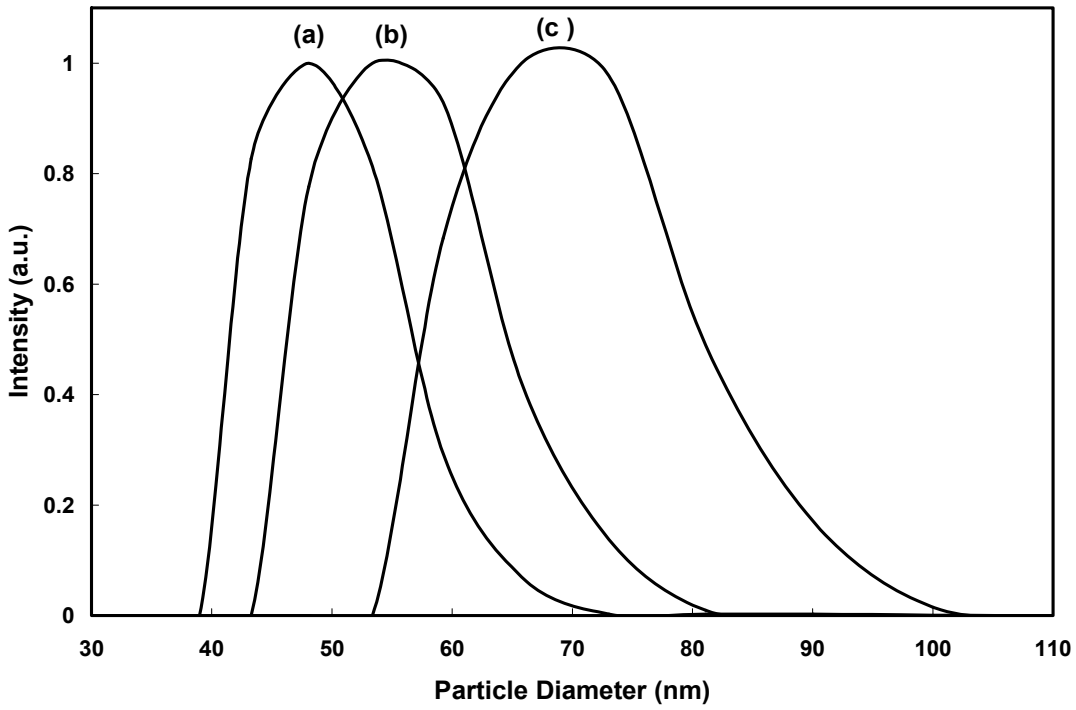

Figure 5.5: Particle size distribution of synthesized CaP nanopowders calcined at (a) 600, (b) 700 and (c) 800 ^oC.

The number average particle size (NICOMP) distribution data has been presented in **figure 5.5** which illustrates that the mean particle diameter increased from 48 nm to 69 nm as the calcination temperature increased from 600 ^oC to 800 ^oC. TEM micrographs of CaP nanopowders in **figure 5.6** revealed that with change in calcination temperature from 600 ^oC to 800 ^oC the aspect ratio of powder particles decreased. **Figure 5.7** showed an expected decrease in average BET surface area of CaP powders from 73 m^2/g to 57 m^2/g with increase in calcination temperature from 600 ^oC to 800 ^oC.

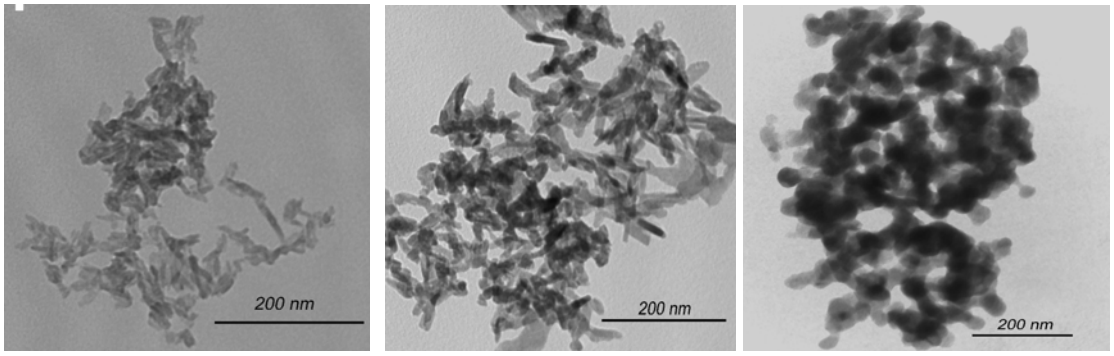

Figure5.6: TEM micrographs of CaP nanopowders calcined at different temperature (a) 600, (b) 700, and (c) 800 ^{o}C.

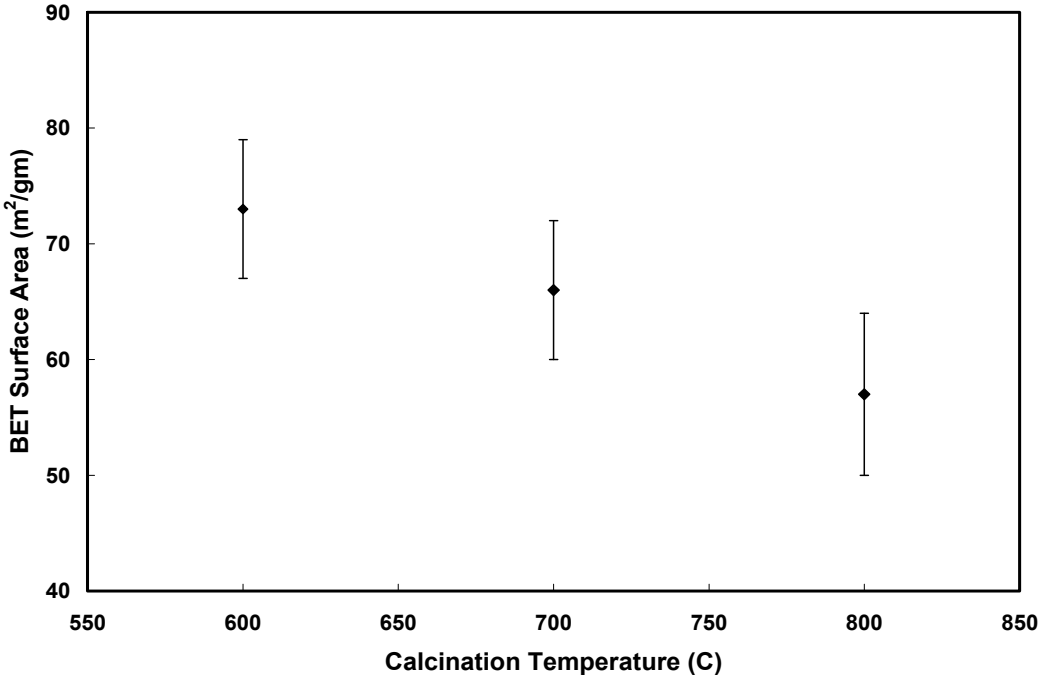

Figure 5.7: Variation in BET surface area as a function of calcination temperature

5.2.2.2. Protein adsorption on TCP and CDHA nanoparticles

Adsorption of protein on CaP nanoparticles was detected by FTIR analysis. The FTIR spectra of pure BSA and BSA loaded CaP nanopowders are also shown in **figure 5.8** for comparison. The spectrum of BSA exhibited an apparent absorption band at 1654 cm^{-1} assigned

to amide I, CMO stretching mode, 1540 cm^{-1} assigned to amide II, N–H bending mode and 1397 cm^{-1} assigned to amide III, C–N stretching mode and N–H bending mode.[224]

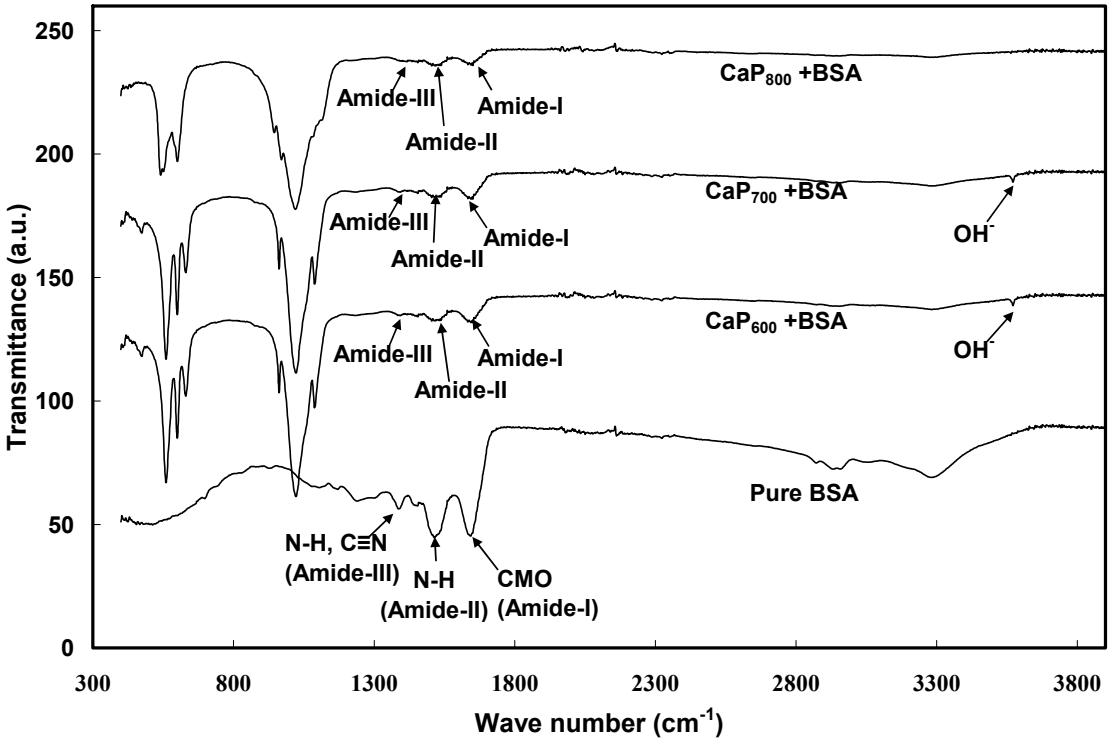

Figure 5.8: FTIR spectroscopy of pure BSA and BSA adsorbed CaP nanopowders.

The adsorbed amount of BSA on powder surface is significantly dependent on the pH of suspension where BSA-nanoparticle interaction took place. The adsorption of BSA onto 600 ^{o}C calcined CaP nanopowders was studied in suspensions at different pH of 7.5, 8.5, and 9. The maximum amount of BSA adsorption was observed at pH 7.5 and thereafter with increase in suspension pH the amount of BSA adsorption onto particle surface decreased as shown in **figure 5.9**. The adsorptive property of BSA on CaP nanopowders was also investigated with BSA solution at various concentrations. The result showed that the adsorbed amount of protein on CaP

nanopowders increased linearly in the range of 0–800 μg/ml of the protein solution and remained constant in solution with BSA concentration higher than 800 μg/ml. The adsorbed amount of

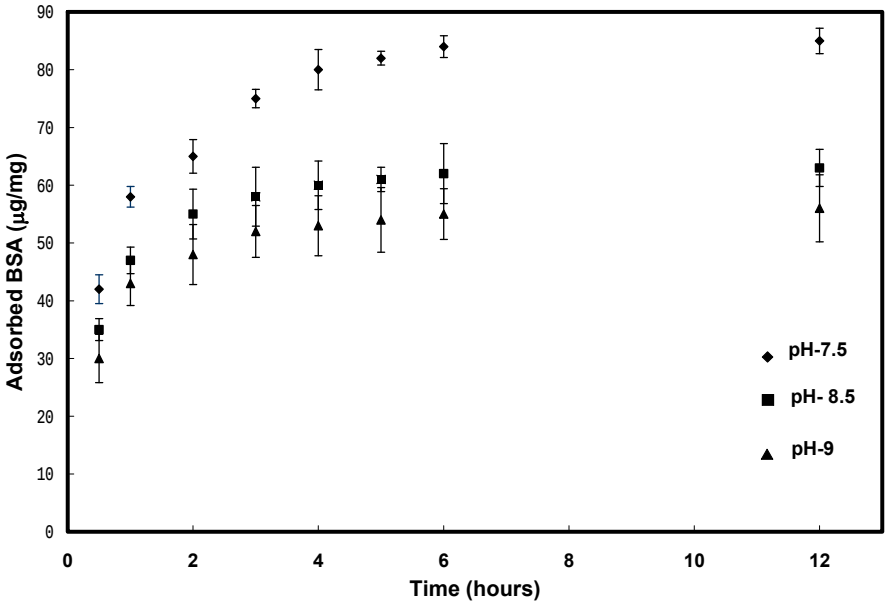

Figure 5.9: Loading of BSA onto CDHA nanoparticle surface at different pH

BSA on CaP nanopowders also changed depending on its average specific surface area as shown in **figure 5.10**. CaP nanopowders calcined at 600 ^{o}C with average specific surface area of 73 m^2/g showed the highest amount of BSA adsorption of 89 μg/mg, whereas 78 μg/mg of BSA was adsorbed onto 800 ^{o}C calcined CaP nanopowders having an average specific surface area of 57 m^2/g.

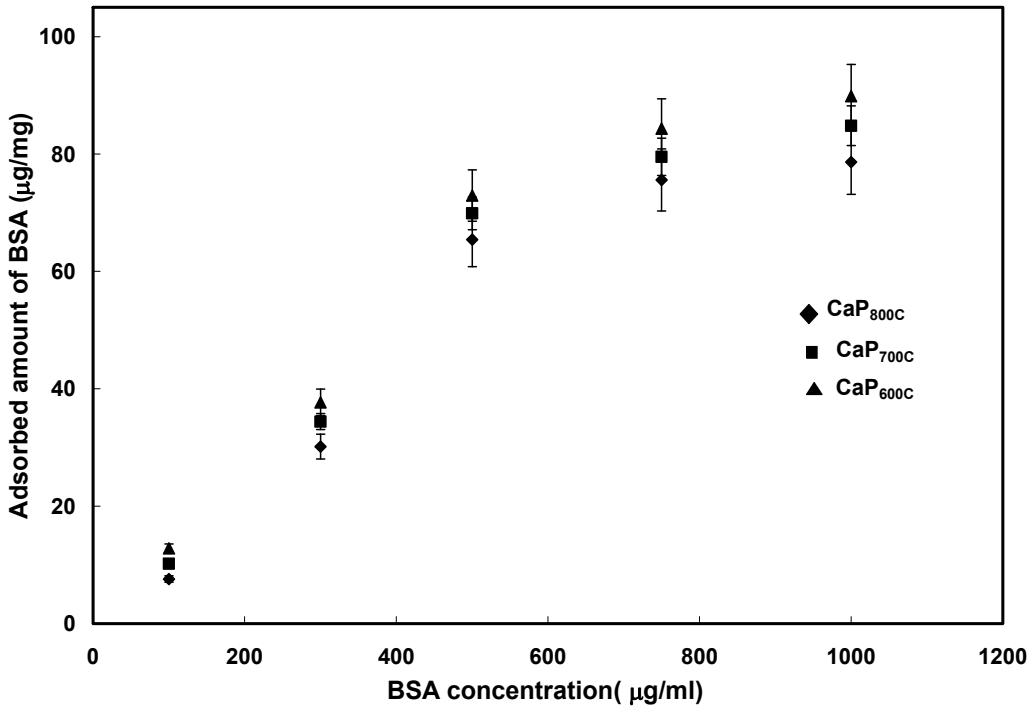

Figure 5.10: Loading of BSA onto CaP nanoparticles calcined at different temperature

5.2.2.3 Secondary structure analysis of BSA

The secondary structure of BSA adsorbed on CaP nanoparticle surface was analyzed using FTIR spectroscopy as shown in **figure 5.11**. **Table 5.2** shows the compositional analysis of secondary structure in pure solid BSA powder and adsorbed BSA on CaP nanoparticle surface. The α-helix content as determined from FTIR spectra in amide –I region was found to be 30 %, 31% and 34% for 600, 700 and 800 ^{o}C calcined CaP nanopowder respectively**.** The result showed a relative decrease in α –helix content in CaP- BSA nanopowder as compared to α- helix content of 38% in pure solid BSA powder.

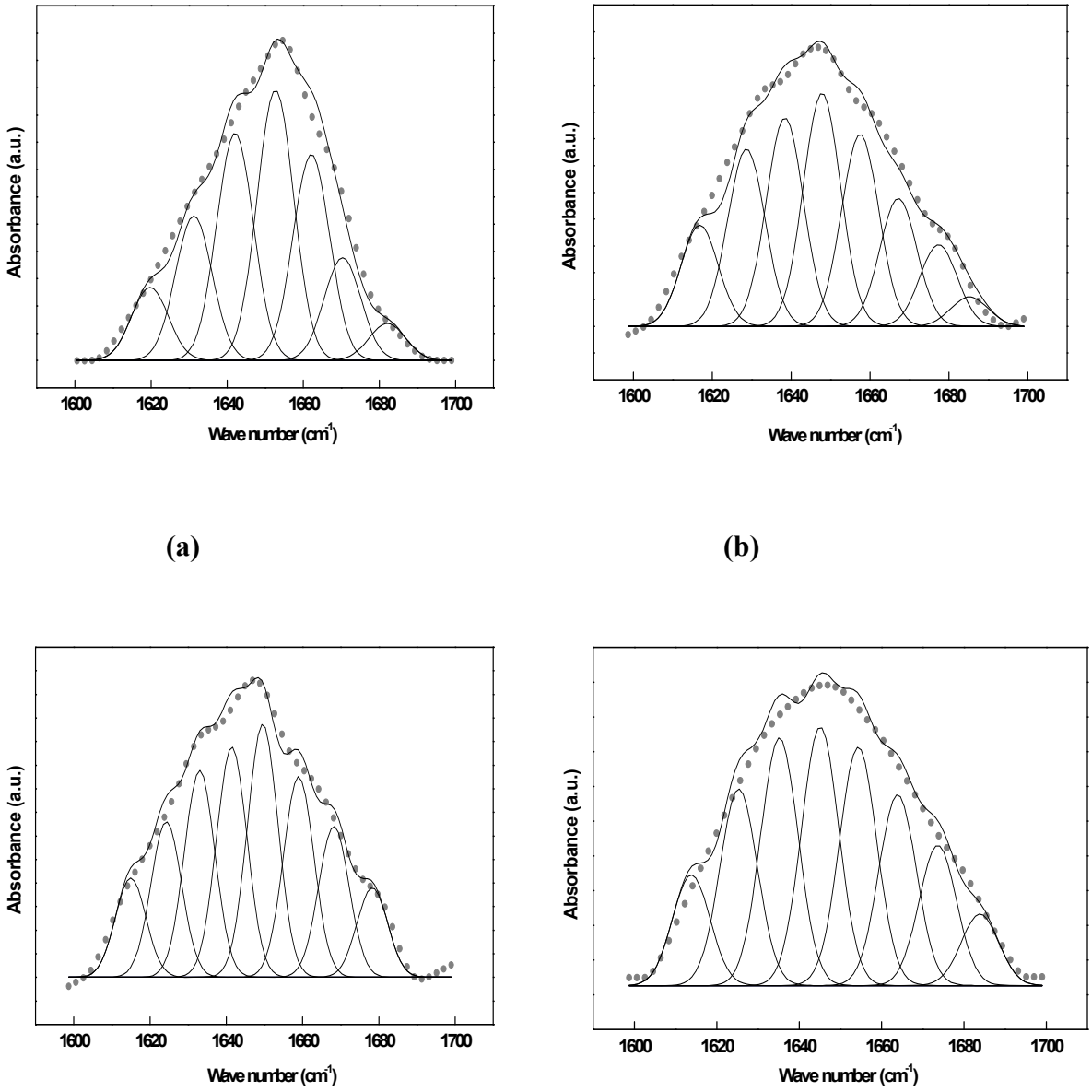

Fig.5.11: Infrared spectra of BSA in the amide I region and their Gaussian curve-fitting (the individual Gaussian bands are shown as symmetrical peaks underneath the IR spectra). Spectra are shown on a relative scale. (a) Pure BSA powder and BSA adsorbed on (b) CaP_{600C}, (c) CaP_{700C} , and (d) CaP_{800C} .

Table 5.2: Infrared band assignments of CaP nanoparticles [244, 249, 250]

Band position (cm^{-1})	Secondary structure assignment	Area				References
		Pure BSA	CaP_{600}+ BSA	CaP_{700}+ BSA	CaP_{800}+ BSA	
1616±3	unordered	5±1	8±2	7±1	4±1	**244**
1628±3	β-sheet	10±2	15±1	13±2	10±2	**249**
1638±3	β-sheet	16±2	19±2	16±1	16±2	**249**
1648±3	unordered	17±1	20±1	18±1	19±1	**250**
1658±3	α-helix	24±1	18±2	16±2	21±1	**250**
1665±3	Unordered	14±1	10±2	14±1	15±1	**244,250**
1671±3	Unordered	10±3	7±2	10±1	9±2	**249, 244**
1685±2	Unordered	4±2	3±2	6±1	6±1	**250**

5.2.2.4 Release rate of protein from BSA adsorbed TCP and CDHA nanoparticles.

The release rate of BSA from CaP nanoparticles was investigated by immersing BSA loaded CaP nanoparticles into buffer solutions at different pH.

5.2.2.4 1 Effect of buffer pH on protein release rate

Figure 5.12 a, b and c show the release rate of BSA from CaP nanoparticles immersed in pH 7.2, 6.1, and 4.1, respectively. For all CaP nanopowders, the amount of released BSA gradually increased with time. However, for BSA adsorbed nanopowders immersed in pH 7.2 solution, the amount of released protein was significantly smaller than that in pH 4.0 and pH 6.0 solutions as shown in **Figure 5.12**. Though the nanopowders immersed in pH 4 and pH 6

exhibited almost 100% release of BSA within 24 hours of incubation, not more than 45 % of protein release was observed for CaP nanopowders immersed in pH 7.2 buffer within the same period of incubation time.

5.2.2.4 2 Effect of calcination temperature on protein release rate

Irrespective of pH of the buffer in which BSA-CaP nanoparticles were immersed, nanoparticles calcined at 800 ^{o}C always showed significantly higher ($p < 0.0001$ in all cases) protein release compared to nanoparticles calcined at 600 and 700 ^{o}C. The BSA release from CaP nanoparticles calcined at 700 ^{o}C was also significantly higher in pH 7.2 ($p < 0.0001$) and pH 6.1 ($p= 0.0137$) buffer solution as compared to 600 ^{o}C calcined CaP nanoparticles, except in buffer solution of pH 4.1 ($p= 0.3842$).

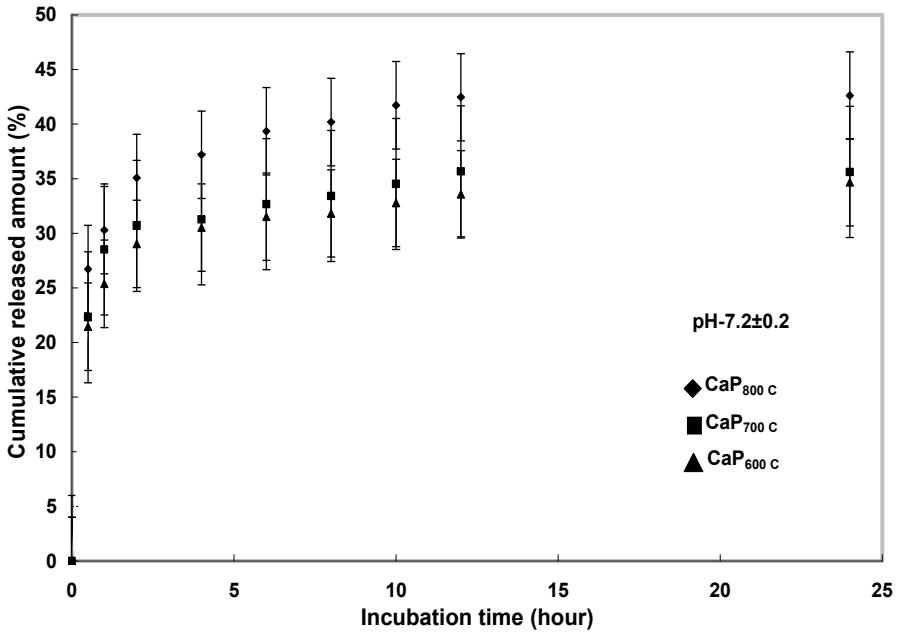

(a)

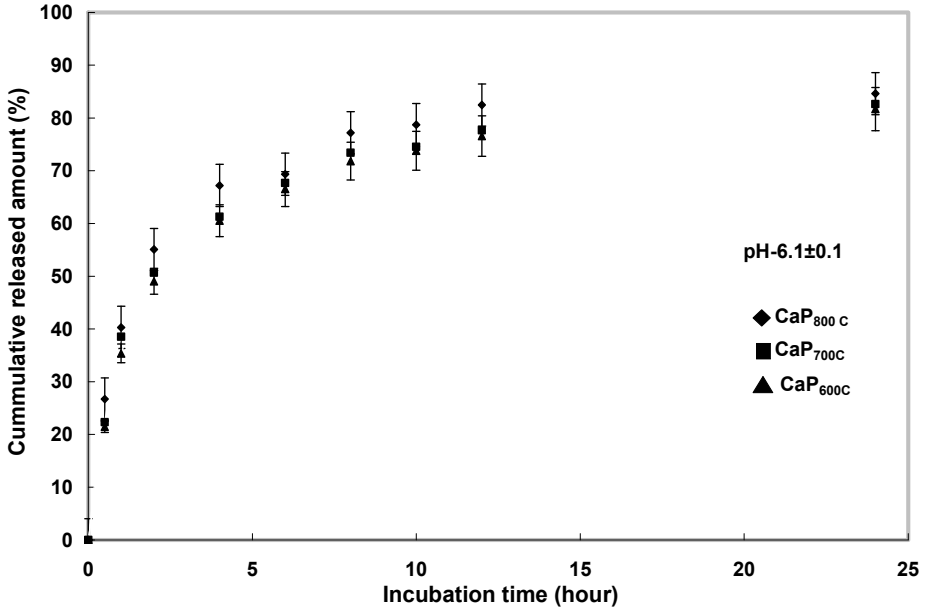

(b)

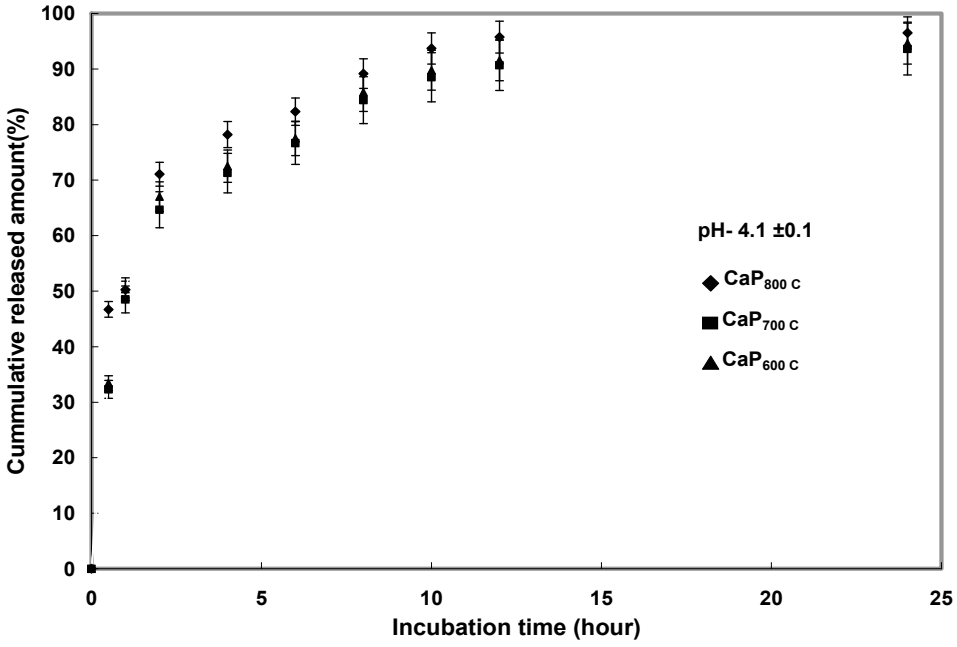

(c)

Figure 5.12: BSA release rate from CaP nanoparticles at different pH (a) 7.2, (b) 6.1, and (c) 4.1 Tukey's pairwise multiple comparison test. (a) at pH-7.2; p <0.0001 for CaP_{800} Vs CaP_{700} , p <0.0001 for CaP_{800} Vs CaP_{600} , p <0.0001 for CaP_{700} Vs CaP_{600}; (b) at pH-6.1; p <0.0001 for CaP_{800} Vs CaP_{700} , p <0.0001 for CaP_{800} Vs CaP_{600} , p =0.0137 for CaP_{700} Vs CaP_{600}; (c) at pH-4.1; p <0.0001 for CaP_{800} Vs CaP_{700} , p =0.0007 for CaP_{800} Vs CaP_{600} , p =0.3842 for CaP_{700} Vs CaP_{600};

5.2.2.5 Dissolution kinetic of TCP and CDHA nanoparticles

The rate of dissolution of CaP nanoparticles in different pH solution were evaluated by measuring Ca^{2+} ion concentration in supernatant using atomic absorption spectroscopy. CaP nanoparticles found to dissolve at increasingly faster rate with decrease in buffer pH from 7.2 to 4. Also at all pH, the rate of dissolution for 800 ^{o}C calcined CaP nanoparticles was always higher ($p < 0.0001$) compared to 600 and 700 ^{o}C calcined nanoparticles as evident from **Figure 5.13 a, b and c**.

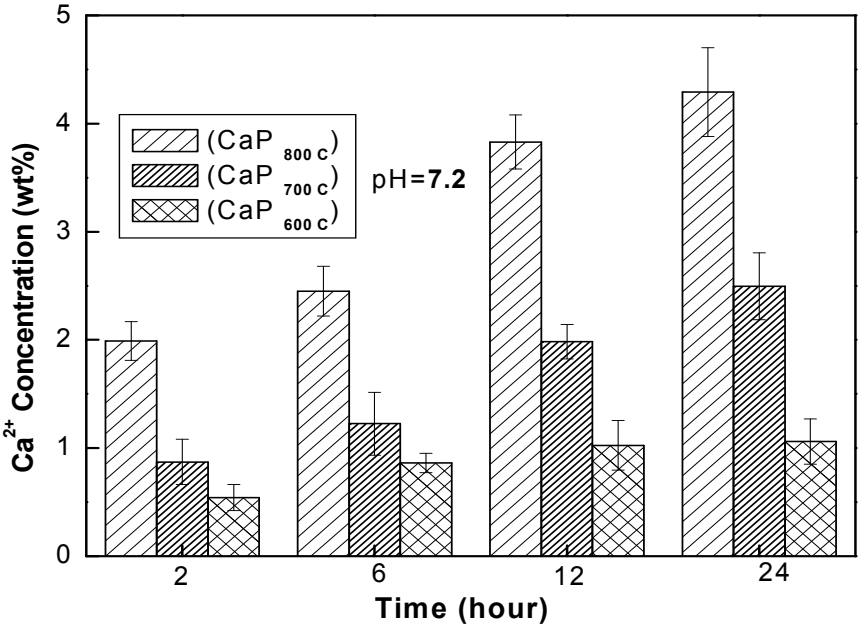

(a)

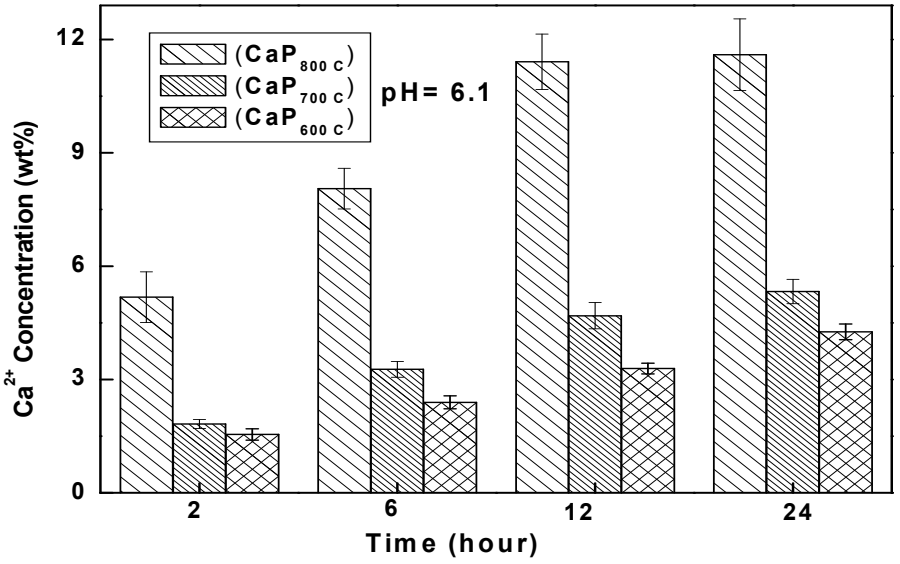

(b)

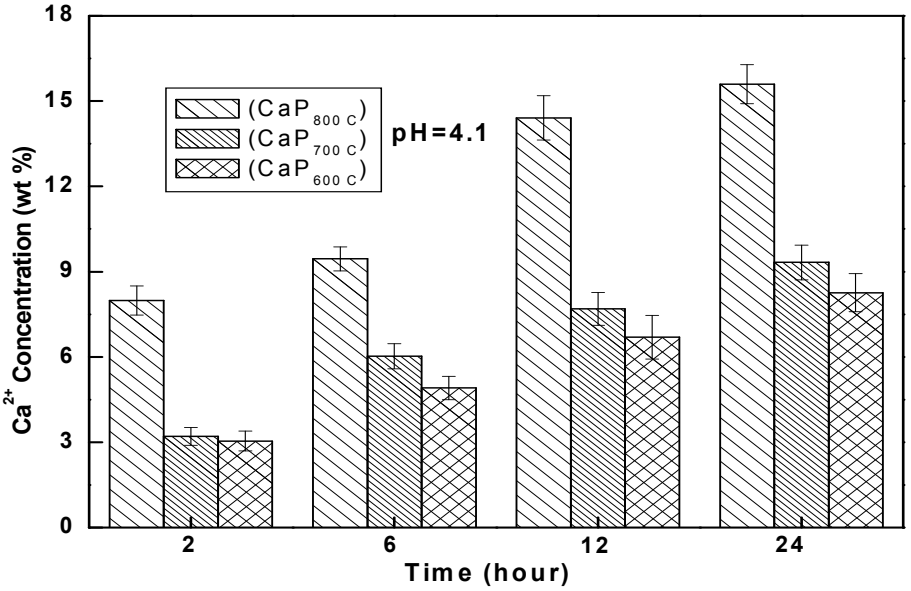

(c)

Figure 5.13: Dissolution kinetics of CaP nanoparticles at three different pHs (a) 7.2 (b) 6.1 and (c) 4.1. Tukey's pairwise multiple comparison test. (a) at pH-7.2; p <0.0001 for CaP_{800} Vs CaP_{700} , p <0.0001 for CaP_{800} Vs CaP_{600} , p <0.0001 for CaP_{700} Vs CaP_{600}; (b) at pH-6.1; p <0.0001 for CaP_{800} Vs CaP_{700} , p <0.0001 for CaP_{800} Vs CaP_{600} , p <0.0001 for CaP_{700} Vs CaP_{600}; (c) at pH-4.1; p <0.0001 for CaP_{800} Vs CaP_{700} , <0.0001 for CaP_{800} Vs CaP_{600} , <0.0001 for CaP_{700} Vs CaP_{600};

5.2.3. Discussion

NP12 surfactant stabilized the aqueous core in reverse micelle domain by organizing polar head groups away from non polar cyclohexane in a definite shape. The polar aqueous core contained Ca^{2+} and PO_4^{3-} ions with a Ca:P molar ratio equal to 1.5:1. Addition of NH_4OH in the microemulsion increased OH^- concentration and promoted nucleation of CDHA[$Ca_9(HPO_4)(PO_4)_5(OH)$] crystal inside polar core of reverse micelle which gradually grew on aging and finally precipitated out in the reaction mixture. The chemical reaction that occurred inside the nanodroplets of water was as follows.

$$9\ Ca(NO_3)_2 + 6\ H_3PO_4 + 18\ NH_4OH = Ca_9(HPO_4)(PO_4)_5(OH) \downarrow + 18\ NH_4NO_3 + 17\ H_2O \quad (1)$$

This CDHA phase transformed into β-TCP on heating at and above 800 ^oC according to following equation.

$$Ca_9(HPO_4)(PO_4)_5(OH) \rightarrow 3\ Ca_3(PO_4)_2 + H_2O \quad (2)$$

In this study, the synthesized CaP nanoparticles showed different crystalline phase with change in calcination temperature which is consistent with previous reports.[235, 236] With increase in calcination temperature the particle size of CaP nanopowders increased due to the growth of CaP nanocrysal. The decrease in particle aspect ratio with similar increase in calcination temperature is attributed to the phase transformation of CDHA into β-TCP with loss of one molecule of water along c-axis of CDHA nanocrystal. CaP nanopowder calcined at 600 ^oC showed the highest average BET surface area not only because of its smaller particle size, but also due to higher particle aspect ratio.

The interaction between BSA and CaP nanoparticle was a dynamic process of adsorption and desorption which reached equilibrium within 6 h. Here we studied BSA loading on CaP nanoparticles at pH $\geq$ 7.5, because at lower pH the dissolution of CaP nanoparticles could

destroy a stable interface between BSA-CaP nanoparticles. Since pH of BSA- CaP suspension was above the isoelectric points of each of BSA, β-TCP and CDHA, both BSA and CaP nanoparticles carried negative charges on their surface. The stern layer of hydroxyl ions attached to exposed Ca^{2+} ions was the source of negative charge on CaP nanoparticle surface. This was followed by a diffuse electrical double layer around the surface of CaP nanoparticles. BSA interacted with CaP nanoparticles through electrostatic interaction between COO^- and Ca^{2+}. For successful BSA adsorption on CaP nanoparticle surface the energy released due to Ca^{2+} -COO^- interaction should supersede the sum of energy released for Ca^{2+}- OH^- attractive interaction and repulsion between BSA chain and electrical double layer around CaP particle surface. The electrostatic interaction between Ca^{2+} and COO^- was energetically favorable when BSA chain length was greater than the thickness of electrical double layer around the particle surface. As pH of the suspension increased from 7.5 to 8.5 to 9 an enhanced charge density on particle surface made Ca^{2+}-OH^- interaction increasingly stronger with a consequent gradual increase in electrical double layer thickness around the CaP nanoparticle surface. This coupled with the shortening of BSA chain length with similar increase in pH rendered BSA-nanoparticle interactions increasingly unfavorable resulting in a decrease in the amount of BSA adsorption onto nanoparticle surface. As expected, the adsorbed amount of BSA increased with increase in surface area of CaP nanoparticles immersed in BSA solutions. Higher the surface area higher was the surface charge density of CaP nanopowders, resulted in a higher degree of electrostatic interaction between BSA and CaP nanoparticles.

In general α-helix content is a preferred indicator of protein's structural integrity. β-sheet content in protein may alter due to protein–protein interactions leading to the formation of intermolecular β-sheet. Consequently, the β-sheet content of a protein in solid form does not

reflect its actual intramolecular structural content. The decrease in α-helix content in CaP- BSA nanopowders indicates that BSA's secondary structural integrity was somehow distorted on its adsorption to CaP nanoparticle surface. The distortion in secondary structure in BSA is attributed to unidirectional electrostatic interaction between Ca^{2+} and COO^{-} .

The first layer of BSA was adsorbed onto nanoparticle surface purely by virtue of electrostatic interaction between CaP nanoparticles and BSA. The adsorption of subsequent layers of BSA was mainly governed by intermolecular hydrophobic interactions as BSA molecules experienced gradually lesser extent of electrostatic interaction with increasing thickness of BSA layers on nanoparticle surface. That is why a number of the BSA layers were adsorbed on CaP nanoparticle surface which were not tightly bound. The initial burst release of protein from nanoparticle surface was mainly due to desorption of these loosely bound BSA molecules. At physiological pH, the solubility product of β-TCP ($K_{sp} \approx 2.27 \times 10^{-27}$) is much higher compared to that of CDHA ($K_{sp} \approx 2.35 \times 10^{-49}$). This explains why 800 ^{o}C calcined CaP nanopowders showed higher rate of dissolution than CaP nanopowders calcined at 600 and 700 ^{o}C at all pHs studied here. The similar trend in BSA release rate with CaP nanoparticle dissolution rate revealed the fact that later stage of BSA release was mainly controlled by particle dissolution to release tightly bound BSA molecules. The higher BSA release from 700 ^{o}C calcined CaP nanopowders as compared to 600 ^{o}C calcined CaP nanopowders is attributed to the presence of little amount of β-TCP phase in the former. The dissolution of CDHA and β-TCP nanoparticle can be explained by following equations.

$$Ca_9(HPO_4)(PO_4)_5(OH) + 19H^{+} \leftrightarrow 9Ca^{2+} + 9H_2PO_4^{-} + H_2O \quad \text{.....(3)}$$

$$Ca_3(PO_4)_2 + 4H^{+} \leftrightarrow 3\,Ca^{2+} + 2H_2PO_4^{-} \quad \text{.....(4)}$$

As the pH of buffer solution decreased, the H^+ concentration in buffer solution increased. The increase in H^+ concentration forced the dissolution equilibrium to be shifted towards right, making dissolution of CaP nanoparticles faster. At lower pH, CaP nanoparticle dissolution being much faster than that at physiological pH, the BSA release rate was also faster.

5.3 Protein release from *in situ* synthesized Mg and Zn doped HA-BSA nanoparticles

5.3.1. Materials and Methods

5.3.1.1 Materials: For synthesis of BSA loaded HA nanopowders, calcium nitrate [$Ca(NO_3)_2$, $4H_2O$] and ammonium hydrogen phosphate [$(NH_4)_2HPO_4$, Alfa Aesar, Ward Hill, MA] were used as source of Ca^{2+} ion and PO_4^{3-} ion and BSA (Sigma-Aldrich, St. Louis, MO) was used as a model protein. Mg^{2+} and Zn^{2+} doped BSA-HA nanopowder was synthesized using magnesium nitrate [$Mg(NO_3)_2$, $6H_2O$, J. T. Baker, Phillipsburg, NJ] and [$Zn(NO_3)_2$, $10H_2O$, J. T. Baker, Phillipsburg, NJ] as a source of Mg^{2+} and Zn^{2+} respectively. Ammonium hydroxide (NH_4OH, J. T. baker, Phillipsburg, NJ) was used to adjust the pH of the reaction mixture.

5.3.1.2 Synthesis of HA-BSA nanopowders: 5 M aqueous solution of Ca^{2+}-ion was prepared by dissolving 0.03 moles of $Ca(NO_3)_2$, $4H_2O$ in 6 ml distilled water. A BSA aqueous solution of 1500 μg/ml was separately prepared by dissolving BSA powder into distilled water. NH_4OH was added dropwise to adjust the pH of Ca^{2+} solution to 9. Five ml of BSA was dropped into Ca^{2+} solution with constant stirring. To maintain Ca to P molar ratio of 1.67:1 in the reaction mixture, 0.018 moles of $(NH_4)_2HPO_4$ was added to Ca^{2+}- BSA solution. The pH of the reaction mixture was readjusted to 9 by dropwise addition of NH_4OH. The suspension was centrifuged to drain supernatant out and the resulting precipitate was then washed with phosphate-buffered solution (PBS at pH 7.0) and DI water for 3 times to remove NO_3^- ions and loosely bound BSA. 2 mol% Mg^{2+} and Zn^{2+} doped HA-BSA nanopowders were synthesized by addition of required amount of

$Mg(NO_3)_3$, $6H_2O$ and $Zn(NO_3)_3$, $6H_2O$ respectively in the Ca^{2+} aqueous solution. After washing all the powders were dried at room temperature and stored in a freezer at -10^o C.

All the supernatants after every washing were collected and analyzed for concentration of BSA in it using BCA protein assay kit. The total amount of BSA incorporated into doped and undoped HA nanopowders was calculated by using the equation $\frac{[BSA]_I - [BSA]_S}{[BSA]_I}$ X 100 %, where $[BSA]_I$ = total amount of BSA added to the reaction mixture, $[BSA]_S$ = total amount of BSA present in the supernatant.

5.3.1.3 Phase, crystallinity, particle size and partcle morphology of synthesized HA-BSA nanopowders: HA-BSA nanopowders were used for powder x-ray diffraction (XRD) following the same procedure as described in chapter 4 (section 4.2.4). The crystallinity of the apatite crystallites was evaluated by measuring the broadening of the XRD peaks in two regions: peak (002) between 25.0 and 27.0° and peak (310) between 37.5 and 41.0°.[251] Broadening of the diffraction peaks was measured at half maximum intensity of the peaks using the Scherrer formula,[252] $D = k\lambda/\beta_{1/2} \cos\theta$ as illustrated in chapter 4 (section 4.2.4.1). Particle size and morphology of synthesized doped and undoped HA-BSA nanoparticles were measured using DLS technique and TEM following the same procedure as described in chapter 4 in section 4.2.4.

5.3.1.4 Transmission electron microscopy: A very dilute aqueous suspension of doped and undoped HA-BSA nanoparticles in water was prepared following aforementioned method. One drop, approximately 5 μl, of particle suspension was deposited onto a formvar coated Cu grid (Ted Pella, Inc.) and allowed to equilibrate for 3 min. The grids were then allowed to air dry. Images were taken using a JEOL, JEM 120 (MA, USA) transmission electron microscope (TEM) set to an accelerating voltage of 100 kV.

5.3.1.5 Elemental analysis of HA-BSA nanopowders: The elemental composition of undoped and doped HA-BSA nanopowders were determined with inductively coupled plasma-optical emission spectroscopy (ICP-OES) using Optima 3200 RL (Perkin Elmer, CA, USA) instrument. For this analysis, ~ 0.1 g of doped and undoped HA-BSA nanopowders were calcined in a muffle furnace at 600 ^{o}C for 2 h to burn out BSA in it. The calcined powders were then dissolved in 10 % HNO_3. All the standards and also the samples were diluted with 4 % HNO_3 for final measurements.

5.3.1.6 Differential Scanning Calorimetric (DSC) analysis. To understand the interaction between HA and BSA, both doped and undoped nanopowders were tested on a DSC thermal analyzer (NETZSCH, Burlington, MA, USA). The measurements were performed with a differential scanning calorimeter model STA 409 PC at a heating rate of 10 K/min in argon atmosphere with a flow rate of 40 ml/min. Samples were kept in an alumina crucible for analysis with an empty crucible as reference. Pure HA nanopowder was used for baseline correction.

5.3.1.7 ATR-FTIR analysis of HA-BSA nanopowders: Fourier transform infrared spectroscopy (FTIR) was conducted on BSA loaded doped and undoped HA nanoparticles to analyze different absorption peaks of BSA and HA. Also the secondary structure of BSA was analyzed following the same procedure as defined in previous section **5.2.1.3.**

5.3.1.8 Study of release kinetics of BSA from HA-BSA Nanopowders: 20 ml of phosphate buffer solution at pH 7.2 was added to BSA-loaded doped and undoped HA nanoparticles. The nanoparticles were dispersed with a stirring rate of 100 rpm at 37 ^{o}C. The sample vials were centrifuged and 0.5 ml of supernatants were removed at each time point, kept in cryovials and frozen at -10 ^{o}C. The BSA release test was carried out by taking 0.1 ml of the supernatant and and mixing this with 0.1 ml of bicinchoninic acid solution (Sigma, bicinchoninic acid protein

assay kit, BCA-1 and B9643). UV–visible spectroscopy (Agelent 8453) was used for the characterization of absorbance peaks at 562 nm to determine the BSA concentration through the use of a pre-determined standard concentration–intensity calibration curve.

5.3.1.9 Statistical Analysis: Statistical analysis of data was performed using the same software package and following the same procedure as described in chapter 4 in section **4.2.4.6.**

5.3.2 Results

Figure.5.14 shows the x-ray diffraction (XRD) patterns of BSA-loaded doped and undoped HA nano-powders. All the powders showed pure HA according to ICDD No. 09-0432.[253] As evident from **table 5.3**, the peaks for (002) and (310) reflections were broader for doped HA-BSA nanopowders. Zn doped HA –BSA nanopowder showed the highest broadening of above peaks among the three powders. The relative broadening of (002) and (310) diffraction lines indicated that crystallinity was the lowest for Zn doped nanopowders, whereas the undoped HA-BSA nanopowders showed the highest crystallinity.

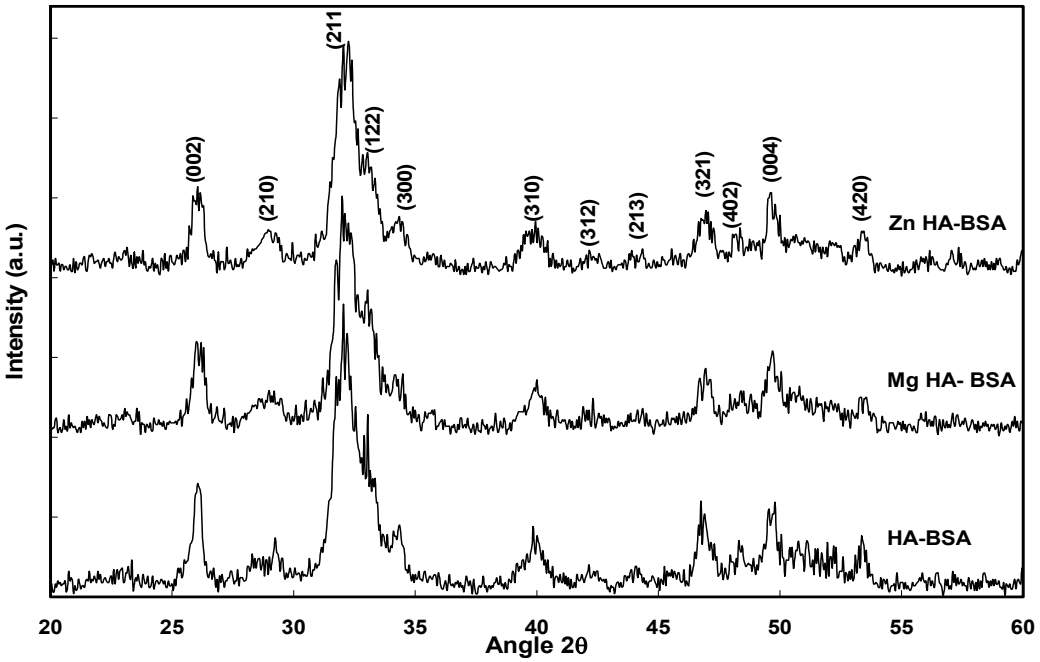

Figure 5.14: X-ray diffraction pattern of doped and undoped HA- BSA nanopowders

Table 5.3: Peak width measurements of the (002) and (310) reflections of BSA loaded doped and undoped HA nanopowders

Sample	Peak width (2θ)	
	(002)	(310)
HA-BSA	0.456	0.608
MgHA-BSA	0.476	0.656
ZnHA-BSA	0.512	0.752

Figure 5.15 shows the FT-IR spectra of the BSA-loaded doped and undoped HA nanopowders. All the nanopowders showed typical ν_3 asymmetric PO_4^{3-} stretching mode at 1093 cm^{-1} and 1024 cm^{-1}, ν_1 symmetric PO_4^{3-} stretching mode at 974 cm^{-1}, labile PO_4^{3-} at 634 cm^{-1}, triply degenerate ν_4 PO_4^{3-} bending mode at 601 and 561 cm^{-1}, and doubly degenerate ν_2 bending mode at 478 cm^{-1}.[201, 202, 254] The decreases in the relative peak intensities at 561, 601, and 1024 cm^{-1} for Mg and Zn doped HA-BSA nanopowders as compared to undoped HA-BSA nanopowders also reflected a relative decrease in crystallinity with addition of dopants into HA-BSA nanocrystal. The doubly degenerate ν_2 CO_3^{2-} bending mode at 871 cm^{-1} indicated the formation of the β-type carbonate in these HA nanopowders.[201] The presence of BSA in all the powders were confirmed from band at 1655 cm^{-1} assigned to amide I C=O stretching mode, 1542 cm^{-1} assigned to amide II N–H bending mode, 1475 cm^{-1} assigned to amide III C–N stretching mode, and 1475 cm^{-1} assigned to amide III N–H bending mode.[224]

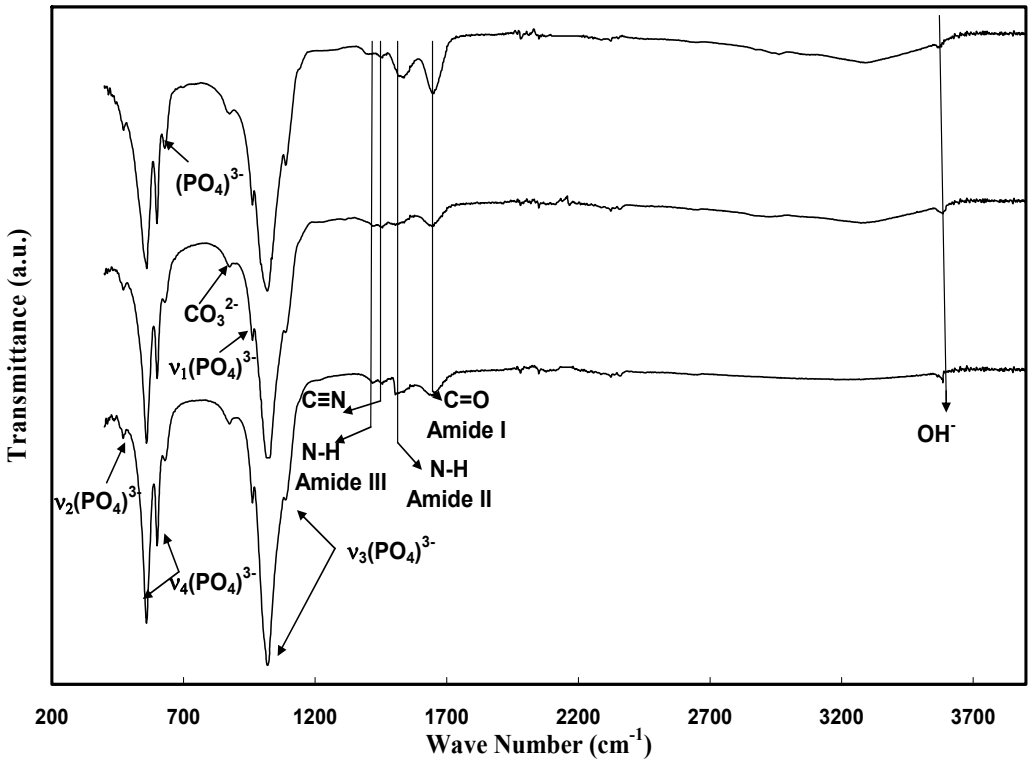

Figure 5.15: FTIR spectra of doped and undoped HA-BSA nanopowders.

Form number average particle size (NICOMP) distribution data presented in **figure 5.16** it is evident that doped HA nanopowders showed broader particle size distribution as compared to undoped HA nanopowder. The number average particle size of these nanopowders varied between 30 -110 nm. TEM micrographs of nanopowders in **figure 5.17** revealed that aspect ratio of doped nanoparticles were higher compared to undoped nanoparticles. Zn doped HA-BSA nanopowder showed the highest aspect ratio among the three powders.

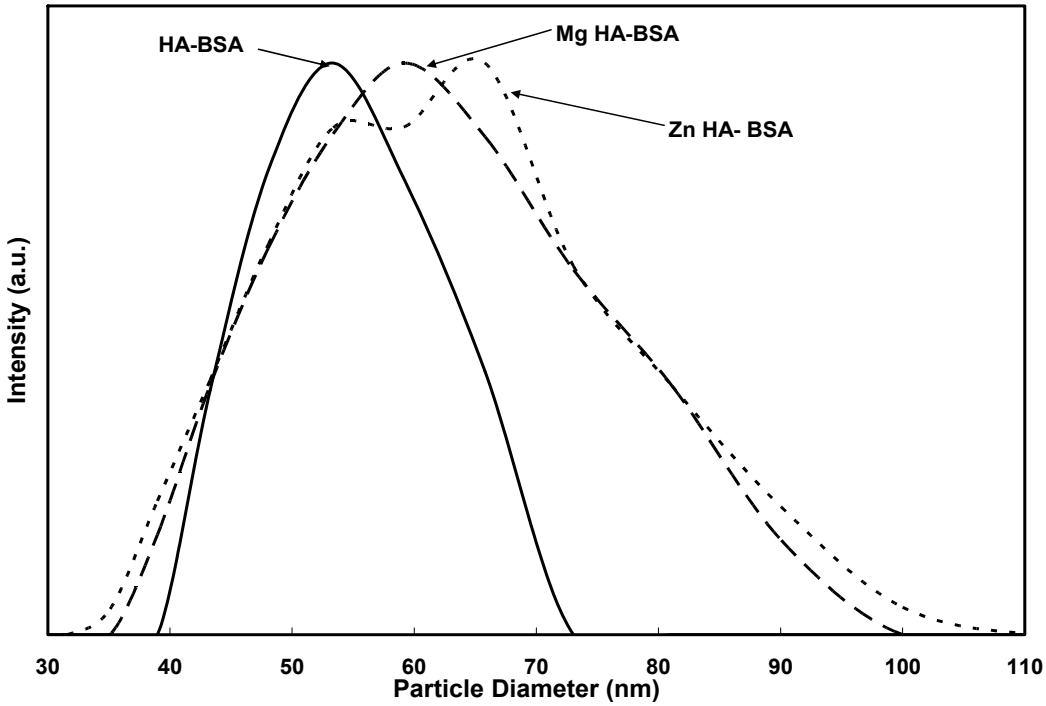

Figure 5.16: Particle size distribution of synthesized HA-BSA nanopowders.

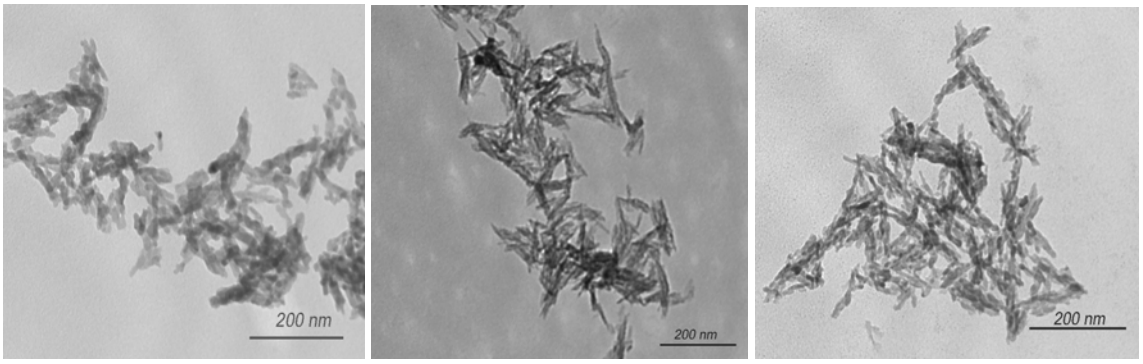

(a) (b) (c)

Figure 5.17: TEM micrographs of in-situ synthesized HA-BSA nanopowders. (a) undoped (b) Mg doepd and (c) Zn doped.

Quantitative estimates of weight and atomic percents of different element present in doped and undoped HA nanopowders are shown in **table 5.4**. The variation in measured dopant atomic percentages suggests that not all of the dopants added precipitated out as a part of the HA. Zn^{2+} appeared to be more effective compared to Mg^{2+} in substituting Ca^{2+} in HA nanopowders. For all the powders Ca/P ratio found to be higher than ideal Ca/P ratio of 1.67 for HA.

Table 5.4: Concentration of Ca, P, Mg and Zn in HA- BSA, Mg HA- BSA and Zn HA-BSA nanopowders, as determined by ICP-OES

	Undoped HA-BSA	Mg doped HA-BSA	Zn doped HA-BSA
Ca (wt %)	38.23±1.54	37.48 ±1.61	37.27± 1.54
P (wt %)	16.41±0.89	16.61±0.34	16.78 ±0.45
Mg (at %)	----------	0.143 ±0.08	----------
Zn (at %)	----------	----------	0.178 ±0.12
Ca/P (atomic)	1.81 ±0.02	1.75 ±0.39	1.72 ± 0.024

The interaction between BSA and HA was explored by differential scanning calorimetric (DSC) analysis as shown in **figure 5.18**. The endothermic peak at 70 ^{o}C was attributed to thermal denaturation of BSA. The removal of water molecule from BSA was evident from the exothermic peak at 210 ^{o}C. Thermal decomposition of BSA molecule was detected by the exothermic peak at 350 ^{o}C.[224] The most noticeable difference in DSC plot of undoped HA-BSA nanopowders from that of doped HA- BSA nanopowders was a sharp and intense exothermic peak in former as compared to relatively broad and less intense exothermic peak in the later at around 470 ^{o}C. The concerned exothermic peak was probably attributed to the thermal decomposition of the BSA–HA complex.[224]

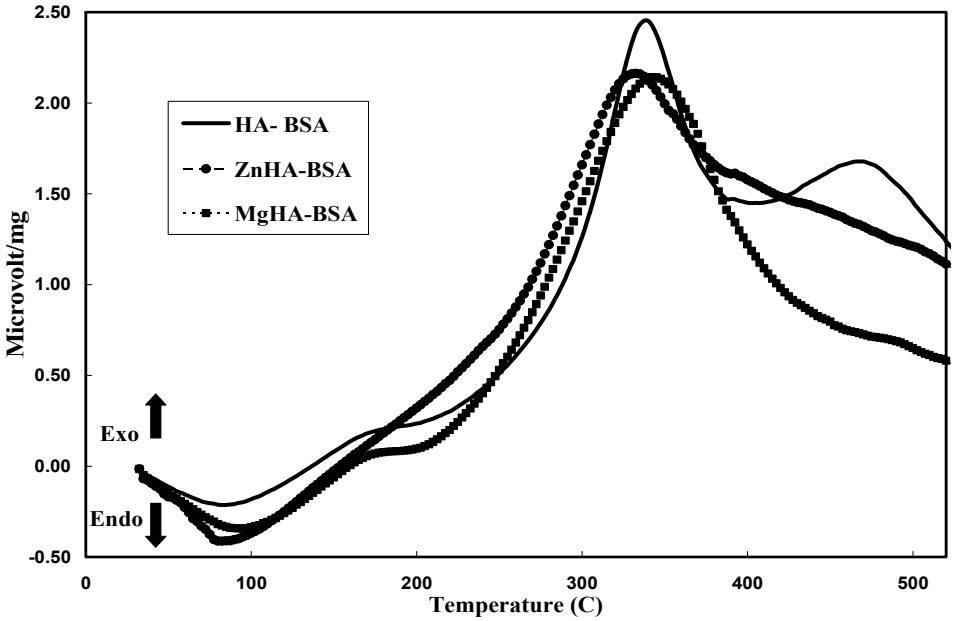

Figure 5.18: DSC curves of BSA loaded undoped and doped HA nanopowders

The amount of BSA uptake by doped and undoped HA nanoparticles is presented in **figure 5.19**. Zn doped HA nanopowder showed the maximum amount (24 wt %) of BSA uptake, followed by Mg doped (21 wt %) and undoped (18 wt %) HA nanopowders.

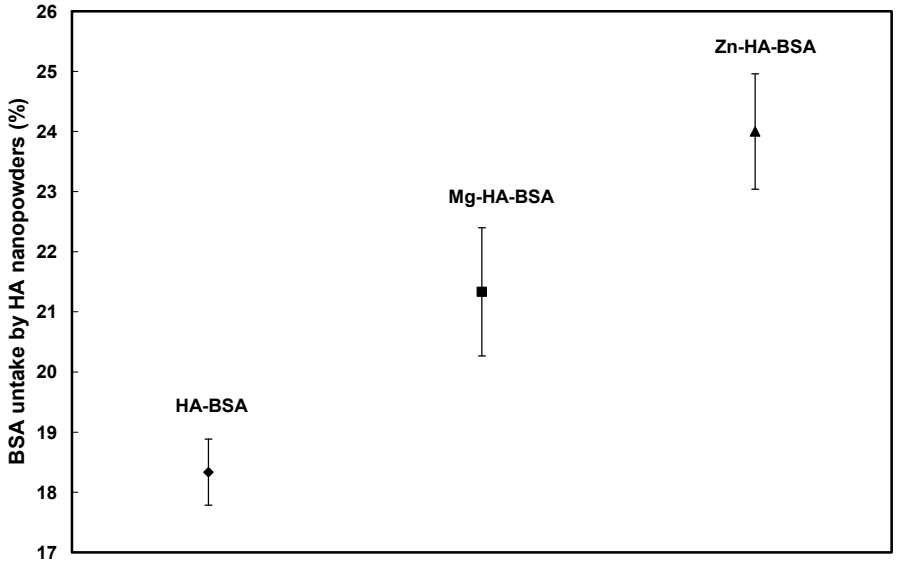

Figure 5.19: Amount of BSA uptake by in-situ synthesized doped and undoped HA-BSA nanopowders

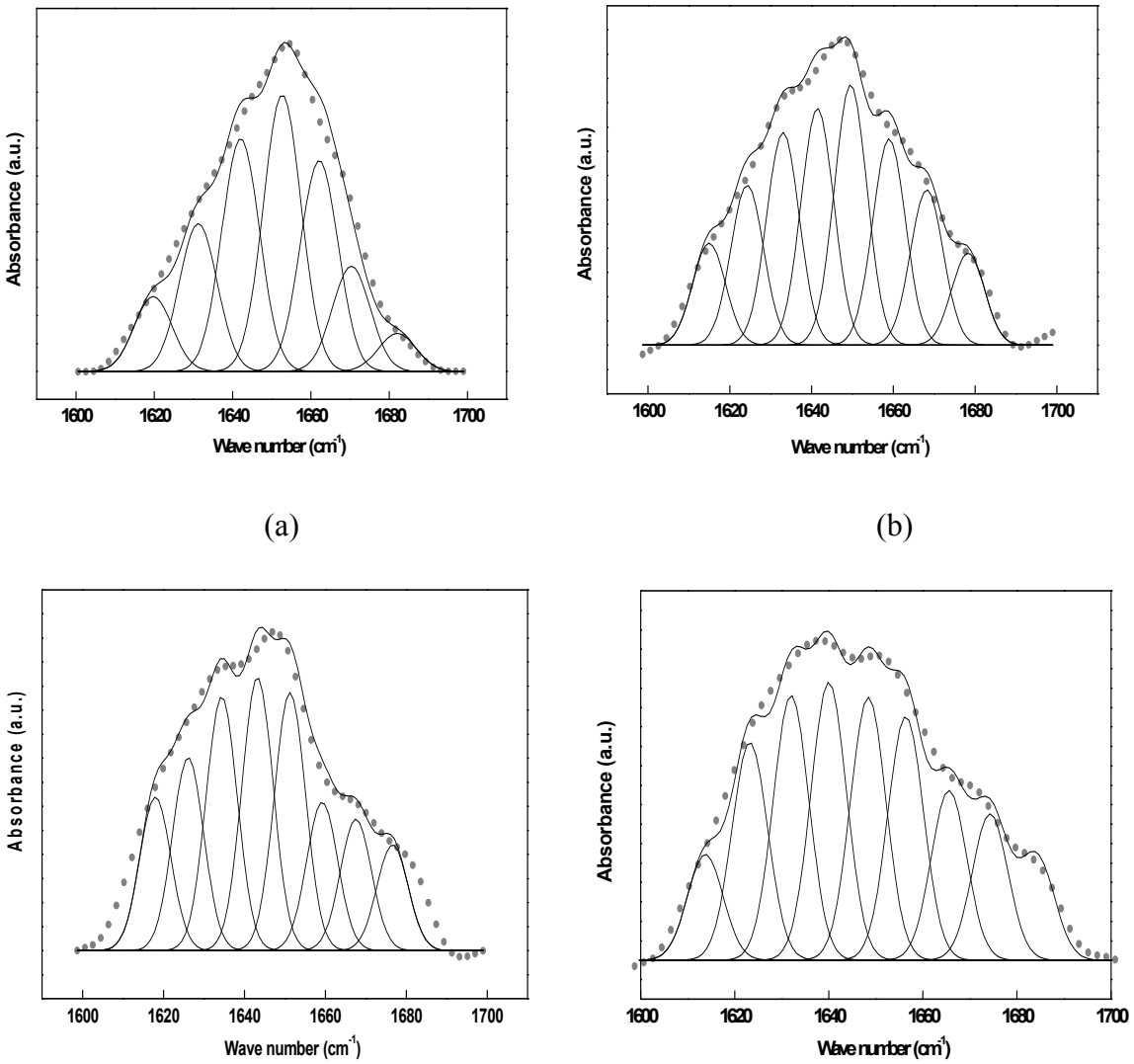

Fig.5.20: Infrared spectra of BSA in the amide I region and their Gaussian curve-fitting (the individual Gaussian bands are shown as symmetrical peaks underneath the IR spectra). Spectra are shown on a relative scale. (a) Pure BSA powder and BSA adsorbed on (b) HA-BSA, (c) Mg HA-BSA and (d) Zn HA-BSA.

Table 5.5: Infrared band assignments of BSA in HA-BSA nanoparticles[244,249, 250]

Band position (cm^{-1})	Secondary structure assignment	Area				References
		Pure BSA	HA-BSA	MgHA-BSA	ZnHA-BSA	
1616±3	Self association	6±1	8±2	6±1	4±1	**244**
1628±3	β-sheet	9±2	12±1	14±2	11±2	**249**
1638±3	β-sheet	15±2	19±2	16±1	16±2	**249**
1648±3	unordered	18±1	20±1	17±1	16±1	**250**
1658±3	α-helix	26±1	17±2	18±2	21±1	**250**
1665±3	α-helix	15±1	11±2	15±1	16±1	**244,250**
1671±3	β-turns	9±3	9±2	9±1	10±2	**249, 244**
1685±2	β-turns	4±2	3±2	6±1	6±1	**250**

Table 5.5 shows the compositional analysis of secondary structure in pure solid BSA powder, doped HA-BSA nanopowders and undoped HA-BSA nanopowder. The α-helix content as determined from FTIR spectra in amide –I region as shown in **figure 5.20 a-d** was found to be 37 %, 33% and 28% for Zn doped, Mg doped and undoped HA-BSA nanopowders respectively**.** The result showed a relative decrease in α –helix content in HA-BSA nanopowders as compared to α- helix content of 41% in pure solid BSA powder. The BSA release profiles of the BSA-loaded doped and undoped HA nanocrystals are shown in **figure 5.21**. It was found that all the samples showed a pronounced bursting behavior for the initial time period of 4 h during which

almost 40% of BSA was released. This was followed by a slower BSA release continued for 4 days. BSA release rate from Zn doped HA nanocrystal found to be significantly higher compared to Mg doped HA-BSA ($p=0.0044$) and undoped HA-BSA ($p<0.0001$) nanopowder. Again Mg doped HA-BSA nanopowder exhibited a significantly higher ($p<0.0001$) BSA release rate compared to undoped HA-BSA nanopowder.

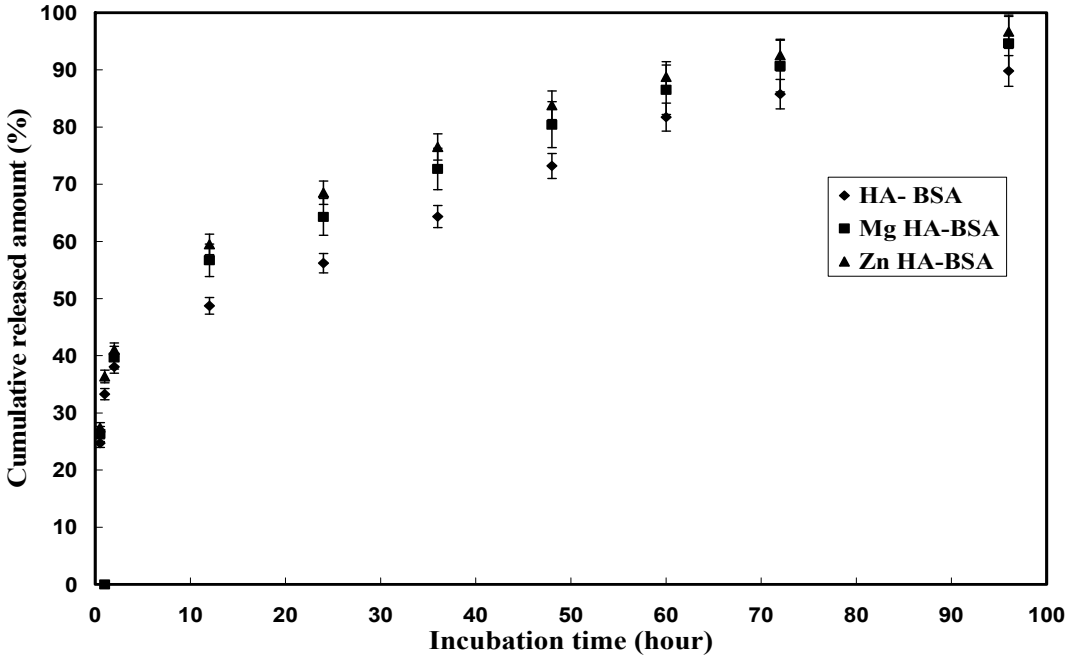

Figure 5.21: BSA release profiles of the BSA-loaded undoped and doped HA nano-carriers

5.3.3 Discussion

The ionic radii of Mg^{2+} and Zn^{2+} are 0.72 and 0.74 Å, which are significantly smaller than 1.00 Å of Ca^{2+}. Thus substitution of Ca^{2+} by Mg^{2+} and Zn^{2+} caused bond strain and decreased crystallinity in HA –BSA nanocrystal. The lower ionic potential of Zn^{2+} imparted higher degree of covalent character in Zn^{2+} - PO_4^{3-} bond as compared to Mg^{2+}- PO_4^{3-} bond and resulted in lower crystallinity of Zn doped HA-BSA nanopowder as compared to Mg doped HA-BSA nanopowder. Addition of dopants, Zn^{2+} and Mg^{2+} into HA crystal lattice caused a reduction

in a –axis and an increase in c-axis and thereby increased the aspect ratio of HA-BSA nanoparticles as reflected in TEM micrographs.[255] The broader particle size distribution for doped HA-BSA nanoparticles than undoped HA-BSA nanoparticles can be attributed to their greater degree of anisotropicity in translational motion in water suspension because of higher aspect ratio of former as compared to later. As synthesis of BSA loaded HA nanopowders was carried out in ambient atmosphere the presence of carbonate in HA-BSA nanopowders is quite expected due to the presence of carbon dioxide (CO_2) in reaction mixture during synthesis process. HA exhibits higher selectivity for Zn^{2+} compared to Mg^{2+} which explains higher amount of Zn^{2+} incorporation into HA lattice.[256] The higher Ca/P ratio in all the HA nanopowders may have resulted from PO_4^{3-} substitution by CO_3^{2-} in HA lattice.

As BSA was added to the reaction mixture an intermediate HA-BSA complex was formed through the electrostatic interaction between Ca^{2+} on the C-sites of HA lattice and COO^- of BSA molecule.[257] The C-sites were developed as a result of Ca^{2+} ions on the HA surface and located on the crystal planes that were perpendicular to a-axis and b-axis of apatite crystal.[258] Preferential inhibition effect on the growth of HA nanocrystals along the ab axis, resulted in higher aspect ratio doped HA-BSA nanoparticle and exposed more number of C-sites for electrostatic interaction between Ca^{2+} of HA lattice and COO^- ions of BSA molecules. Thus aspect ratio of Zn doped HA-BSA nanoparticles being the highest exhibited maximum amount of BSA uptake, followed by Mg doped HA-BSA and undoped HA-BSA nanoparticles.[259]

BSA molecules were incorporated into HA nanocrystals by two types of interaction; one is physical adsorption on the surface of HA nanoparticles which is weak in nature and the other one is strong electrostatic interaction between Ca^{2+} of HA lattice and COO^- ions of BSA molecules. The adsorption of BSA onto HA nano-crystals can be considered as a pseudo-

Langmuir type, where a number of the BSA layers were adsorbed onto HA surface which were not tightly bound with HA nanocrystals.[258] Therefore, for all the HA nanoparticles an exothermic peak was observed at 350 ^{o}C due to thermal decomposition of adsorbed BSA molecule which is close to that of pristine BSA. The exothermic peak at 470 ^{o}C is attributed to the thermal decomposition of tightly bound BSA molecules into HA nanocrystals through strong electrostatic force. A sharper and more intense exothermic peak at around 470 ^{o}C in undoped HA-BSA nanocrystals indicates a stronger HA-BSA interaction in undoped HA-BSA nanopowder compared to doped HA-BSA nanopowders.[224] Undoped HA-BSA nanocrystals being more crystalline than doped HA-BSA nanocrystals exhibited stronger Ca^{2+}-COO^{-} electrostatic interaction as compared to doped HA-BSA nanocrystals.

The decrease in α-helix content in doped and undoped HA- BSA nanopowders indicates that BSA's secondary structural integrity was somehow distorted due to its interaction with HA crystal lattice.[264] The undoped HA nanopowders interacted most strongly with BSA which resulted in a maximum decrease in α-helix content to of loaded BSA molecules. Retention of α-helix structural integrity found to be the greatest for BSA molecules in Zn doped HA-BSA nanopowders primarily because of less intense BSA-HA interaction in Zn doped nanopowders. Again, the secondary structural integrity of protein is retained to a greater extent in *in situ* synthesized HA-BSA nanopowders compared to *ex situ* synthesized CaP-BSA nanopwders. BSA incorporation in *in situ* synthesized nanopowders was mainly governed by hydrophobic interactons between BSA chains, whereas electrostatic interaction between CaP nanoparticles and BSA primarily controlled the BSA adsorption onto *ex situ* synthesized nanoparticle surface. This explains why secondary structure of BSA was retained to a greater extent in *in situ* synthesized HA-BSA nanopowders.

The initial burst release of BSA from HA nanocrystals could be attributed to desorption of BSA molecules which were not tightly bound with HA nanocrystals. The slower BSA release profile in the later stage can be assigned to gradual release of BSA molecules which were incorporated into HA crystals forming BSA–HA complex. The later stage of BSA release was governed by crystal dissolution along c- axis to release incorporated BSA from BSA–HA complex.[260] The crystallinity of HA-BSA nanopowders was in the order, such as, Zn doped HA-BSA< Mg doped HA-BSA< undoped HA-BSA and thus the rate of dissolution of Zn doped HA-BSA nanopowders should be the highest, while undoped HA-BSA nanopowders should dissolve at the slowest rate in phosphate buffer solution at pH-7.2 ±0.2. This explains why the BSA release rate from Zn doped HA-BSA nanopowder was the highest and the slowest rate of BSA release was observed from undoped HA-BSA nanopowder.

5.5 Summary

The objective of this work was to control BSA release from CaP-BSA nanoparticles synthesized via *ex situ* and *in situ* processes. The work has shown that several parameters can influence BSA release from CaP nanoparticles. For both *ex situ* and *in situ* synthesized nanoparticles, two stage BSA release profile was observed. The initial burst release of BSA from nanoparticle surface was mainly due to desorption of loosely bound BSA molecules. The later stage of BSA release was mainly controlled by nanoparticle dissolution to release strongly bound BSA molecules. Some of the general conclusions from this research are as follows.

5.5.1 *Ex situ* Process

- For *ex situ* synthesized CaP-BSA nanopowders, the adsorbed amount of BSA onto CaP nanoparticles decreased from 89 μg/mg to 78 μg/mg with change in average specific surface area from 73 m^2/g to 57 m^2/g, respectively.

- The rate of dissolution of β-TCP phase in buffer medium being much higher compared to CDHA phase, 800 ^{o}C calcined CaP nanopowder showed higher BSA release rate than CaP nanopowders calcined at 600 and 700 ^{o}C.
- At lower pH, the rate of dissolution of β-TCP and CDHA nanoparticles was much higher and hence increasingly higher rate of BSA release was observed.

5.5.2 *In situ* Process

- For *in situ* synthesized HA-BSA nanopowders, the amount of BSA uptake was found to be the highest for Zn doped HA-BSA nanopowder, while undoped HA-BSA nanopowder exhibited the lowest amount of BSA uptake.
- BSA found to interact with undoped HA nanocrystal more strongly compared to doped HA-BSA nanocrystals to form HA-BSA complex.
- Addition of dopants significantly altered the BSA release behaviors of HA nano carriers.
- Zn doped HA-BSA nanocarriers being the least crystalline, released BSA at the fastest rate followed by Mg doped HA-BSA nanopowder and undoped HA-BSA nanopowders.

The study showed that the BSA release rate can be controlled by varying the particle size, surface area, and phase composition of CaP nanoparticles. Addition of dopants such as, Zn and Mg, found to influence the BSA release rate of HA nanoparticles. Constructing a layered structured material that includes CaP nanoparticles having varying particle size, morphology, surface area, and phase composition with different kinds of proteins in each layer, would ensure a predesigned, controlled, and optimized protein release.

CHAPTER-SIX

NANOSTRUCTURED HYDROXYAPATITE AS BONE IMPLANT

6.1. Introduction

6.1.1. Hydroxyapatite as bone implant

As already been discussed in section 2.3.2.1**,** HA shows significant potential to be used as an advanced orthopedic implant because it elicits a favorable biological response and forms a bond with the surrounding tissues.[261-264] However, applications of HA are currently limited to powders, coatings, porous bodies, and nonload-bearing implants due to processing difficulties and the poor mechanical properties of conventional HA.[261-263] Nanostructured HA have mechanical properties substantially different from their conventional coarse-grained counterparts.[265-268] Nanostructure processing improves the sinterability of HA and enhances the mechanical reliability by reducing flaw sizes. The high volume fraction of grain boundaries in nanocrystalline HA compacts also provides increased ductility for low-temperature net-shape forming.[266] Not only the mechanical reliability, but biological functions of synthetic HA are also largely determined by its particle or grain size, morphology, crystallinity, and composition, which depend on the synthesis precursors and processing. Fabrication of fully dense nanostructured HA compact is difficult, especially because most HA powders contain needle-like particles that hinder densification.[268–271] To obtain a nanostructured HA, grain growth should be suppressed during densification, and a lower sintering temperature is thus required without deteriorating the densification. Microwave sintering has been found to be very effective in producing highly dense nanostructured ceramics with ultrafine microstructure.[271]

6.1.2. Microwave sintering of ceramics

Microwave is the electromagnetic radiation in the wavelength range from 1m to 300 mm corresponding to a frequency of about 300 MHz to 300 GHz. This frequency range falls just above radio waves and just below visible light on the electromagnetic spectrum.

61.2.1. Microwave-Material Interactions

61.2.1.1. Dielectric Properties: Material dielectric properties are usually defined in terms of the dielectric constant and the loss tangent. The dielectric constant can be regarded as a measure of the polarizability of a material in an electric field. While the loss tangent is a measure of the absorption of microwaves by the material, the dielectric constant can be defined through the complex permittivity, which is given by the following formula:

$\varepsilon^* = \varepsilon' - \iota\varepsilon'' = \varepsilon^\circ(\varepsilon_r, - i\varepsilon_{eff})$, where ε^* = complex permittivity, ε' = dielectric constant, ε'' = dielectric loss factor, ε° = permittivity in free space, ε_r = relative dielectric constant, ε_{eff} = effective relative dielectric loss factor, and $i = (-1)^{1/2}$. The loss tangent is defined as follows: $\tan\theta = \varepsilon_{eff} / \varepsilon_r$, where $\tan\theta$ = loss tangent. Both the dielectric constant and the loss tangent are functions of temperature.

According to their microwave properties materials can be classified into three categories. Materials with very low loss tangents are transparent to microwaves because they allow microwaves to pass through with very little absorption. Materials with extremely high loss tangents, i.e. metals, reflect microwaves and are considered to be opaque. Materials with intermediate loss tangents generally absorb microwaves. The amount of absorption is quantified by the term skin depth. The skin depth is defined as the distance into the material at which the electric field falls to 1/e or 37% of its initial value. The skin depth is related to frequency, magnetic permittivity and conductivity by the following equation:

SD = $1/(\pi f \mu \sigma)^{1/2}$, where SD = skin depth, f = frequency, μ= magnetic permittivity, and σ= conductivity.

6.1.2.1.2. Loss Mechanisms: Electromagnetic energy can be dissipated in a crystalline dielectric through several loss mechanisms. These mechanisms include electronic polarization, ionic vibration, ion jump relaxation, conduction, and interfacial polarization.

Electronic polarization and ionic vibration are resonance phenomena. Both have the capability to directly change the ion jump frequency, if operable during microwave heating. Electronic polarization would change the energy barrier to be overcome by the jumping ion. On the otherhand, frequency of attempted jumps would be altered by ionic vibration. Microwave frequencies are in the range of 10^9 to 10^{10} Hz, and the ion jump frequency is of the order of the Debye frequency, which is about 10^{13} Hz. Since electronic polarization takes place at even higher frequencies than ionic vibration, both electronic and ionic vibration related loss mechanisms are not thought to be operable at microwave frequencies. Ion jump relaxation in a crystalline ceramic occurs when an aliovalent ion and vacancy form an associated pair. An aliovalent ion-vacancy pair has a dipole moment associated with it that responds to the applied electric field. The vacancy is thought to jump around the aliovalent ion to align its dipole moment with the electric field. Structural inhomogeneity such as grain boundary, dislocation, or vacancy cluster in a material is source of interfacial polarization. In an ionic lattice there will be a localized disruption in electroneutrality at such a structural inhomogeneity with a net dipole moment that will align itself with the applied field. Conduction is of interest at mostly low frequencies. Conduction related loss mechanism occurs when vacancies are not paired with other defects, and hence are not localized. These types of vacancies are much more mobile than associated pairs and migrate in response to the electric field.

6.1.3. Overview of the work

Interaction between cells and implanted materials depends on grain size, and surface properties, which include topography, surface energy, and wettability.[272–275] Such characteristics determine the attachment and orientation of biological molecules that are adsorbed to the biomaterial surface, and affect subsequent cell behavior. Maximum vitronectin, fibronectin, and albumin adsorption were noted on hydrophilic surfaces with high surface roughness and energies. These proteins have been identified to mediate adhesion of specific anchorage-dependent cells, such as osteoblasts, fibroblasts, and endothelial cells, on substrate surfaces.[276, 277] Cell attachment and adhesion are the first phase of cell-material interactions, which further influence cell's capacity to proliferate and to differentiate on contact with the implant. Again surface property of an implant material greatly depends on its grain size. Thus it is very interesting to design implant material with different grain size and investigate cell behavior on the implant surface.

The present work deals with the processing of HA compacts with different grain size using microwave assisted sintering. The variation in mechanical properties, such as compressive strength, indentation hardness and fracture toughness, were evaluated with change in grain size of sintered HA compacts. The bioactivity of different grain sized HA compacts were investigated using human osteoblast cell.

6.2. Nanostructure processing of hydroxyapatite

6.2.1. Experimental

6.2.1.1. Consolidation of HA compacts

Synthesis of HA nanopowders and their characterization have already been discussed in Chapter 4. The as synthesized HA nanopowders were ball milled for 6 hours and then freeze

dried. A suspension of freeze dried HA nanopowders were prepared by dispersing the powders in deionized water with the addition of ammonium polymethacrylate (NH_4PMA) solution (Darvan C, R T Vanderbilt, Norwalk, CT, USA), using mechanical stirring. The amount of NH_4PMA used in suspension is expressed as a dry weight of the powder basis, equivalent to the wt./wt. basis of the HA nanopowders. The suspension was dried in an oven at 150 C and used for the preparation of HA compacts.

Dried powders were pressed into tablets with approximately 12.4-12.7 mm in diameter and 2.1–2.3 mm in height using uniaxial pressing at 50 MPa, followed by cold isostatic pressing at 345 MPa. Cylindrical HA compacts with approximately 5.4 to5.6 mm in diameter and 9.1 to 11.6 mm in height were prepared using the same technique.

6.2.1.2. Sintering of HA compacts

The green HA compacts were calcined in a conventional muffle furnace at 600 ^oC for 2 h to burn out the surfactant. HA compacts were then sintered in a 3 KW microwave furnace at different temperature for different time interval. The compacts prepared from HA nanopowders were sintered at 1000, 1100 and 1150 ^oC for 20 minutes. After sintering the compacts were thermally etched at 800 ^oC for 30 minutes in a conventional muffle furnace.

6.2.1.3. Characterization of HA compacts

Sintered compacts were characterized for bulk density, phase composition, microstructural analysis, microhardness, fracture toughness and compressive strength.

A. Bulk density measurement: The bulk densities of the green and sintered compacts were measured from the sample dimension and mass of the compacts according to following equation.

B.D.= [(M/V)/ ρ_{th}] x 100, where M= mass of the compact, V= volume of the compact= $1/4\pi d^2$ l when d and l are the diameter and thickness of the compact, and ρ_{th} is the theoretical density of the sample.

B. Phase analysis: The phases of sintered HA and β-TCP compacts were determined using a Philips fully automated x-ray diffractometer with Cu-K_α radiation (1.54018 A) and a Ni- filter. The diffractometer was operated at 35 kV and 30 mA. The XRD data were collected at room temperature over the 2θ range of 20^o- 60^o at a step size of 0.02^o and a count time of 0.5 s/step.

C. Microstructure analysis: The microstructure of sintered compacts was characterized using SEM (Hitachi S570, Hitachi Scientific Instrument, CA). The samples were gold-sputter coated and SEM analysis was performed at an acceleration voltage of 20 KV. HA grain sizes were determined from the SEM images via a linear intercept method. [278]

G = (L/N) C, where G is the average grain size (μm), L is the test line length (cm), N is the number of intersections with grain boundaries along test line L; and C is the conversion factor (μm/cm) of the picture on which the test lines were drawn as obtained from the scale bar.

D. Mechanical characterization of sintered compacts

The sintered HA tablets were characterized for microhardness and indentation fracture toughness measurement. Compression strength analysis was performed with cylindrical HA compacts.

(a) Microhardness measurement: Microhardness of sintered HA compacts was evaluated using Vicker's diamoand indenter (LECO Corporation, St. Joseph, MI. First the samples were mounted on epoxy resin and then polished on sand paper and cottonpads using alumina suspension. After polishing with 0.03 μm alumina suspension, microhardness measurement was carried out. 500 g

load was used for microhardness measurements, and the value was calculated from the indentation size.

(b) Indentation fracture toughness measurement: Fracture touighness was calculated from the radial crack length that appeared after the indentation test. The equation for the calculation of fracture toughness was given below. [279]

Fracture toughness ($K_{IC} = 0.016X\ (E/H)^{1/2}X\ P/C^{3/2}$.

Where E is Young's modulus of the sample, H is microhardness in GPa, P is the applied load and C is the half of the crack length.

(c) Compressive strength measurement: The cylindrical HA compacts were prepared to maintain diameter to height ratio > 1:2 for compressive strength measurement. Compressive strength of the samples was measured using a screw driven Instron compression test machine. Cross head speed was maintained at 0.0002 cm/sec. Compressive strength was calculated from failure strength and cross sectional area of the sample.

Three sintered samples at each sintered cycle were used for the measurement of microhardness, fracture toughness and compressive strength.

- **Calculation of hardness**

$H = 1.854\ F/d^2 = 1.854 \times [0.5\ Kg/\ (0.033\ mm)^2] = 851.239\ Hv = 8.345\ GPa$

- **Calculation of fracture toughness**

$$K_{IC} = 0.016\left(\frac{E}{H}\right)^{\frac{1}{2}} \frac{P}{C^{\frac{3}{2}}} = 0.016\left(\frac{129}{8.345}\right)^{\frac{1}{2}} \frac{0.5X9.81}{\left(28X10^{-6}\right)^{\frac{3}{2}}} = 2.06MPam^{\frac{1}{2}}$$

6.2.2. Results

6.2.1.1. Consolidation and sintering of HA nanocompacts

The freeze dried HA nanopowders synthesized using reverse micelle as template system were consolidated and sintered in microwave furnace to fabricate dense HA compacts. The green density of HA nanocompacts that were processed without any dispersant was in the range between 45 to 47 % and not more than 89% of sintered density was obtained even after sintering at 1150 ^{o}C for 30 minutes. Different amount of ammonium polymethacrylate dispersant was used to prepare slurry from HA nanopowders and the dispersant added to HA nanopowders significantly improved the green density of HA compacts. Though from **table 6.1** it is clear that only 6 wt% of NH_4PMA was found to be effective in improving both green and sintered density simultaneously resulting in microstructure with finer and narrower grain size distribution.

Table 6.1: Processing of HA nanocompacts by adding different amount of dispersant

Surfactant (wt%)	Relative green density (%)	Sintering cycle (^{o}C) /min	Relative sintered density (%)	Grain size (μm)	Comments
2	51.25	1100/20	87.27	0.8-1.5	Wide grain size distribution
4	53.85	1100/20	90.52	0.44-0.9	Wide grain size distribution
4	53.85	1150/20	89.81	----------	Melted surface
6	56.84	1100/20	96.98	0.41-0.64	Relatively narrow grain size distribution
6	57.82	1000/20	98.72	0.12- 0.47	Relatively narrow grain size distribution , high sintered density
6	56.98	1150 /20	97.48	0.92-1.27	Relatively narrow grain size distribution , high sintered density
8	53.42	1100/20	86.89	----------	Melted surface
10	55.82	1100/20	85.82	---------- --	Melted surface

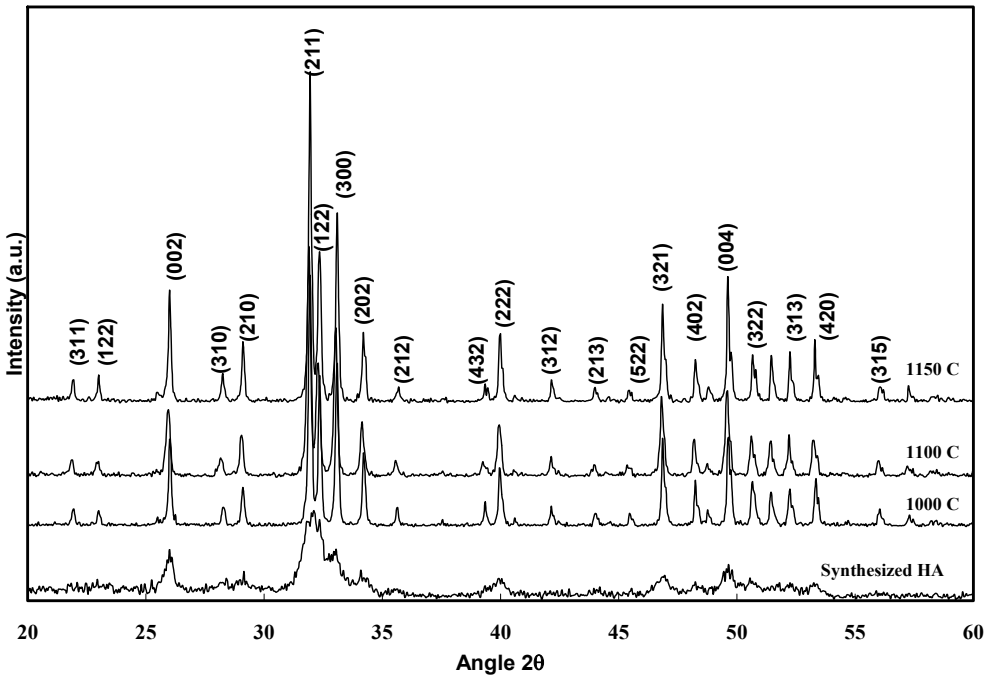

Figure 6.1: X-ray diffraction of HA pellets sintered at different temperature in microwave furnace for 20 minutes. In all cases the green HA compacts were processed with 6 wt% dispersant and then consolidated.

Figure 6.1 shows the diffraction pattern of HA pellets sintered in microwave furnace at 1000, 1100 and 1150 ^{o}C for 20 minutes. All the sintered pellets showed phase pure HA (JCPDS 09-0432). The relative green density of HA compacts were above 56 % and after sintering all the compacts showed a relative sintered bulk density greater than 97 %. **Figure 6.2** shows the microstructures of HA compacts sintered at 1000, 1100 and 1150 ^{o}C for 20 minutes. With increase in sintering temperature from 1000 C to 1150 ^{o}C the average grain size of sintered HA compacts increased from 0.16 μm to 1.17 μm as shown in **figure 6.3**.

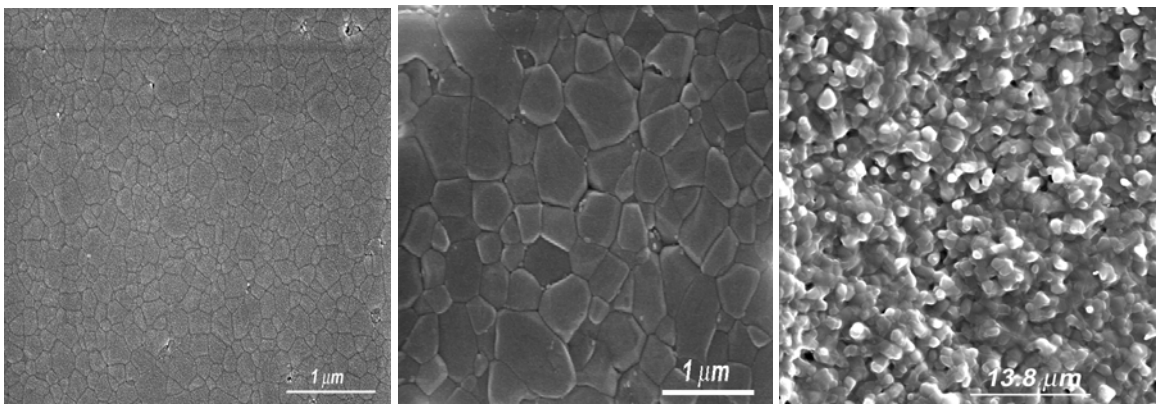

(a) (b) (c)

Figure 6.2. Microstructure of HA pellets sintered for 20 minutes in microwave furnace at (a) 1000 ^{o}C, (b) 1100 ^{o}C and (c) 1150 ^{o}C

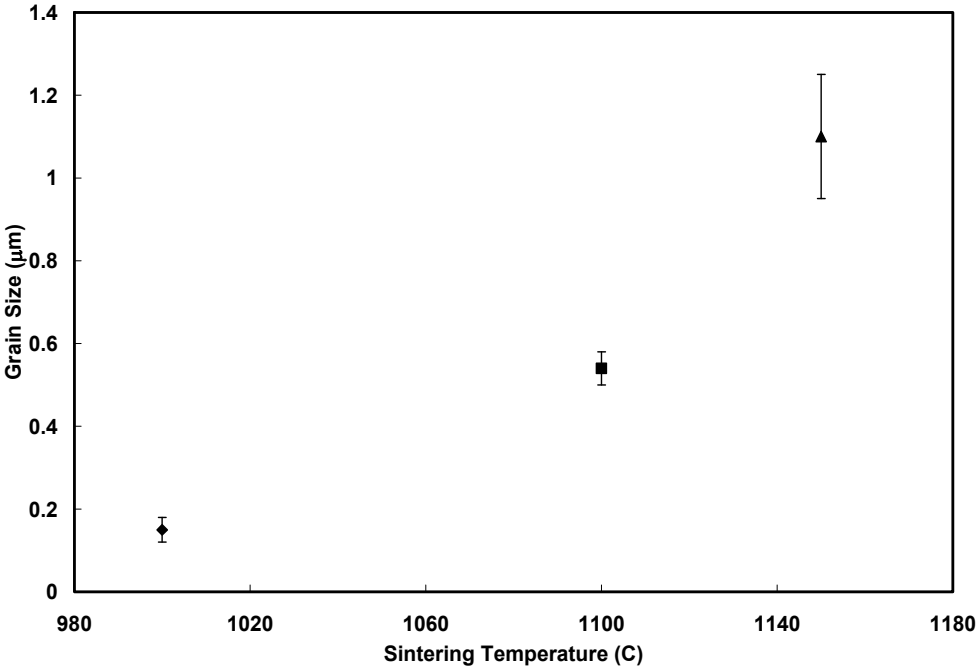

Figure 6.3. Grain size of HA discs with increase in sintering temperature in microwave furnace

6.2.2.2. Mechanical characterization of HA compacts with fine microstructure

The bulk densities of HA compacts sintered at 1000, 1100 and 1150 ^{o}C were greater than 97 %. That means the change in sintering temperature from 1000 to 1150 ^{o}C did not exert any significant effect on the bulk densities of HA compacts, but the grain size of sintered HA compacts varied greatly with change in sintering temperature from1000 to 1150 ^{o}C as already

been discussed in earlier section. The effect of grain size on the compressive strength of HA compacts is shown in **figure 6.4**. As expected the compressive strength of HA compacts increased with decrease in grain size. HA compacts with a grain size of 0.16 μm showed an average compressive strength of around 400 MPa, which is greater than the compressive strength value of compact bone and dental enamel. The average values of Young's modulus also decreased with decrease in grain size as depicted in **table 6.2**.

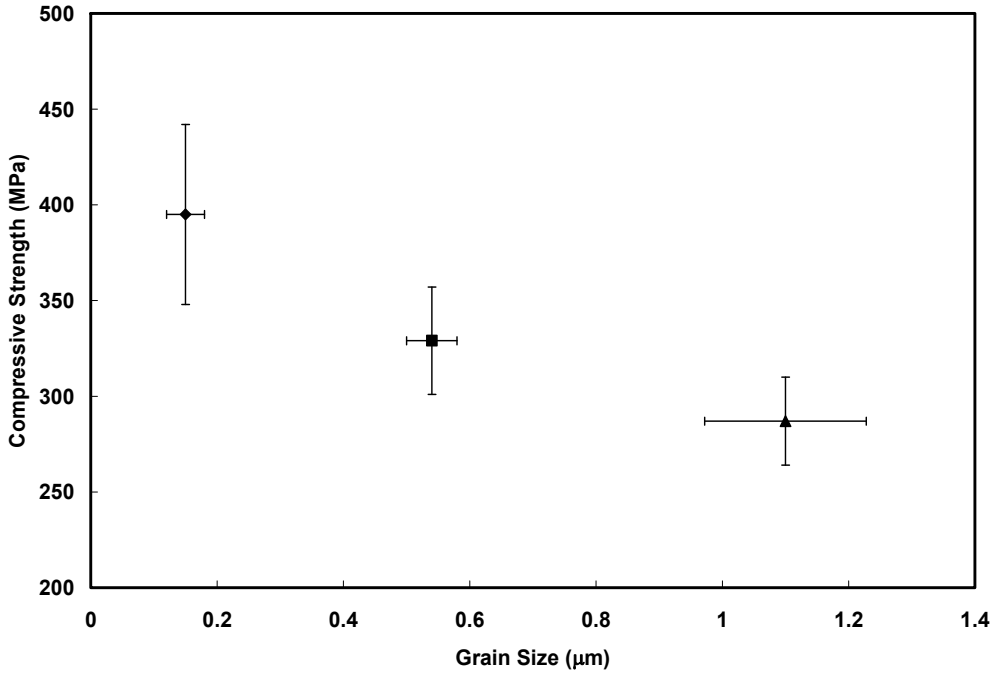

Figure 6.4: Effect of grain size on compressive strength of sintered HA pellets

Table 6.2.Values of Young's modulus for different grain sized HA compacts

HA grain size (μm)	Young's modulus (MPa)
0.168±0.086	129± 5
0.54±0.035	123± 4
1.1±0.128	115± 6

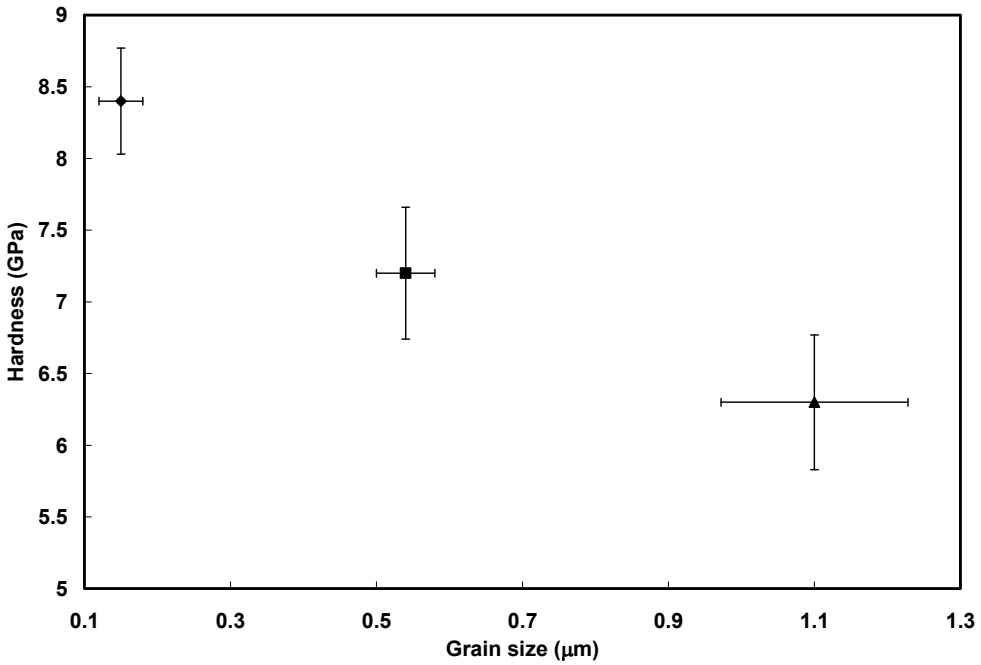

(a)

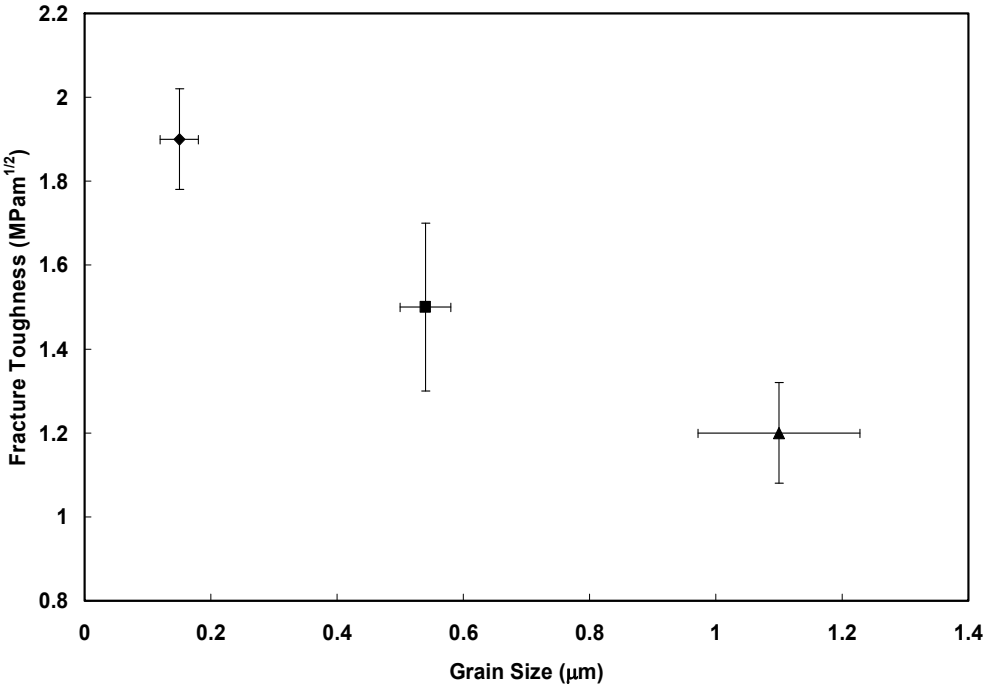

(b)

Figure 6.5: Effect of grain size on indentation (a) microhardness (b) fracture toughness of sintered HA discs

Figures 6.5 (a) and 6.5 (b) show the variation in hardness and fracture toughness with change in grain size in sintered HA compacts. With increase in grain size hardness of sintered HA compacts decreased. The average microhardness value of HA compacts with an average grain size of 0.16 μm was 8.4 GPa, whereas the HA compacts with average grain size of 1.1 μm showed an average microhardness value of 6.3 GPa. Similarly fracture toughness of HA compacts increased with decrease in grain size. HA compacts with an average grain size of 0.15 μm exhibited a maximum fracture toughness of 2.0 $MPam^{1/2}$ which is close to the lower limit of fracture toughness of natural bone. SEM micrographs of some of the indents made at a load of 500 g on nano and micron grained HA compacts are shown in **figure 6.6**. It is clear that the size of indentation as well as radial crack length decreased with decrease in grain size.

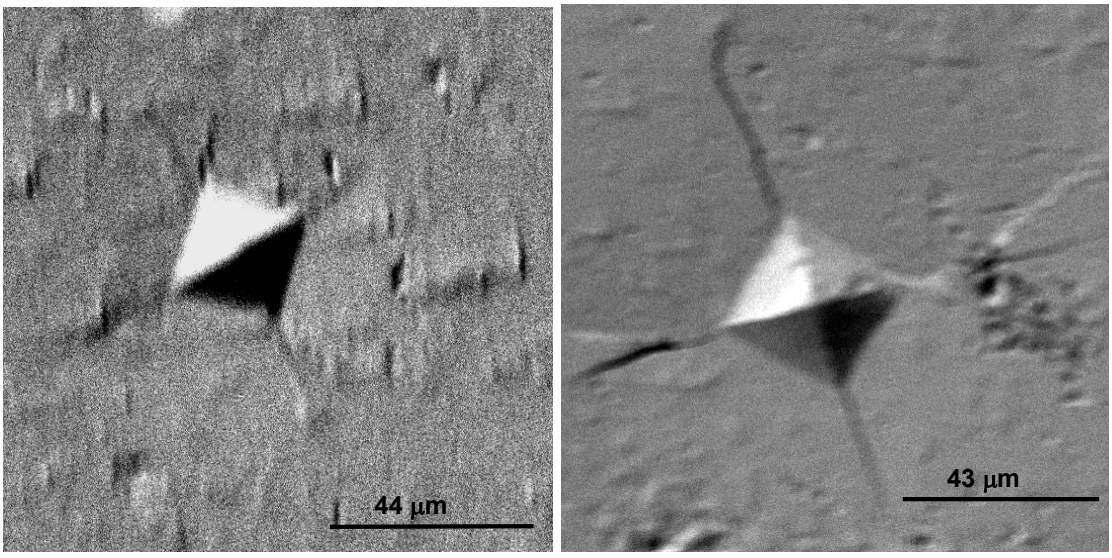

(a) (b)

Figure 6.6. Back scattered micrographs of indentations done on HA compacts with different grain size (a) 0.168±0.086 μm and (b) 1.1 ± 0.128 μm, at a load of 500 g

6.2.3. Discussion

Due to high surface area of synthesized HA nanopowders it experienced high frictional resistance during consolidation into compacts which resulted in poor green density. NH_4PMA is

an anionic polyelectrolyte and can dissolve in aqueous solution, producing negatively charged carboxyl groups as shown in **equation 6.1**, which are very easily adsorbed on the positively charged HA surface. The dissociation of NH_4PMA in water can be described as follows:

$RCOONH_4 \rightarrow RCOO^- + NH^{+4}$ ……(6.1).

NH_4PMA effectively dispersed HA nanopowders through an electrosteric mechanism of dispersing action. The role of NH_4PMA was to disperse agglomerate free HA nanopowders as well as to minimize frictional resistance during consolidation to improve green density of HA nanocompacts. Optimization of the amount of NH_4PMA was very essential during preparation of slurry to maximize its dispersing action. Lower amount of NH_4PMA kept HA nanopowders agglomerated whereas excess amount NH_4PMA led to bridging flocculation, which hampered consolidation of HA green compacts. In this case, 6 wt% NH_4PMA found be the most effective in improving green density as well as sintered density of HA nanocompacts. An increase in sintering temperature had an obvious effect on increasing the grain size of sintered HA compacts due to growth of HA crystallites.

There are several literature reports available, discussing superior strength and higher fracture toughness for finer microstructures in comparison with coarser ones.[280] Since relative bulk density of HA compacts were all above 98 %, the hardness and fracture toughness of HA compacts were solely affected by its grain size. The influence of grain size on the hardness of HA compacts can be explained by Hall–Petch equation: $H = H_i + kd^{-1/2}$, where H_i is the lattice friction stress, k is the Hall–Petch constant and d is the grain size of HA compact. With decrease in grain size in HA compacts, the relative volume of grain boundaries increased. Thus resistance to indentation was increased due to higher amount of stored energy from increased number of grain boundaries in smaller grained HA compact. Similarly the increase in fracture toughness of

HA compacts with decrease in grain size can be attributed to increased resistance to crack propagation due to the presence of more number of grain boundaries in nanograined HA as compared to submicron or micron grained HA compacts. Again the reduced flaw size with decrease in grain size in HA compacts was responsible for increase in compressive strength with similar decrease in grain size in HA compacts.

6.3. HA compacts prepared from calcined powders

6.3.1. Experimental

6.3.1.1. Consolidation of calcined HA powders

The as synthesized HA nanopowders were calcined at different temperature for different time as depicted in **table 6.3**

Table 6.3: Calcination cycle of as synthesized HA nanopowders

HA powders	Processing steps	Calcination
HA (I)	Ball milling, Freeze drying, Suspended with dispersant NH_4PMA, oven dried	None
HA (II)	None	800 ^oC / 4 h
HA (III)	None	900 ^oC / 10 h

Particle size of HA (I), HA (II) and HA (III) powders were measured using DLS technique as described in section 4.2.4.2. HA (I) nanopowders were processed using the same procedure as described in section 6.2.1.1**.** Discs with approximate dimensions of 12.4-12.7 mm in diameter and 2.1–2.3 mm in height were prepared from HA (I), HA (II) and HA (III) powders by uniaxial pressing at 50 MPa, followed by cold isostatic pressing at 345 MPa. Cylindrical HA (I), HA (II) and HA (III) compacts with approximately 5.4 to5.8 mm in diameter and 9.1 to 11.2 mm in height were also prepared using the same technique.

6.3.1.2. Sintering of HA (I), HA (II) and HA (III) compacts

The discs and cylindrical HA compacts prepared from HA (I), HA (II) and HA (III) powders were sintered in a 3 KW microwave furnace at different temperature for different time interval as described in **table 6.4**.

Table 6.4 Sintering cycle of different HA compacts

HA compacts	Sintering cycle (^{o}C / min)
HA (I)	1000/ 20
HA (II)	1150/ 30
HA (III)	1150/ 45

6.3.1.3. Characterization of HA (I), HA (II) and HA (III) compacts

The phase, microstructure and mechanical properties of sintered HA (I), HA (II) and HA (III) compacts were analyzed using the same procedures as described in section 6.2.1.3. Surface properties such as wettability, surface energy of HA compacts were evaluated by measuring contact angle of different liquids on HA discs. Bioactivity and *in vitro* cell –materials interaction of HA compacts were studied using human osteoblast cell line (Hfob 1.19 osteoblast).

A. Surface analysis

(a) Contact angle measurement

Contact angles of different liquids on sintered HA disc surface were measured using the sessile drop method on a face contact angle set-up equipped with a microscope and a camera. Contact angles were determined with liquids such as water, formamide, glycerol, and cell culture media. A 0.5-1.0 µl droplet of each liquid was suspended from the tip of the microliter syringe. The syringe tip was advanced toward the disk surface until the droplets made contact with the

disk surface. Images were collected using the camera and the contact angle between the drop and the substrate was measured from the magnified image. Three samples at each sintering cycle were used to collect the contact angle data. For each samples again three data points were used.

(b) Surface Energy

Contact angles were determined with three different liquids to calculate surface energy. Apolar liquid diiodomethane and two polar liquids formamide and glycerol were used in the following equation to calculate the surface energy.

$$\gamma_L(1+\cos\theta) = 2\,(\gamma_S^{LW}\gamma_L^{LW})^{1/2} + 2(\gamma_S^{+}\gamma_L^{-})^{1/2} + 2(\gamma_S^{-}\gamma_L^{+})^{1/2} \quad (6.2)$$

In equation (1) θ is the contact angle of liquid L and solid S, γ^{LW} is the apolar component of the surface energy, γ^{+} is the Lewis acid component (electron acceptor) and γ^{-} Lewis base component (electron donor).[281]

Table 6.5. Surface Tension Data (mJ/m^2) on the three contact angle liquids.[265]

Liquid used	**γ_L (mJ/m^2)**	**γ_L^{LW} (mJ/m^2)**	**γ_L^{+} (mJ/m^2)**	**γ_L^{-} (mJ/m^2)**
Water	72.8	21.8	25.5	25.5
Glycerol	64	34	3.92	57.4
Formamide	58	39	2.28	39.6

- **Example for the calculation of surface energy for nano HA surface**

Table 6.6: Contact angle values of different liquids on nano HA surface

Contact Angle (degree)	**Water**	**Glycerol**	**Formamide**
	34.95±1.88	40.55±3.93	29.18± 4.07

Inserting the contact angle values from **table 6.6** and surface tension data from **table 6.5** in **equation (6.2)** we get

$$(39\,\gamma_S^{LW})^{1/2} + (2.28\,\gamma_S^{+})^{1/2} + (39.6\,\gamma_S^{-})^{1/2} = 54.32\ldots\ldots\ldots\ldots \quad (6.3)$$

$$(21.8\,\gamma_S^{LW})^{1/2} + (25.5\,\gamma_S^{+})^{1/2} + (25.5\,\gamma_S^{-})^{1/2} = 66.235\ldots\ldots\ldots\ldots..(6.4)$$

$$(34\gamma_S^{LW})^{1/2} + (3.92\gamma_S^{+})^{1/2} + (57.4\gamma_S^{-})^{1/2} = 56.31\ldots\ldots\ldots\ldots \quad (6.5)$$

Solving these three equations 6.3, 6.4 and 6.5 by Cramer's rule we get

$\gamma_S^{LW} = 39.87$ mJ/m^2, $\gamma_S^{+} = 48.086$ mJ/m^2, $\gamma_S^{-} = 0.742$ mJ/m^2

Now, $\gamma_S = \gamma_S^{LW} + \gamma_S^{+} + \gamma_S^{-}$

$\gamma_{HA\,(I)} = \gamma_S^{LW} + \gamma_S^{+} + \gamma_S^{-} = 39.87 + 48.09 + 0.74 = 88.7$ mJ/m^2

Surface energy is a measure of the extent to which bonds are saturated or unsaturated at the surface of a material. At the surface, there is an asymmetric force field which results in a net attraction of surface atoms into the bulk. This asymmetric force renders the sample surface in tension. When a liquid drop is placed onto a solid surface it may wet the surface completely or partially by spreading over the solid surface or it may sit on the surface in the form of droplet without spreading at all, the phenomenon called absolute non wetting. Which event occurs depends upon the relative interfacial free energies of the liquid and solid substrate. The interfacial free energy is analogous to surface free energy but accounts for the interactions of the materials on either side of the interface.

B. *In vitro* cell –material interaction

In vitro cell-material interaction was studied using human osteoblast cells (OPC1) cultured onto disc samples for 1, 5 and 11 days. SEM, MTT assay and confocal microscopy were used to study osteoblast cell attachment, spreading, proliferation and differentiation on sample surface.

(a). Osteoblast Cell line

Human osteoblast cells (hFOB 1.19 Osteoblast) were purchased from ATCC (Manassas, VA). Cells were plated at a density of 10^5 /cm^2 in 100 mm tissue culture plates, and were cultured in Dulbecco's modified eagle's medium (DMEM) (with L-glutamine, without phenol red). Composition of the medium is shown in **table 6.7**. Cells were maintained at 37 ^oC under an atmosphere of 5% CO_2 and 95% air to attain confluence. These cells were then splitted into 1:2 ratios and seeded onto each sample surface.

Table 6.7 Compositions of cell media for 1000 ml batch

Chemicals	Quantity
Water	900 ml
DMEM	15.6 g
Sodium bicarbonate	1.2g
Fetal Calf Serum	100 ml

(b). Seeding of osteoblast cells onto disc surface

Old medium onto the confluent culture plate was removed off. The plate was rinsed with phosphate based buffered saline and then 2 ml of trypsin enzyme was added onto the plate and incubated for 3-5 minutes. Trypsin helps in digesting the attachment proteins of the cell from the culture plate and detaches the cells from culture plate. Fresh 6 ml of the McCoy's 5A medium was added to inactivate the trypsin. Part of the trypsinzed cells was used to seed on the surface of the sample and another part was kept for future use in cryogenic atmosphere.

The whole 8 ml solution with cell suspension was transferred to a conical vial. Approximately 7.5 ml of cell suspensions were spread under the cover slip on each side of the haemocytometer. There were 8 grids in hemocytometer and cells were counted on each of the grids using. The following calculations were performed to find the volume of cell suspension needed on each of the samples.

- **Calculations to determine the volume of the cell suspension**

Number of cells/8 grids= A

A (1.0×10^4)= B, cell count, cells/ml

For 12-well plate: (2×10^4)/B ml of the volume of cell suspension to seed onto each substrate in each well.

For 100 mm plate: (1×10^5)/B

Example of the calculation is provided below:

No. of cells counted/grid= 478

No. of cells counter/grids= 478/8 = 59.75=A

59.75 (1×10^4) = B

For 100 mm plate: (1×10^4) / (59.75×10^4) = 0.167 ml =167 µl

Discs samples were sterilized by autoclaving (AST Products Inc, VC Optima, Billerica, MA Billerica, MA) for 20 minutes at 121 ^{o}C before cell culture. Osteoblast cells were seeded onto the sterilized disc surface. Culture medium was changed every 2-3 days for the duration of experiment. Samples were then removed from culture medium at 1, 5 and 11 days of incubation to study cell-materials interactions.

(c) Study of cell morphology using SEM

There are six major steps for tissue preparation for electron microscopy which include: primary fixation, washing, secondary fixation, rinsing, dehydration, critical point drying.[282] The purpose of fixation is to preserve the structure of living tissue unaltered from living state. Additionally fixation protects tissues against disruption during exposure to the electron beam. The primary fixative is a combination of 2% glutaraldehyde and 2 % formaldehyde in either 0.1

(M) cacodylate or 0.1 (M) phosphate buffer solutions. Formaldehyde ensures rapid initial fixation of the tissue because it penetrates the tissue more readily (1mm/ h) than glutaraldehyde. Glutaraldehyde, by virtue of its terminal aldehyde groups, fixes the cells onto substrate surface by cross-linking cellular proteins. Constituents of the cell would be unified into a single interlocking structure or mesh work held together by a multitude of glutaraldehyde molecules. Secondary fixative, osmium tetroxide, works primarily by reacting with lipid moieties. It is widely believed that the unsaturated bonds of fatty acids are oxidized by osmium tetroxide, with osmium tetroxide being reduced to black metallic osmium.[282] This reduced heavy metal adds density and contrast to the biological tissue. Penetration of osmium tetroxide is slower than glutaraldehyde (about 0.5 mm/h). Buffers like cacodylate and phosphates are used for subsequent rinsing purposes. As fixative lowers the pH of the tissues during the fixative process, artifacts may be produced. The buffering system maintains physiologic pH (e.g. 7.2 to 7.4) resulting in fewer artifacts. After primary fixation with glutaraldehyde, the tissue is usually washed in the same buffer vesicle used in glutaraldehyde fixation step. Washing is extremely important because it eliminates any free unreacted glutaraldehyde that remains within tissues. Aldehydes remaining from the primary fixation will be oxidized by osmium tetroxide. Dehydration is the process of replacing the water in cells with a fluid that acts as a solvent between the aqueous environment of the cell and the hydrophobic embedding media. Water is a highly polar molecule that is, by far, the major component of virtually all cells. Common dehydrating agents are ethanol or acetone. Ethanol is a widely used dehydrating agent for acetone because anhydrous acetone absorbs water from the atmosphere and is a more powerful extractor of lipids within the cell. Usually 30% ethanol is the first solvent that tissue is exposed to after secondary fixation followed by 50%, 70%, 95% and 100%. As one reaches higher concentrations of the dehydrating

agents, the time that tissue is exposed to the dehydration agent are increased in order to eliminate the small amount of water remaining in the tissues.

For SEM observation, cell-cultured disc samples were placed in 0.1M phosphate buffered saline (PBS) and rinsed quickly. Samples were subsequently fixed with 2% paraformaldehyde and 2% glutaraldehyde in 0.1 M cacodylate buffer overnight at 4 ^{o}C. Following three rinses in 0.1 M cacodylate buffer, each sample was post-fixed in a secondary fixative (2% osmium tetroxide (OsO_4) for two hours at room temperature). The fixed sample was then again rinsed three times in 0.1 M cacodylate and dehydrated in an ethanol series (30%, 50%, 70%, 95% and 100% three times). Samples were then critical-point dried using acetone and hexamethyldisilazane (HMDS). Samples were mounted on aluminum stubs, gold sputter coated (Technis Hummer, San Jose, CA), and observed under SEM.

(d) Study of cell proliferation using MTT assay

To estimate the number of cells, we will employ a colorimetric assay (MTT assay), which quantities the ability of mitochondrial dehydrogenases to metabolize 3-[4, 5-dimethylthiazol-2-yl]-2, 5-diphenyl-tetrazolium bromide to an insoluble formazan. MTT (Sigma, St. Louis, Mo) solution of 5 μg /ml was prepared by dissolving MTT in PBS, and filter sterilized. MTT was diluted with 50 μl of the solution in 450 μl of serum free phenol red-free Dulbeco's Minimum Essential medium (DME). 500 μl of the above-diluted solution were used in each sample in 24-well plates to form formazan by mitochondrial dehydrogenases. After 2-hours of incubation at 37 ^{o}C, 500 μl of the solubilization solution (10% triton X-100, 0.1N HCl and isopropanol) were added in each well plate to dissolve the formazan crystals. The 100 μl of the solution was then transferred to new 96 wells plate and 8 data points were obtained from each sample. The purple color of the formazan provides an optical density number which is also a measure of cell density.

Optical density of the solution in each well was measured at wavelength of 570 nm using a Microplate reader (Cambridge Tech., Inc., EIA). Data are presented as mean of 8 values with standard deviation.

(e) Immunochemistry and confocal microscopy

Human bone cells can bind to implant surface via proteins called integrins ($\alpha_5\alpha_1$ and β_1). Integrins mediated contacts between cells and their substratum influence cell adhesion, migration and spreading. It is important to see the effect of each of these proteins family on the substrate to understand the cell adhesion, differentiation, spreading and mineralization behavior. Vinculin is a membrane-cytoskeletal protein in focal adhesion plaques that is involved in linkage of integrin adhesion molecules to the actin cytoskeleton.[283] Cell spreading and movement occur though the process of binding of cell surface integrin receptors to extracellular matrix adhesion molecules. As an adhesive molecule, vinculin aids in the assemblage of focal contact by crosslinking and recruiting other proteins to form adhesion plaques.[284]

Cell differentiation on HA compacts will be evaluated using alkaline phosphatase (ALP) phenotypic expression. ALP is a hydrolase enzyme responsible for removing phosphate groups from many types of molecules, including nucleotides, proteins, and alkaloids. ALP is produced by bone-forming cells called osteoblasts, a feature of the osteoblast phenotype. ALP expression appears strongly positive in differentiating osteoblastic cell. ALP is regarded as an early marker for osteoblast differentiation, and it is generally accepted that as the specific activity of ALP in a population of bone cells increases there is a corresponding shift to a more differentiated state.[285] Osteoblasts create a local environment of alkalinity through ALP and helps build bone. Adhesion of cells to HAp surface will be qualitatively evaluated by vinculin expression.

Cells cultured on disc samples for a pre-specified number of days were fixed in 4% paraformaldehyde in 0.1M phosphate buffer and were kept for 24h at 4 ^{o}C for future use. Those samples were rinsed in Triton X for 10 minutes and blocked with TBST/BSA (tris-buffered saline with 1% bovine serum albumin, 250 mM NaCl, pH 8.3) for 1 hour. Primary antibody alkaline phosphatase (ALP) (Sigma-Aldrich, St. Louis, MO) or vinculin (Sigma-Aldrich, St. Louis, MO) was added at a 1:100 dilution and incubated at room temperature overnight. Vinculin was used to study cell attachment, while ALP was used for investigating on cell differentiation. The following day, samples were rinsed with TBST/BSA three times for 10 minutes each. The secondary antibody, Oregon green goat anti-mouse (GAM) (Molecular Probes, Eugene, OR), was added at 1:100 dilution and incubated at room temperature for one hour. Samples were then mounted on coverslips with Vectashield Mounting Medium (Vector Labs, Burlingame, CA) with propidium iodide (PI) and observed in confocal scanning laser microscopy (BioRad 1024 RMC, Hercules, CA, USA). **Figure 6.7** shows the schematic of the protocols for vinculin and ALP study on cell cultured samples.

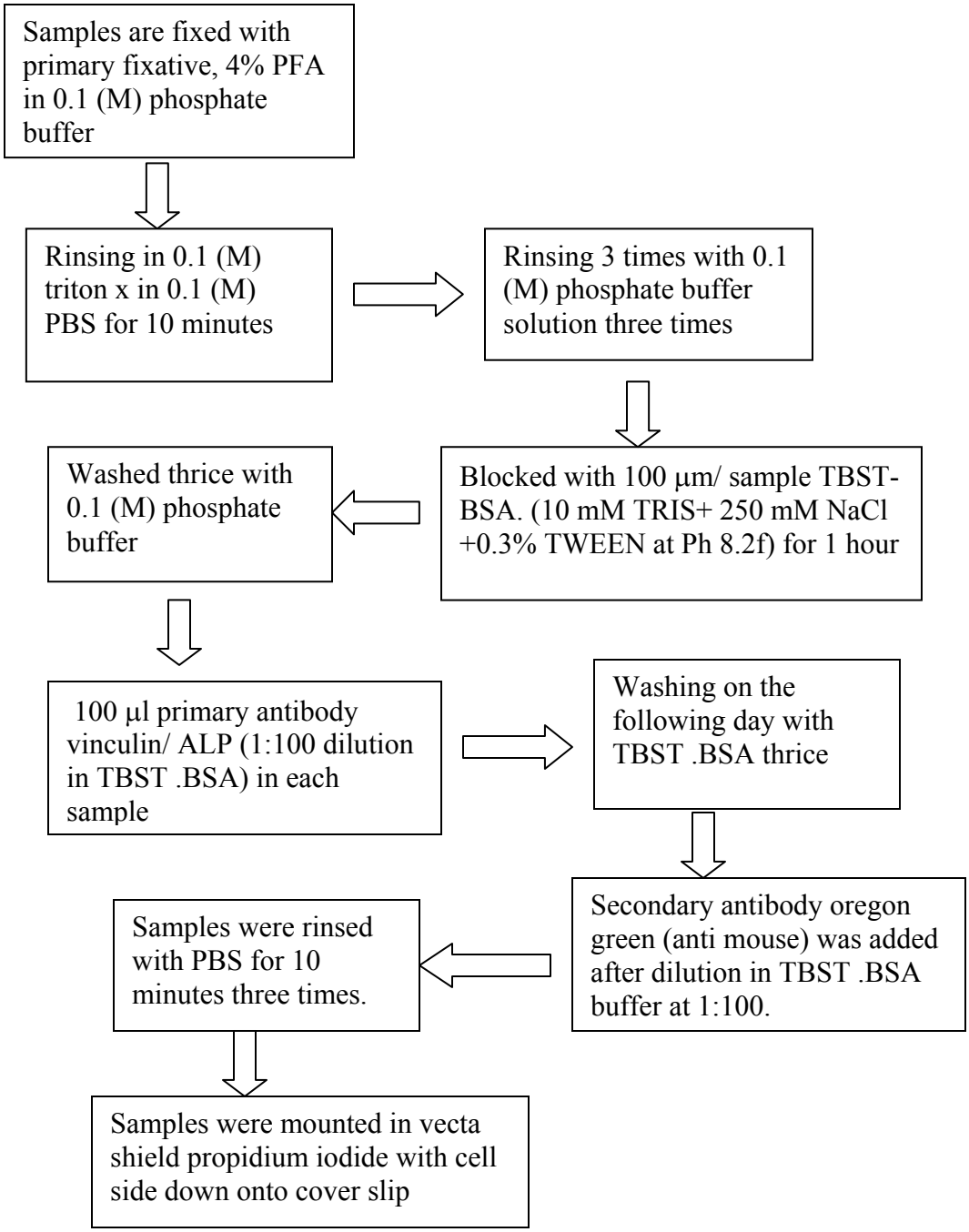

Figure 6.7. Protocol of vinculin and ALP expression study on sample surface

6.3.2. Results

6.3.2.1. Particle size analysis of calcined HA particles

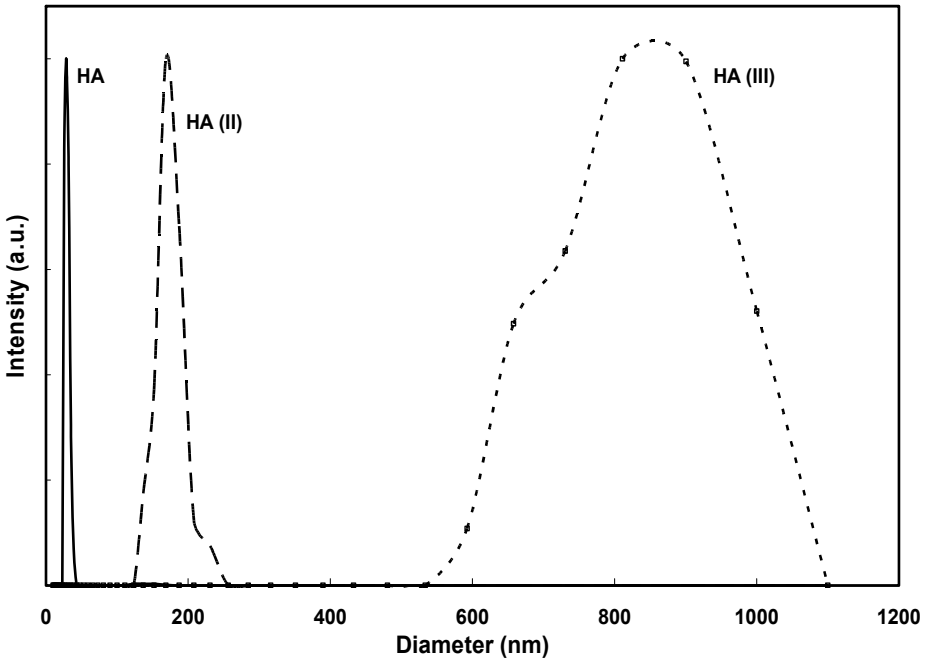

Figure 6.8: Particle size distribution of HA (I), HA (II) and HA (III) powders

Figure 6.8 shows the particle size distribution of HA (I), HA (II) and HA (III) powders. The particle size of as synthesized HA (I) nanopowders varied between 30 to 60 nm. After calcination HA (II) powder showed a particle size distribution between 150 to 280 nm, whereas HA (III) powder exhibited much broader particle size distribution between 540 nm to 1.1 μm.

6.3.2.2. Phase and microstructural analysis

X-ray analysis of sintered HA compacts processed from as synthesized and calcined HA powders is shown in **figure 6.9**. All the compacts, HA (I), HA (II) and HA (III), exhibited phase pure HA according to JCPDS 09-0432.

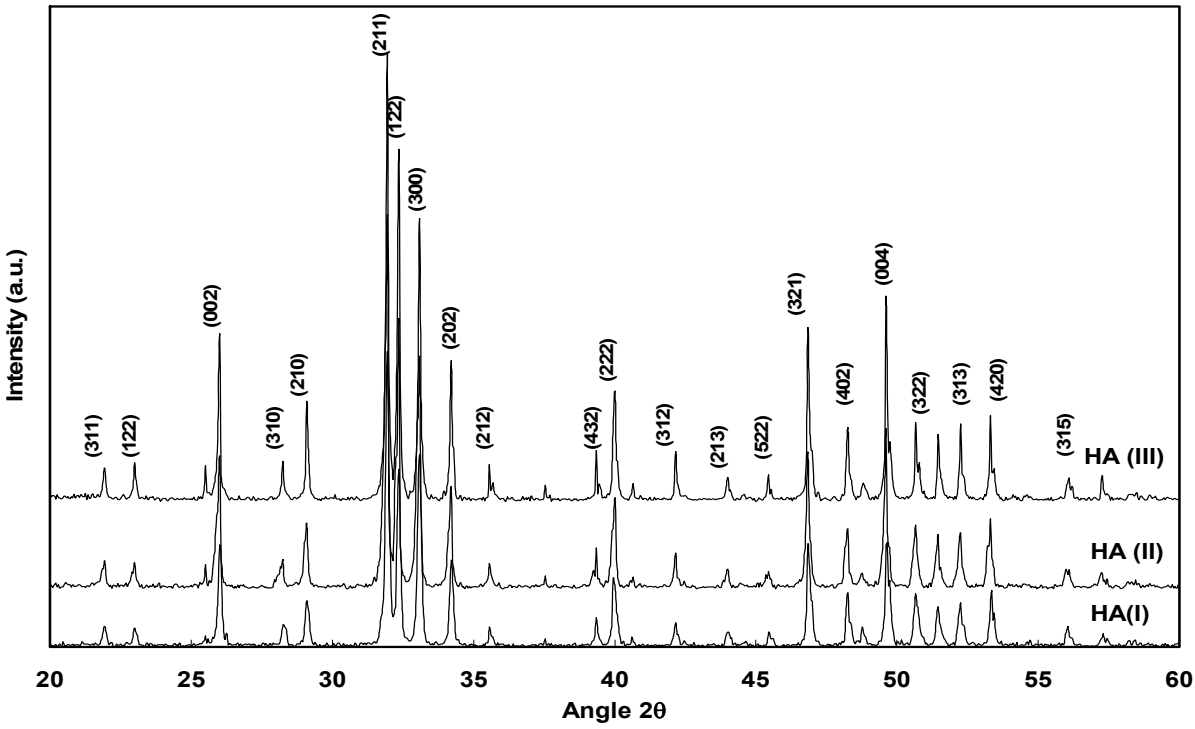

Figure 6.9: X-ray diffraction of sintered HA pellets prepared from as synthesized and calcined HA powders

Scanning electron micrographs of the surfaces of sintered HA compacts are shown in **figures 6.10 a-c**. The average grain size of sintered HA (I), HA (II) and HA (III) compacts were found to be 0.168±0.086, 1.48 ±0.627 and 5.01 ± 1.02 μm respectively.

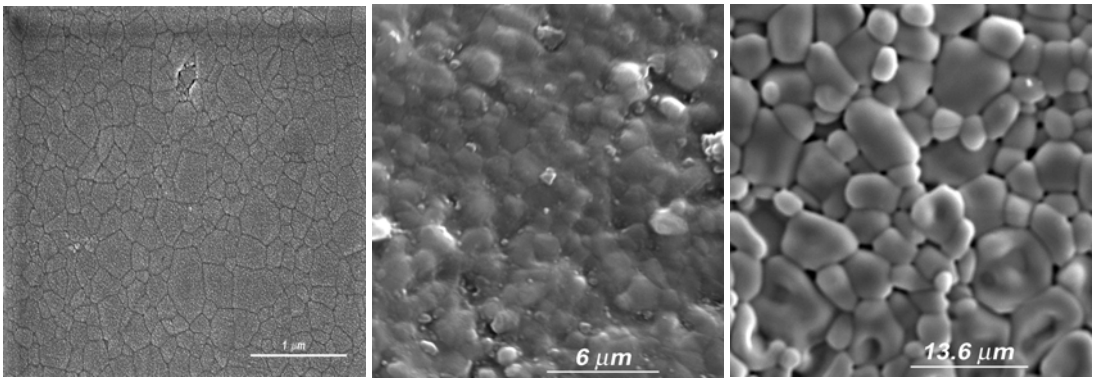

(a) (b) (c)

Figure 6.10. Microstructures of sintered HA compacts prepared from (a) HA (I), (b) HA (II), and (c) HA (III) powders

6.3.2.3. Mechanical characterization

The sintered HA compacts, HA (I), HA (II) and HA (III), were used for the measurement of microhardness, fracture toughness and compressive strength. The variation in compressive strength of HA compacts with change in grain size is depicted in **figure 6.11**. As expected, with increase in grain size the compressive strength of HA compacts were decreased. Thus the lowest grain sized HA compact, i.e. HA (I) showed the highest compressive strength of 395±36 MPa, whereas only 88± 29 MPa of compressive strength was observed in HA (III) that possessed the highest grain size among the three HA compacts. **Figure 6.12** shows the variation in Young's modulus of HA compacts with change in grain size. HA (I) compact having the lowest grain size showed the highest Young's modulus of 127 MPa, which was higher than Young's modulus of HA (II) (117 MPa) and HA (III) (103 MPa).

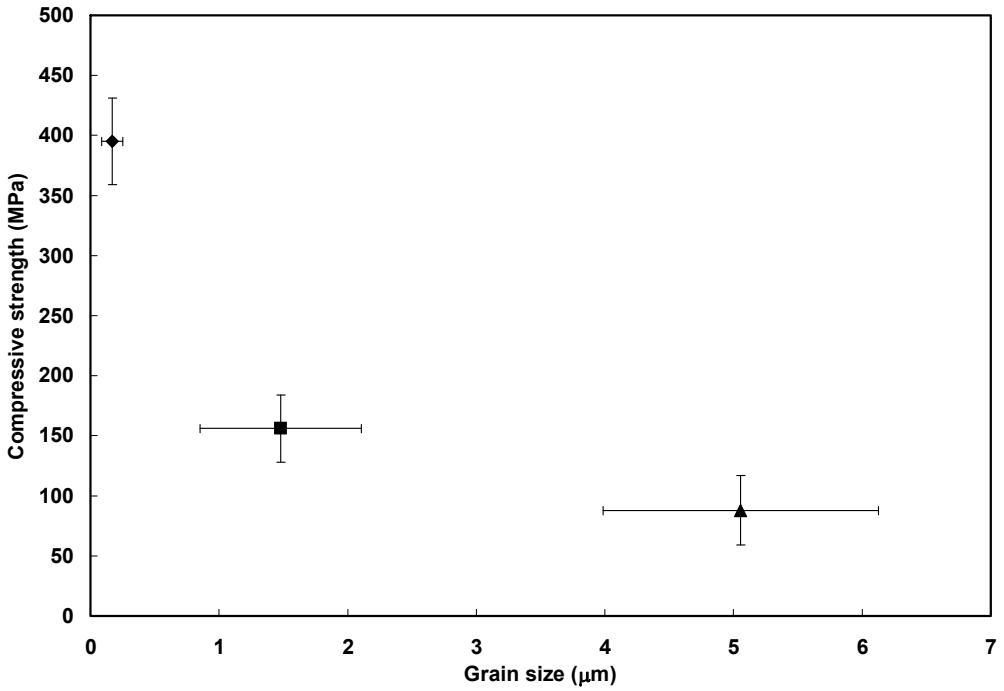

Figure 6.11: Compressive strength of HA (I), HA (II) and HA (III) compacts

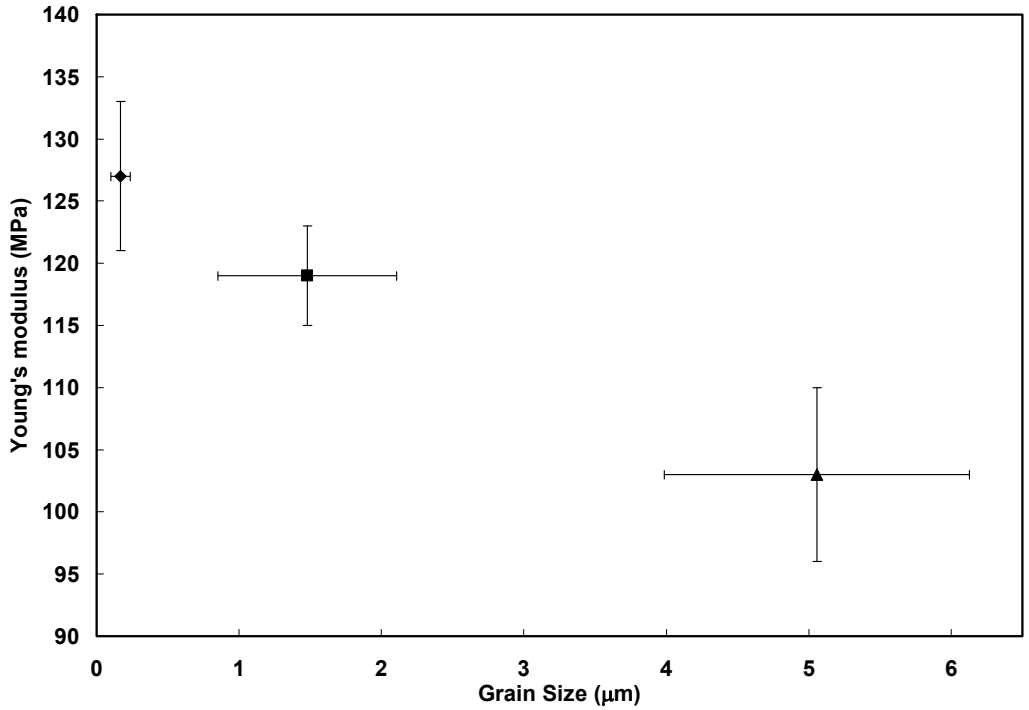

Figure 6.12: Young's modulus values of HA (I), HA (II) and HA (III) compacts

Figures 6.13a, b show the effects of grain size on microhardness and indentation fracture toughness of sintered HA compacts. It was observed that with decrease in grain size, both microhardness and fracture toughness of HA compacts were increased. HA (I) compact with an average grain size of 0.168±0.86 μm showed the highest hardness of 8.4±0.4 GPa and fracture toughness of 1.9 ±0.1 $MPam^{1/2}$. The hardness (3.8 ±0.42 GPa) and fracture toughness of (0.8 ±0.07 $MPam^{1/2}$) were the lowest for HA (III) with a grain size of 5.1±1.07 μm. SEM micrographs of some of the indents made at a load of 500 g on HA(I) and HA (III) compacts are shown in **figure 6.14**. It is clear that the size of indentation as well as radial crack length were smaller on HA (I) compact compared to that on HA (III) compact.

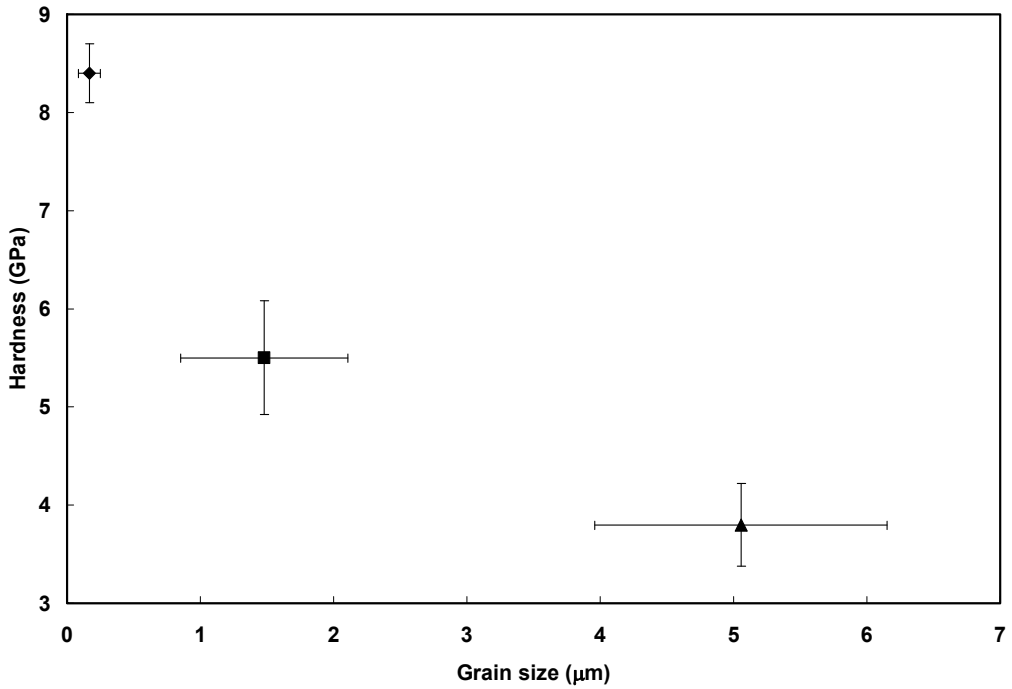

(a)

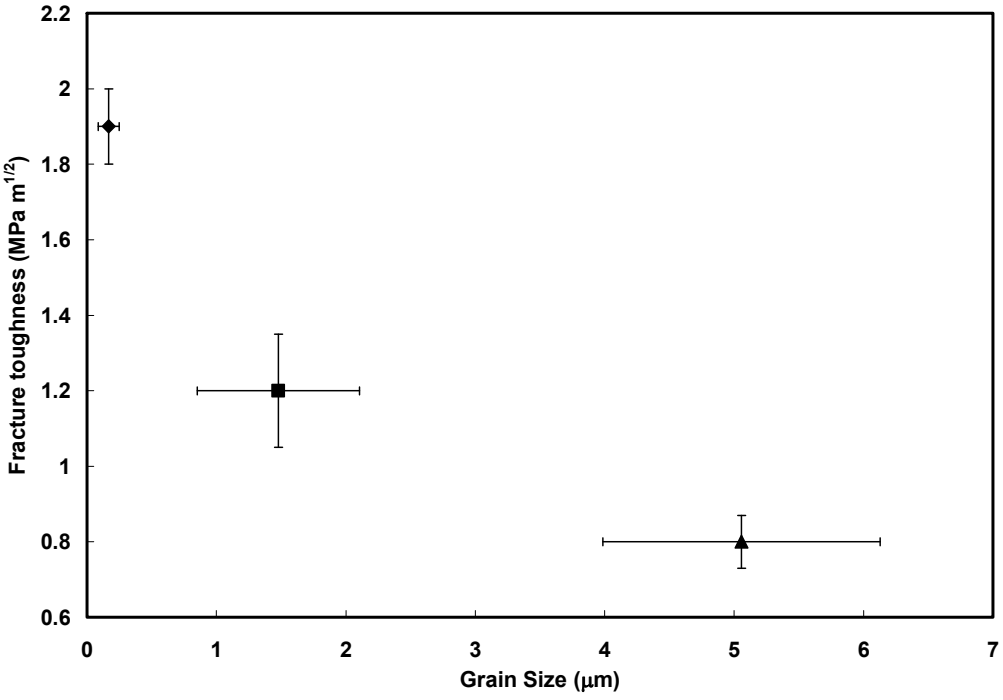

(b)

Figure 6.13: Variation in (a) microhardness (b) fracture toughness of sintered HA (I), HA (II) and HA (III) compacts

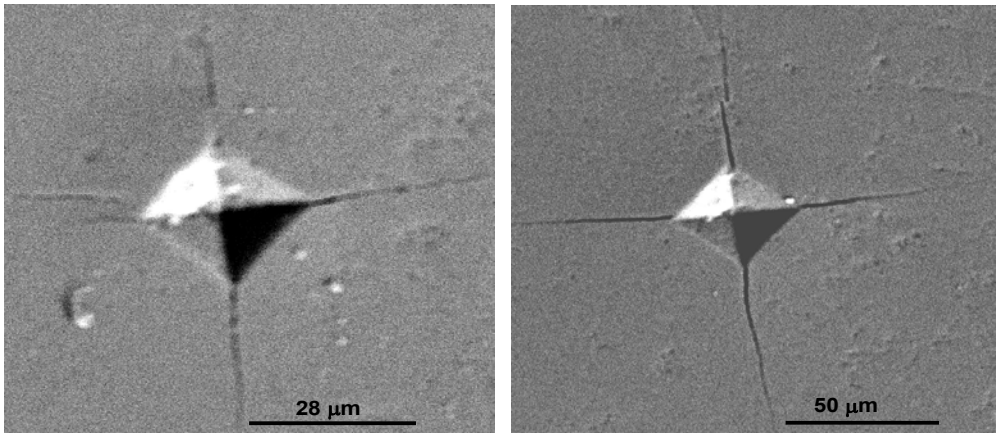

(a) **(b)**

Figure 6.14. Back scattered micrographs of indentations done on (a) HA (I) and (b) HA (II) compacts, at a load of 500 g

6.3.2.4. Surface properties

To determine the surface properties of HA (I), HA (II) and HA (III) compacts, contact angles of different liquid in contact with HA surfaces were evaluated. The angle of contact between a liquid and a surface is known as contact angle. When a drop of liquid is placed on a surface, it will spread to reach equilibrium, when the sum of the interfacial tensions in the plane of the surface is zero. **Figure 6.15(a, b)** show the values of contact angles measured using cell media and water on HA (I), HA (II) and HA (III) surfaces. It was noticed that contact angle changed significantly depending on grain size of HA compacts. With decrease in grain size in HA compacts contact angle values of both distilled water and cell media were decreased. Both water and cell media droplets on HA (I) surface showed the lowest contact angles whereas the highest contact angles were observed HA (III) surface. Irrespective of the grain size of HA compacts the contact angle values of water droplets were always higher compared that of cell media droplets. With the help of contact angle surface energies for all the HA compacts were calculated using **equation 6.2** in experimental section 6.3.1**.3 A (b).** To calculate surface energy, three different liquids namely water, glycerol, and formamide were used. Surface energy, defined

as the increased free energy per unit area for creating a new surface, is directly related to the tendency of molecules to be adsorbed on the surface. Calculations for surface energy from contact angles of three liquids were shown in **table 6.8**. Surface energy of HA surface found to increase with decrease of grain size on HA surface. HA (I) surface having the lowest grain size showed the maximum surface energy of 88.7±1.62 mJ/m^2, whereas the highest grain sized HA surface i.e. HA (III) surface exhibited a surface energy 72.89±1.55 mJ/m^2. HA (II) surface showed an intermediate value of surface energy, which is 79.54±2.36 mJ/m^2.

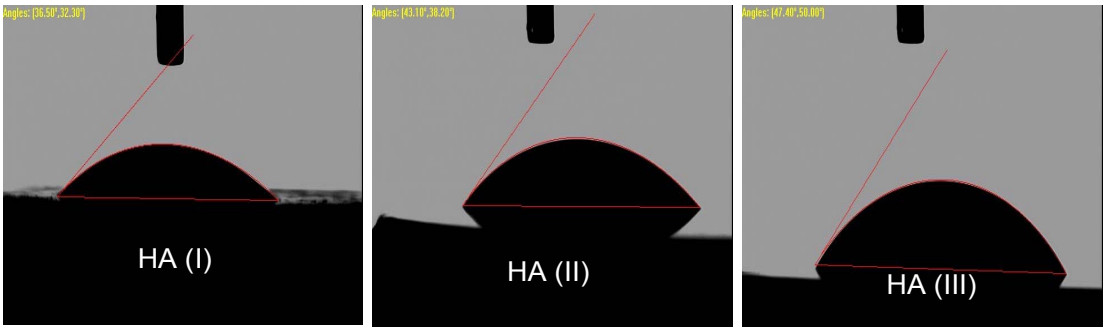

(a)

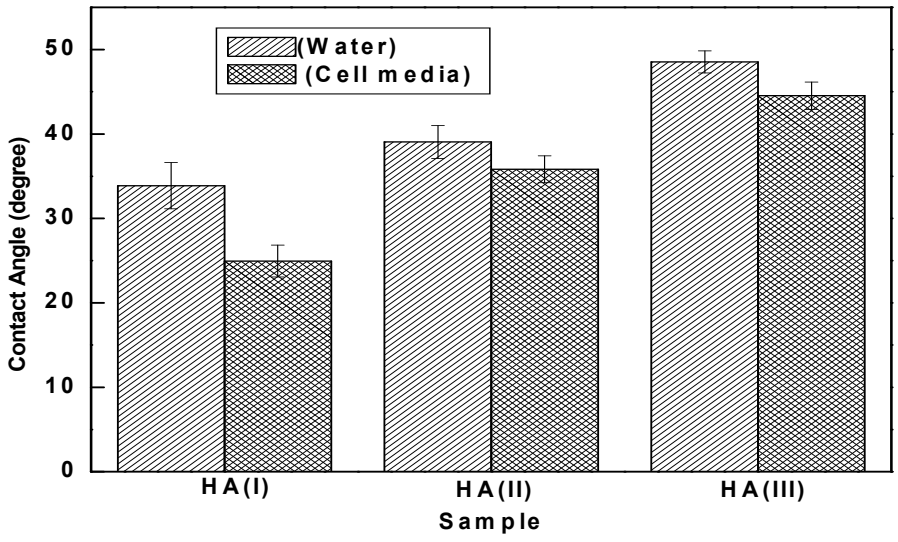

(b)

Figure 6.15: Variation in contact angle liquids on the surfaces of HA (I), HA (II) and HA (III) compacts (a) photographs of water droplets in contact with HA surface and (b) plot of contact angles of water and cell media on different grain sized HA surface

Table 6.8 Surface energy of HA compacts with different grain size

Samples	Contact Angles (degrees)			Surface energy (mJ/m^2)
	Formamide	Glycerol	Water	
HA (I)	29.18±2.07	40.55±3.93	34.95±2.38	97.3±4.28
HA (II)	35.81±2.58	44.53±1.92	39.16±1.84	81.88±3.21
HA(III)	44.43±1.3	52.15±1.23	48.53±1.86	71.92±1.82

6.3.2.5 *In vitro* cell-material interaction

Osteoblast cell attachments, spreading and proliferation on HA surfaces were analyzed for cell-materials interactions using a scanning electron microscope.

A. Cell morphology

Osteoblast cells on HA surfaces were analyzed for cell shape and cell-material interactions using SEM. **Figures 6.16a-c** show SEM morphologies of osteoblast cells on HA (I) ,HA (II) and HA (III) surfaces. Osteoblast cells attached well on all the HA samples. However,

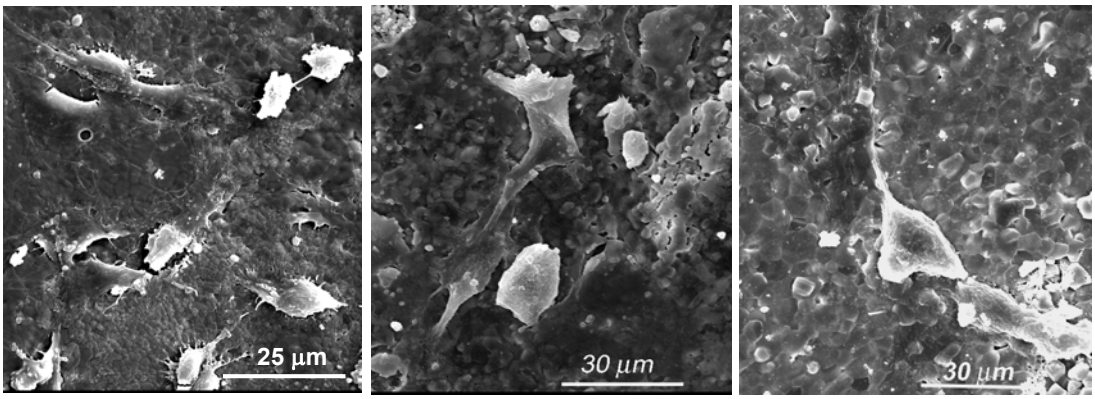

(a) (b) (c)

Figure 6.16: SEM micrographs of osteoblast cells after 1 day of culture on (a) HA (I), (b) HA (II), and (c) HA (III) compacts

when compared with HA (II) and HA (III), more number of cells were observed on HA (I). Osteoblast cells cultured on HA (I) exhibited more number of lamellipodia and filopodia extensions as shown in **figure 6.16a**, for attachment with substrate as well as with neighboring cells. Cells on HA (II) and HA (III) exhibited an elongated, flattened morphology, as shown in

figure **6.16b, c**. Fewer filopodia between cells and HA (II), HA (III) were evident when compared with that between cells and HA (I). High magnification microstructure imaging in figure **6.17** shows the spreading of filamentous microextensions from osteoblast cells onto the nanograins of HA (I) surface. HA (I) compact having higher number of grain boundaries provided greater number of adhesion sites for filopodia extensions.

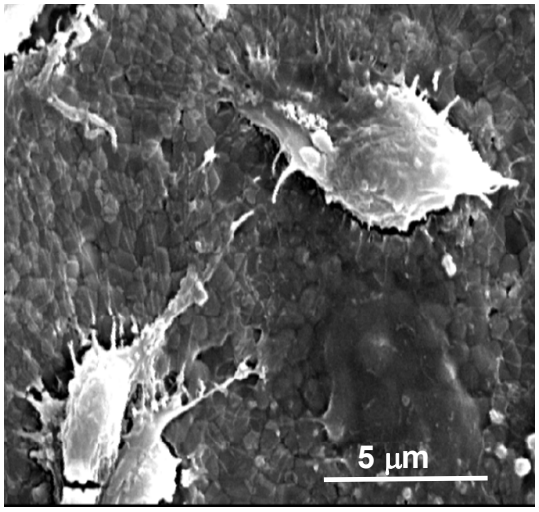

Figure 6.17: Human bone cell study after 1 day of cell culture on nanostructured HA [HA (I)] compact. Filopodia extensions from cells used the grain boundaries on nano HA compact for better cellular attachment.

After 5 days of culture, cells had undergone a significant spreading on the surfaces of three HA compacts as depicted in figures.**6.18 a-c**. Significant cell proliferation was evident as more number of cells could be observed on all the HA compacts after 5 days of cell culture than that at day 1. Cell spreading on HA (I) surface found to be much greater as compared to that on HA (II) and HA (III) surfaces. Cells on HA (I) surface started to grow to confluence. In general, fewer cells grew on the surfaces of HA (II) and HA (III) when compared to that of HA (I). Again HA (II) surface encouraged higher cell spreading as compared to HA (III) surface.

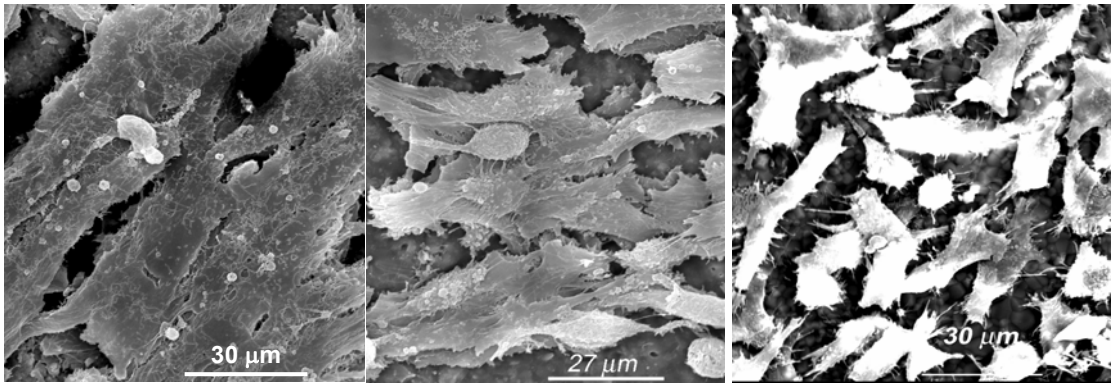

(a) (b) (c)

Figure 6.18: SEM micrographs of osteoblast cells after 5 days of culture on (a) HA (I), (b) HA (II), and (c) HA (III) compacts

SEM images of osteoblast cells cultured for 11 days are presented in figures **6.19 a-c**. The surfaces of HA was completely covered by a dense and confluent cellular multilayer forming a three-dimensional fibril network. The presence of ECM could be detected on the surface of cells. **Figure 6.14a** shows higher number of cell banding on HA (I) surface as compared to HA (II) and HA (III) surfaces in figures **6.14b, c**.

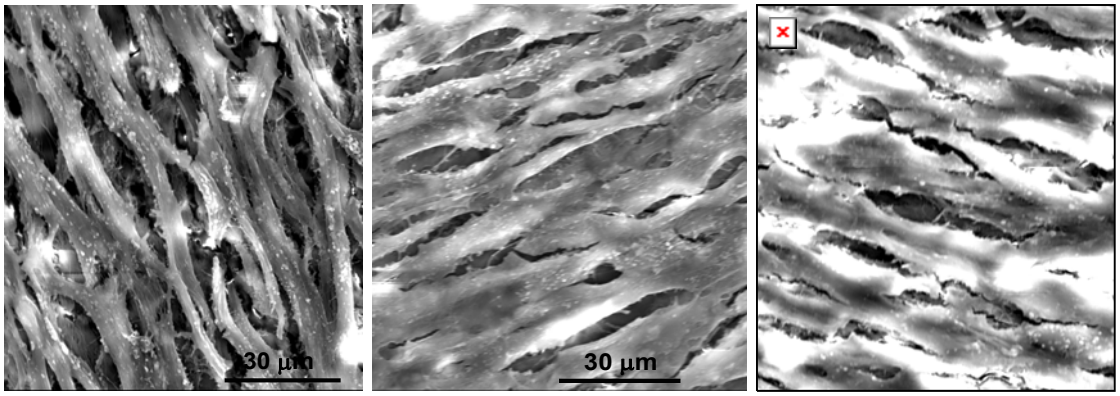

(a) (b) (c)

Figure 6.19: SEM micrographs of osteoblast cells after 11 days of culture on (a) HA (I), (b) HA (II), and (c) HA (III) compacts.

B. MTT Assay

MTT assay was used to determine osteoblast cell proliferation on HA compacts. **Figure 6.20** shows a comparison of cell densities on three HA compacts over the course of the

experiment. Cell proliferation was evident over the duration of the experiment, on all the HA compacts. Cell densities were significantly higher on HA (I) compact as compared to HA (II) and HA (III) at all time points. Again cell proliferation on HA (II) compact found to be greater compared to that on HA (III) compact.

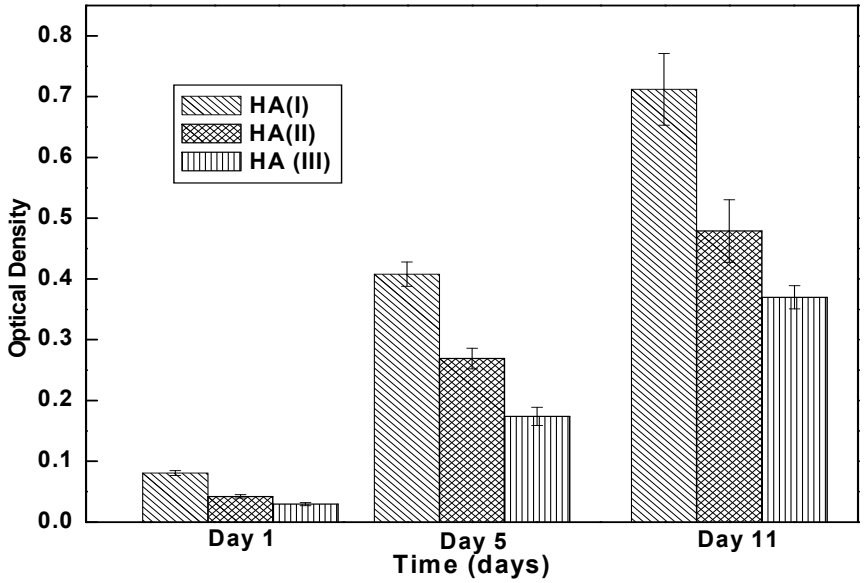

Figure 6.20. MTT assay of cells on HA (I), HA (II) and HA (III) compacts

C. Immunocytochemistry and confocal microscopy

(a) Vinculin expression

The formation of focal adhesion plaques is a prerequisite process for the development of the signaling transduction in cell attachment, and is one of the important indicators for cell activity on the substrates. Vinculin aids in the assemblage of focal contacts by cross-linking and recruiting other proteins to form adhesive plaques.[286] Vinculin also acts as an adhesion molecule between the cells and substratum. It is mostly located at points of focal adhesion plaque, so the existing of vinculin represents the formation of focal adhesion plaque. As cells attach to one another and to the substratum, adhesive proteins interact with and form bonds to adhesion

receptors within the cellular membrane. Antibody bound to vinculin expressed green fluorescence and nuclei stained with propidium iodide (PI) in the mounting medium expressed red fluorescence. The formation of vinculin-positive focal adhesion plaques increased gradually with cell culture time on all three HA compacts as shown in figures **6.21, 6.22** and **6.23**. After one day of cell seeding, the most fluorescence staining of vinculin was observed on HA (I) substrate as in figure **6.21a**, compared to that on HA (II) and HA (III) substrates. Again HA (II) compact showed higher degree of vinculin expression as in figure **6.21b** compared HA (III) compact in figure **6.21c**.

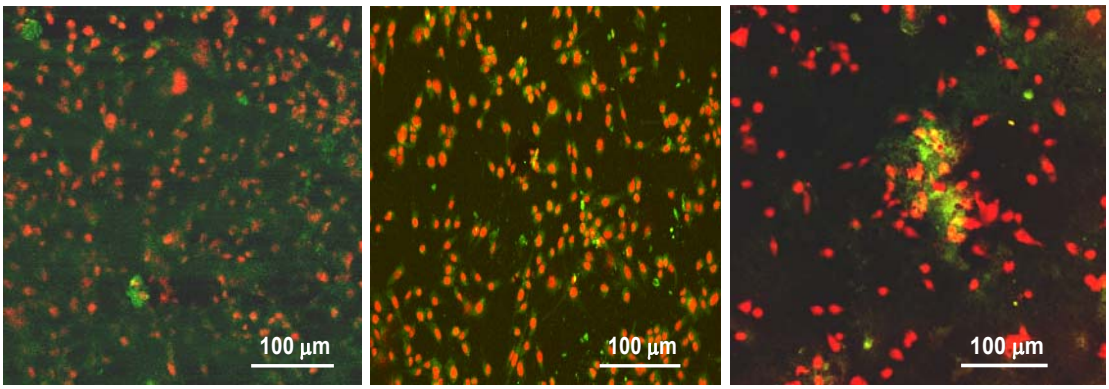

(a) (b) (c)

Figure 6.21: Confocal micrographs of vinculin expression in osteoblast cells cultured on (a) HA (I), (b) HA (II), (c) HA (III) after day1.

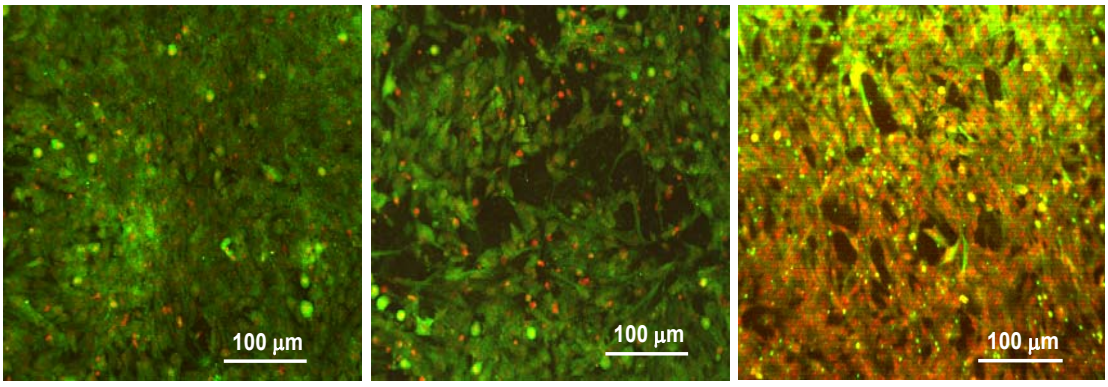

(a) (b) (c)

Figure 6.22. Confocal micrographs of vinculin expression in osteoblast cells cultured on (a) HA (I), (b) HA (II), (c) HA (III) after day 5.

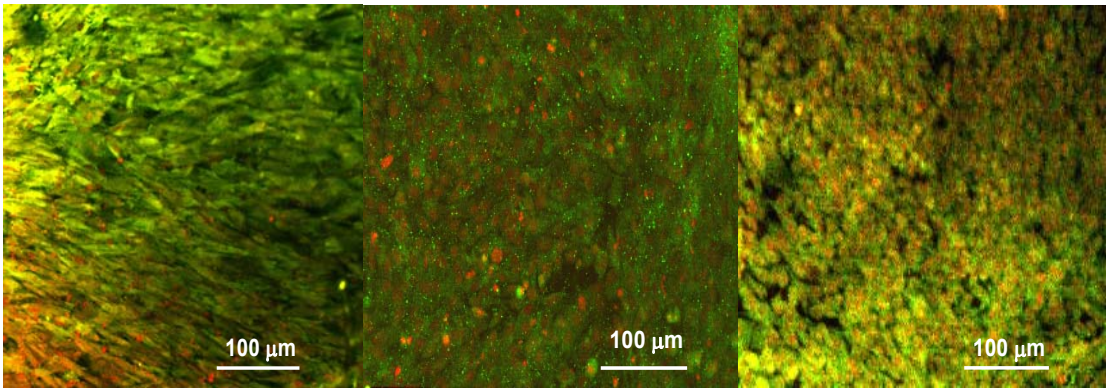

(a) (b) (c)

Figure 6.23. Confocal micrographs of vinculin expression in osteoblast cells cultured on (a) HA (I), (b) HA (II), (c) HA (III) after day 11. Green fluorescence indicating antibody bound to ALP, red fluorescence indicating antibody bound to DNA (nucleus).

Vinculin staining on HA (I) was also more than that on HA (II) and HA (III) at 5 days as in **figure 6.22** and 11 days as in **figure 6.23**. Compared with HA (III) substrate, the vinculin staining on HA (II) substrate was more intense at all day points of cell culture experiment.

(b) Alkaline Phosphatase expression

Immunocytochemistry of osteoblast cells was used to determine whether the cells express an osteoblastic phenotype on samples or not. A major characteristic of osteoblasts is the expression of alkaline phosphatase (ALP). Antibody bound to ALP expressed green fluorescence and nuclei stained with propidium iodide (PI) in the mounting medium expressed red fluorescence. **Figures 6.24a-c** show confocal micrographs of ALP expression in one day cultured osteoblast cells on HA (I), HA (II) and HA (III) substrates. No positive immunostaining for ALP was detected on any substrate after day 1. After day 5, osteoblast cells cultured on HA

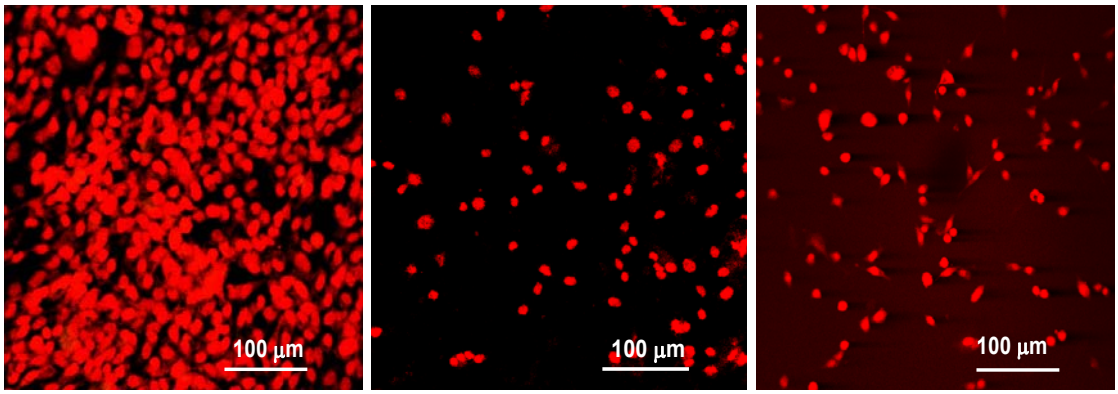

(a) (b) (c)

Figure 6.24. Confocal micrographs of ALP expression in osteoblast cells cultured on (a) HA (I), (b) HA (II), (c) HA (III) after day1.

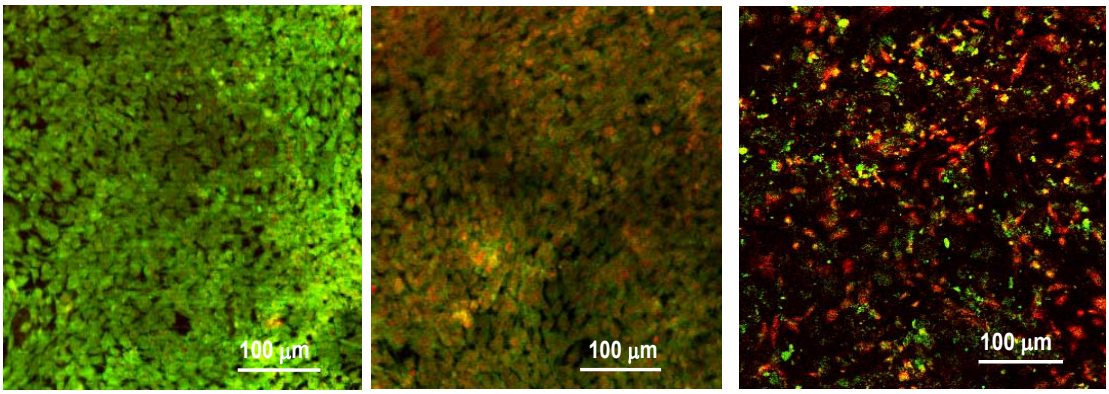

(a) (b) (c)

Figure 6.25. Confocal micrographs of ALP expression in osteoblast cells cultured on (a) HA (I), (b) HA (II), (c) HA (III) after day 5

substrates displayed positive signal for ALP, but with different patterns and levels as depicted in **figure 6.25a-c**. After 5 days of culture, cells on HA (I) showed stronger green fluorescence for ALP followed by HA (II) and HA (III). With the increase in culture time, ALP activity increased significantly on all the HA compacts. After 11 days of cell culture, ALP expression on HA (I) as shown in figure **6.26a**, was more intense compared to that observed on HA (II) in **figure 6.26b**, and HA (III) in **figure 6.26c**. Again HA (II) compact exhibited stronger green fluorescence staining for ALP compared to HA (III) compact after 11 days of cell culture.

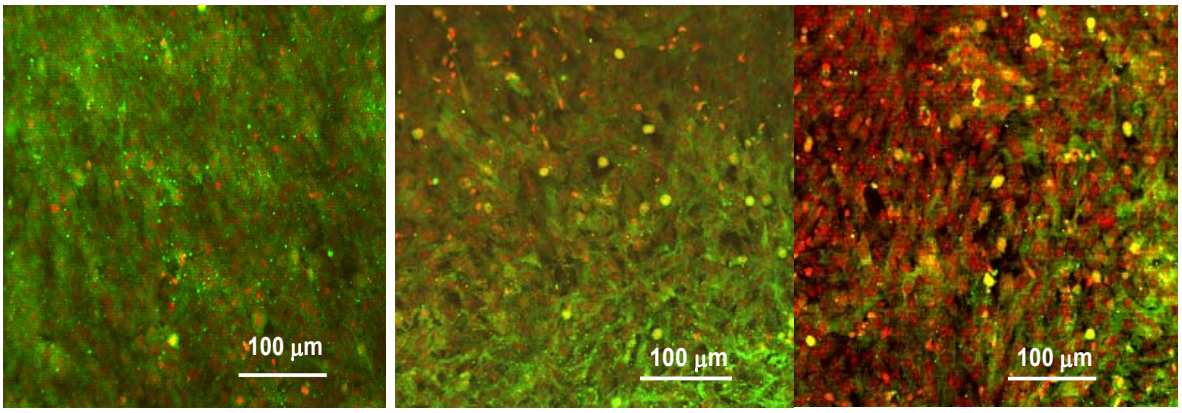

(a) (b) (c)

Figure 6.26. Confocal micrographs of ALP expression in osteoblast cells cultured on (a) HA (I), (b) HA (II), (c) HA (III) after day11. Green fluorescence indicating antibody bound to ALP, red fluorescence indicating antibody bound to DNA (nucleus).

Table 6.9. Summary of mechanical, surface and bioactive properties of HA (I), HA (II) and HA (III) compacts

Sample	Grain size (μm)	Mechanical properties			Surface energy (mJ/m^2)	*In vitro* cell –material interaction
		Compressive strength (MPa)	Hardness (GPa)	Fracture toughness ($MPam^{1/2}$		
HA-I)	0.168 ±0.086	395±36	8.4±0.4	1.9±0.1	97.30 ± 4.28	Promoted faster osteobalast cell attachment, spreading, proliferation and differentiation than HA (II) and HA (III)
HA-II	1.48 ±0.627	156 ±28	5.5±0.58	1.2±0.15	81.88 ± 3.21	Showed higher bioactivity compared to HA (III)
HA-III	5.1 ±1.07	88±29	3.8±0.42	0.8 ±0.07	71.92 ± 1.82	Showed the lowest bioactivity

6.3.3. Discussion

The final grain size in sintered ceramic compact depends on starting particle size and surface area of powders, sintering temperature and time of green ceramic compact. All other factors being constant, higher the particle size in green compact, higher will be the grains size in sintered compact. HA powders calcined at higher temperature for longer amount of time

possessed particles of higher size compared to powders calcined at lower temperature for shorter duration. Thus HA (III) green compact was composed of the biggest sized HA particles among all the HA compacts. Again, green HA (III) compact was sintered in microwave furnace for longer time compared to HA (II) compact, which resulted in higher grain growth in the sintered HA (III) microstructure. HA (I) green compacts were composed of particles of the highest surface area, which resulted in the highest driving force for sintering. That is why, HA (I) green compact could be sintered at lower temperature with no or minimum grain growth in sintered microstructure.

For HA compacts with identical densities, mechanical properties such as compressive strength, hardness and fracture toughness, are enhanced with decrease in grain size in sintered microstructure. With decrease in grain size, the inherent flaw size in sintered microstructure is reduced which leads to the enhancement of compressive strength. Again as the number of grain boundaries per unit volume is increased with decrease in grain size, lower grain sized compacts offer more resistance to crack propagation resulting in higher hardness and fracture toughness. Thus HA (I) nanocompacts having the lowest grain size showed the maximum compressive strength, hardness and fracture toughness than HA (II) and HA (III) compacts.

Surface energy of HA compact increased with decrease in grain size. Again with decrease in grain size in sintered HA compact the surface became increasingly hydrophilic which was reflected in the lowest contact angle values of polar liquids, such as, water and cell media, in contact with nanograined HA (I)compacts. As the surface became increasingly hydrophilic, wettability increased which favored cell spreading.

The most critical stage of osteoblast cell –material interaction is adhesion and spreading which ultimately governs cell's capacity to proliferate and differentiate. The MTT result showed

that, at all day points of cell culture, the number of cells on HA (I) compact was significantly higher than those on HA (II) and HA (III). This result suggests that nano grained HA compact enhanced cellular attachment. In support of this claim, it was observed that after 1 day of cell culture filopodia extensions from the cells to the substrate were more abundant on HA (I) than on HA (II) and HA (III). In addition to communication between cells, external physical features such as filopodia and microextensions are also used in attachment and migration. Surface energy directly influences two important phenomena for an efficient cell-biomaterial interaction, namely protein adsorption and cell attachment. After immersion in biological fluids, all implant materials are coated by a protein layer. The presence of this pre-adsorbed protein layer is essential in mediating cell response to the material. For HA ceramics, protein adsorption is governed by electrostatic interaction between Ca^{2+} and COO^{-} of protein, PO_4^{3-} and NH_3^{+} of proteins. With decrease in grain size of HA compact the number of sites for electrostatic interaction between HA and protein increased. Thus protein adsorption and subsequent cell attachment was the highest on nanograined HA (I) compact, followed by HA (II) and HA (III) compact. This fact was further endorsed by the results from vinculin protein expression on cell cultured HA (I), HA (II) and HA (III) surfaces. HA (I) compact showed the strongest vinculin expression all through the cell culture experiment, signifies HA (I) surface generated most number of focal points for cell adhesion. It was also observed that decrease in grain size on HA surface creates more number of focal points for cell adhesion , the fact was well reflected in higher amount of vinculin expression on HA (II) compact compared to that on HA (III) compact. Again after 5 days of culture, SEM micrographs show that cell spreading on nanograined HA (I) compact was the highest followed by HA (II) and HA (III) compacts, which was due to higher wettability of lower grained HA compacts. Thus surface of HA (I) compacts being conducive for both cell

attachment and spreading encouraged cell proliferation most efficiently compared to HA (II) and HA (III) compacts. Higher degree of cell proliferation on HA (II) surface as compared to HA (III) surface was due to higher amount of cell attachment and spreading on former.

As osteoblast cells proliferate and then differentiate, it expresses a number of osteoblastic phenotypic markers. ALP is a major characteristic marker of osteoblasts. ALP is regarded as an early marker for osteoblast differentiation, and it is generally accepted that as the specific activity of ALP in a population of bone cells increases there is a corresponding shift to a more differentiated state. Though after 1 day no green fluorescence from ALP was observed from any of the HA compacts, after 5 days abundant amount of ALP protein expression was found on HA (I) surface. Both on 5 and 11 days ALP expression was far more intense on HA (I) compact as compared to HA (II) and HA (III) compacts. Higher levels of ALP expression on HA (I) could be related to faster differentiation of osteoblast cells on HA (I) surface. Thus nanograined HA (I) compacts facilitated rapid differentiation and strong adhesion of osteoblast cells. Again HA (II) compact showed stronger ALP expression than HA (III) compact at 5 and 11 days. These facts suggest that differentiation of osteoblast cells become faster as the grain size of HA compact decreased. Though results from vinculin expression was not conclusive to differentiate cellular attachment behavior on different grained HA compacts, ALP study found to be conclusive in distinguishing rate of osteoblast differentiation on different grained HA compacts. In general, osteoblast cells attach, adhere, spread, proliferate and then differentiate faster as the grain size of HA compact decreased.

6.4. *In vitro* biocompatibility evaluation of TCP compacts

6.4.1. Experimental

6.4.1.1. Processing of TCP compacts

The synthesized β-TCP nanopowders (as described in section 4.2.3) were consolidated in the form of discs by uniaxial pressing at 50 MPa followed by cold isostatic pressing at 345 MPa. The consolidated β-TCP discs were then sintered in microwave furnace at 1250 ^{o}C for 20 minutes.

6.4.1.2. Characterization of TCP compacts

Bulk density of sintered TCP compact was evaluated by measuring weight and dimensions of sintered TCP compacts. X- ray diffraction of sintered disc was used to study phase composition in sintered structure. The sintered TCP compacts were sterilized in autoclave at 121 ^{o}C for 30 minutes. An immortalized, cloned osteoblastic precursor cell line 1 (OPC1), which was derived from human fetal bone tissue, was purchased from OSHU (Portland, OR, USA) and used as a source cell to study *in vitro* cell –material interaction on sterilized TCP compact using SEM, MTT assay, and confocal microscopy as described in section 6.3.1.3.2**.**

6.4.2. Results

6.4.2.1. Phase analysis

Bulk density of sintered TCP discs varied from 2.68 to 2.80 g/cc. The XRD pattern of the sintered sample showed the formation of significant amount of α-TCP phase as shown in **figure 6.27.**

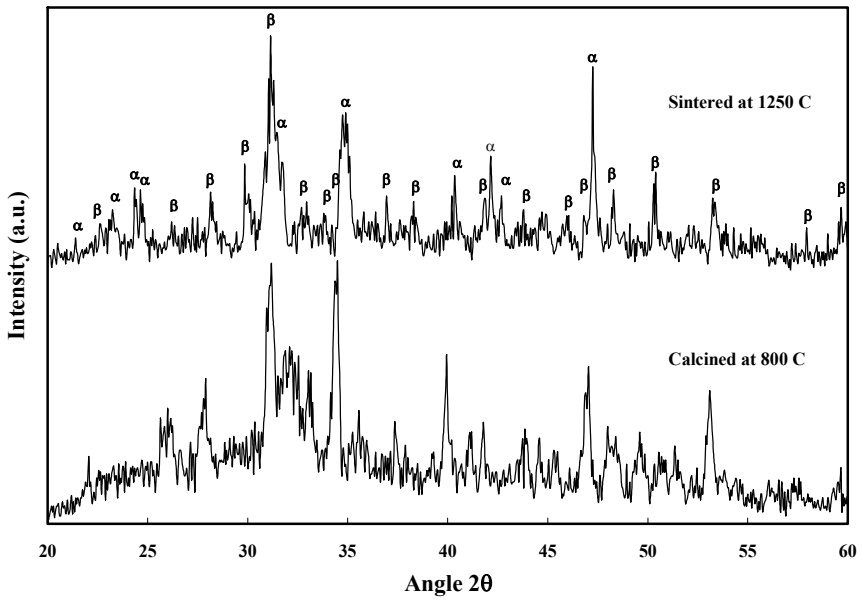

Figure 6.27: XRD pattern of samples calcined at 800 C/3h and sintered at 1250 C/20 min in microwave furnace

6.4.2.2. Study of cell morphology using SEM

Figures 6.28 a, b and **c** illustrate SEM observations of bone cell-material interactions after 1, 5 and 11 days respectively using human osteoprecursor cell line (OPC1). **Figure 6.28a** shows cell attachment through small micro extension onto the sintered body surface after 1 day of OPC1 cell culture. After day 5, cells on material surface were found to proliferate or grow as shown in **figure 6.28b**. After day 11, the cells displayed numerous lamellipodia and filopodia extensions to attach onto the substrate covering the sample surface and to the neighboring cells, as shown in **figure 6.28c**.

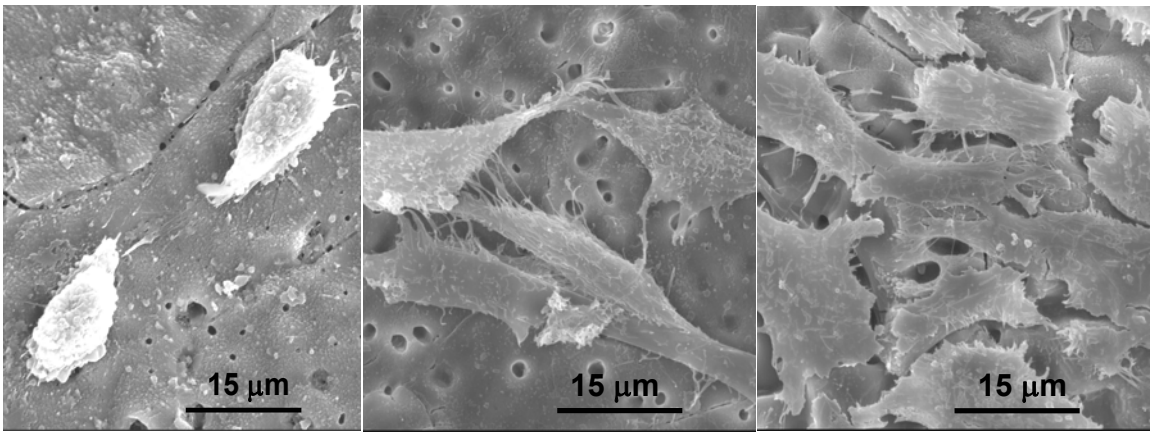

(a) (b) (c)

Figure 6.28: Scanning electron micrographs of OPC1 cells on tricalcium phosphate (TCP) after: (a) 1 day, (b) 5 days and (c) 11 days of cell culture

6.4.2.3. MTT Assay

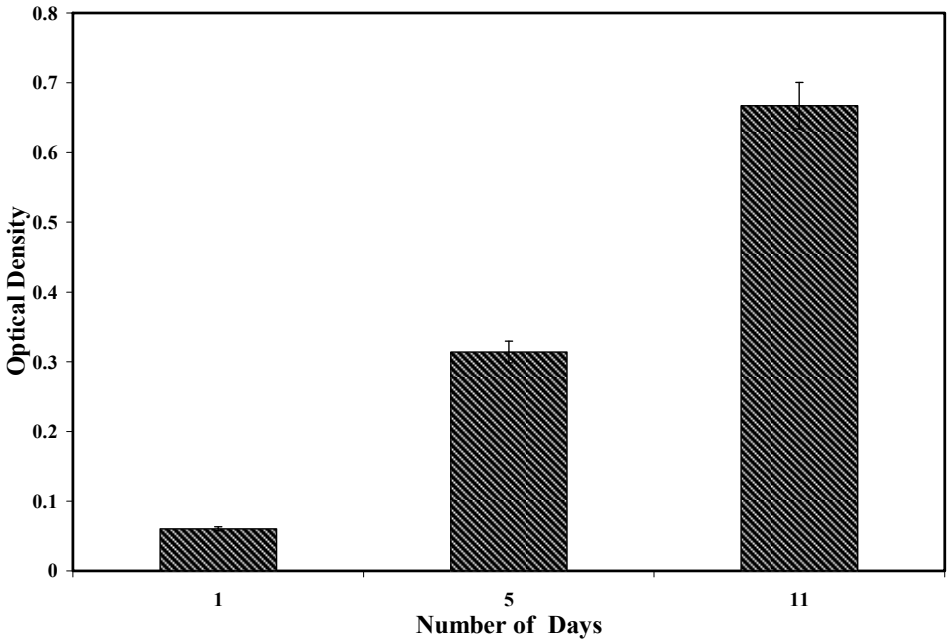

Figure 6.29: MTT assays on TCP discs after 1, 5 and 11 days of cell culture

MTT assay was used to determine OPC1 cell proliferation on coatings. **Figure 6.29** shows a comparison of cell densities on TCP substrate over the course of the experiment. Cell

proliferation was evident over the duration of the experiment. After 11 days of culture, the number of cells on TCP substrate increased approximately 10 times in relation to day 1.

6.4.2.4. Immunocytochemistry and confocal microscopy

Immunocytochemistry of OPC1 cells was used to determine whether the cells express an osteoblastic phenotype on β-TCP samples or not. A major characteristic of osteoblasts is the expression of alkaline phosphatase (ALP). **Figure 6.30** shows confocal micrographs of ALP expression in OPC1 cells cultured on TCP substrate. ALP within the cells is identified by the expression of green fluorescence and nuclei counterstained with PI in the mounting medium expressed red fluorescence. After 5 and 11 days, the immunostaining viewed on the confocal microscope identified the presence of ALP expected. Though after 5 days the cells exhibited little amount of ALP expression, with increase in culture time upto 11 days ALP activity increased significantly.

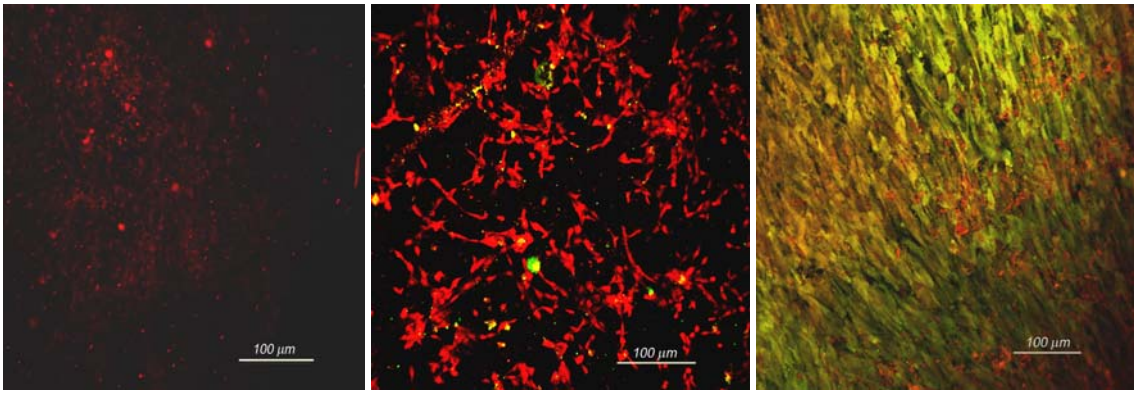

(a) (b) (c)

Figure 6.30. Confocal micrographs of ALP expression in OPC1 cells cultured on TCP discs at (a) day 1, (b) day 5, and (c) at day 11.

6.4.3. Discussion

With progress of cell culture experiment, TCP discs became increasingly porous because of faster dissolution of α-TCP phase in cell culture medium. Up to 11 days of cell culture, the

sintered TCP substrates prepared from the synthesized β-TCP nanopowders exhibited good cell adhesion and spreading to support osteoblast cells attachment, growth and proliferation. In support of this claim, it was observed that filopodia extensions from the cells to the substrate were more abundant on TCP substrates with increase in cell culture time. In addition to communication between cells, external physical features such as filopodia and microextensions are also used in attachment and migration. After 11 days of culture, the cells on TCP substrate grew to confluence.

MTT solution is reduced to give purple color in presence of mitochondrial dehydrogenase in living cells. The absorbance of this colored solution can be quantified by measuring at 570 nm by a spectrophotometer. Higher the intensity of purple color higher is the absorbance at that wavelength and vice versa. Therefore this conversion can be directly related to the number of viable cells. More number of cells was observed on TCP substrate with increase in cell culture days as evident from MTT assay. The MTT assay and SEM observation showed that TCP substrates were not cytotoxic, and thus did not inhibit cell proliferation.

Cellular differentiation is defined as a process by which functional changes occur in cells to make them specialized. Though ALP expression was sparse and localized in some cells after 5 days of culture, it appeared strongly positive in 11 days cultured TCP substrate to support differentiation of osteoblastic cells.

6.5. Summary

The objective of this research was to process highly dense nanostructured HA compacts using microwave sintering with improved mechanical properties and bioactivities. The mechanical and biological properties of HA compacts were evaluated with variation in grain size in sintered HA compacts. The study has shown that nanostructured HA compacts exhibit

remarkably different mechanical and biological properties compared to micron grained counterparts. Some of the key conclusions of the research work are as follows.

- Fully dense nanostructured HA compact with average grain size of 168 ±86 nm was obtained after microwave (3 KW) sintering of HA green compact at 1000 C for 20 minutes.
- With variation in microwave sintering temperature and sintering cycle, HA compacts with grain size varying between 168±86 nm to 1.1± 0.128 μm can be produced.
- Nanostructured HA exhibited better compressive strength (395 MPa) and indentation fracture toughness (2.0 MPa $m^{1/2}$) compared to micron size HA.
- By calcining as synthesized HA nanopowders and then sintering green compacts at 1150 ^{o} C for 30 and 45 minutes in microwave furnace, sintered HA compacts with grain size of 1.48±0.627 μm and 5.1±1.07 μm were obtained.
- Surface properties such as contact angle and surface energy changed with variation in grain size in sintered HA compacts. Nanostructured HA compacts found to be highly hydrophilic with the highest surface energy (97.30 ±4.28 mJ /m^2). HA compacts with an average grain size of 1.48±0.627 and 5.1±1.07 μm exhibited surface energy of 81.88 ±3.21 mJ /m^2 and 71.92 ±1.82 mJ /m^2 respectively.
- Cell adhesion, proliferation and differentiation were tested with vinculin molecules, MTT assay and alkaline phosphatase, respectively.
- Nanostructured HA showed higher number of focal contacts for cell adhesion, higher cell density and faster differentiation compared to micron grained counterparts.
- With a decrease in grain size, HA compacts showed enhanced bioactivity and higher mechanical strength.

6.6 Concluding remarks:

Although preliminary investigations show that nanobiomaterials can bring about significant advancement in the fields of orthopedic and dentistry, more detailed investigations are necessary to realize their full potential in clinical use. Substantial research endeavors are required to address the following key challenges and concerns:

- Consistency and reproducibility of processing technologies
- *In vivo* examination to validate the *in vitro* data
- Optimization of structure and properties of nanobiomaterials mimicking natural bone
- Optimization of bioresorption without comprising mechanical properties
- Identifying cell-specific nanobiomaterials
- Understanding molecular mechanisms of cell–nanobiomaterial interactions
- Improving angiogenesis within the nanobiomaterials system
- Assessing the inflammatory response to nanobiomaterials to validate their biosafety

LIST OF PAPERS

This thesis is based on following papers.

1. Sudip Dasgupta, and Susmita Bose. "Reverse Micelle Mediated Synthesis and Characterization of Nanocrystalline Tricalcium Phosphate Powders for Bone graft." Submitted to *Journal of American Ceramic Society* (after major/minor revision).

2. S. Bose, **S. Dasgupta**, W. Xue, and A. Bandopadhayay, "Tricalcium Phosphate Nanoparticles: Osteoblast Response and A Novel Drug Carrier," Proceedings of the 4th International Symposium on Nano Manufacturing, MIT Press, MIT, MA,USA, 2006.

3. Sudip Dasgupta, Amit Bandyopadhyay, Susmita Bose. Nanoscale Calcium Phosphate for Protein Delivery, International Conference & Exposition on Advanced Ceramics & Composites, Daytona Beach, FL, USA, 2008.

Manuscripts Under Preparation

1. **Sudip Dasgupta**, Amit Bandyopadhyay, and Susmita Bose "Calcium Phosphate Nanoparticles for BSA Protein Delivery." To be communicated.

2. **Sudip Dasgupta**, Amit Bandyopadhyay, and Susmita Bose, "Zn and Mg Doped Hydroxyapatite Nanoparticles for Controlled Release of Protein." To be communicated

3**. Sudip Dasgupta**, Amit Bandyopadhyay, and Susmita Bose. "Mechanical Characterization of Microwave Sintered Nanostructured Hydroxyapatite Compact." To be communicated.

4. **Sudip Dasgupta**, Amit Bandyopadhyay, and Susmita Bose."Grain Size Effect on the Bioactivity of Hydroxyapatite Compacts." To be communicated.

ABBREVIATIONS

AAOS= American Academy of Orthopedic Surgeons

API= Active pharmaceutical ingredient

ACP= Amorphous calcium phosphate

ANOVA= One way analysis of variance

NH_4PMA= Ammonium polymethacrylate

BBB= Blood brain barrier

BMP= Bone morphogenetic protein

BSA= Bovine serum albumin

bFGF= Basic fibroblast growth factor

BET= Brunauer, Emmett and Teller

CD= Crohn's disease

CHA= Carbonated apatite

CaP= Calcium Phosphate

CDHA= Calcium deficient hydroxyapatite

CNS= Central Nervous system

CTAB= Cetyltrimethylammonium bromide

DCPD= Dicalcium phosphate hydrate

DPCA= Dicalcium phosphate anhydrous

DSC= Differential scanning calorimetry

DNA= Deoxyribonucleic acid

DLS= Dynamic light scattering

DME= Dulbeco's minimum essential medium

DMEM= Dulbecco's modified eagle's medium

ESD= Electrostatic spray deposition

ECM= Extra cellular matrix

FAD= Food and drug administration

FTIR= Fourier transform infrared spectroscopy

GI= Gastrointestinal tract

HCA= Hydroxycarbonated apatite

HA= Hydroxyapatite

ISO= International organization for standardization

IDB= Inflammatory bowel disease

ICP-OES= Inductively coupled plasma-optical emission spectroscopy

IGF= Insulin like growth factor

JCPDS= Joint Committee on Powder Diffraction Standards

LDH= Layered double hydroxide

MWCNT= Multi walled carbon nanotube

MCP= Monocalcium phosphate

NOF= National Osteoporosis Foundation

OCP= Octacalcium phosphate pentahydrate

OPC1= Osteoprecursor cell line 1

PEG= Polyethylene glycol

PLGA= Poly(lactic acid-co-glycolic acid)

PVC= Polyvinyl chloride

rhBMP= Recombinant human bone morphogenetic protein

ROS= Reactive oxygen species

RF= Radiofrequency

RGD= Arginine- Glycine- Aspartic acid

RES= Reticulo endothelial system

SWCNT= Single walled carbon nanotube

SEM= Scanning electron microscopy

TEM= Transmission electron microscopy

TCP= Tricalcium phosphate

TGF= Transforming growth factor

UHWMPE= Ultra-high-molecular-weight polyethylene

UV= Ultra violet

XRD= X-ray diffraction

BIBLIOGRAPHY

[1]Alliance Annual Report: Occupational Safety and Health Administration and the American Academy of Orthopedic Surgeons (AAOS), August 4, **2004**

[2] National Osteoporosis Foundation (NOF), Annual Report **2003**

[3] Census Releases 2003 U.S. Population Estimates, US Bureau of Census, **2003**

[4] R. Barbucci, *Integrated Biomaterials Science* (New York: Kluwer–Academic/Plenum) **2002,** 189

[5] D. F. G Emery, H. J .Clarke, M. L. Grover, "Stanmore total hip replacement in younger patients: review of a group of patients tinder *50* years of age at operation", *J. Bone Joint Surgery,* **1997,** 79, 240-46

[6] K. Masanori, N. M Hiroko, Takeki Y. Yoshihisa K., T. Kazuo T. Junzo, "Glutaraldehyde cross-linked hydroxyapatite/collagen self-organized nanocomposites**",** *Biomaterials*, **2004**, 25 (1), 63-69

[7] P. I. Branemark, B.O Hansson. , R. Adell, "Osseointegrated implants in the treatment of the edentulous jaw Experience from a 10-year period," *J Plast Reconstr Surg Suppl,* **1977**, 16(1), 231-38

[8] F. Peters, K. Schwarz, M. Epple, "The structure of bone studied with synchrotron X-ray diffraction", *Thermochim Acta,* **2000**, 361-70

[9] Y. Doi, T. Shibutani, Y. Moriwaki, T. Kajimoto, Y. Iwayama. "Sintered carbonate apatites as bioresorbable bone substitutes", *J Biomed Mater Res*, **1998**, 39, 603-10

[10] Y. Doi, H. Iwanaga, T. Shibutani, Y. Morikawa, Y. Iwayama."Osteoclastic responses to various calcium phosphates in cell cultures", *J Biomed Mat Res,* **1999**, 47, 424-33

[11] U. Hasan, D. D'Augusta, J. Golden, J. Li, G. Timony, M. R Riede John Wozney, "Implantation of recombinant human bone morphogenetic proteins with biomaterial carriers: A correlation between protein pharmacokinetics and osteoinduction in the rat ectopic model", *J Biomed Mater Res*. **2000**, 50 (2), 227-38

[12] T. S. Lindholm, T. J. Gao, "Functional carriers of bone morphogenetic protein", *Ann Chir Gynaecol,* "**1993**, 82, 3-12

[13] U. Ripamonti, A. H. Reddi, "Tissue engineering, morphogenesis, and regeneration of the periodontal tissues by bone morphogenetic proteins", *Crit Rev Oral Biol Med*, 1997, 8, 154-63

[14] J. O.Hollinger, K. Leong, *Biomaterials*, **1996,** 17, 187

[15] Dee KC, Pulao DA and Bizios R. *An Introduction to Tissue-Biomaterial Interaction*, Willey Liss, **2002**

[16] L. Hench and J. Wilson, *An Introduction to Bioceramics*, World Scientific, **1993**

[17]. S. Desa, B. Bidanda, P. Bartolo, "Metallic and Ceramic Biomaterials: Current and Future Developments", Springer, **2007**, 1-14

[18.] S.J. Bhat, *Biomaterials*, 2nd edition, Alpha Science, **2005**

[19.] R. M. Nerem, A. Sambanis, "Tissue Engineering: From Biology to Biological Substitutes ", *Tissue Engineering*, 1 (1), Mary Ann Liebert Inc, **1995**

[20] Biomaterials science: *An introduction to Materials in Medicine,* 2 nd Edition, Edited by B.D. Ratner, A.S. Hoffman, F.J. Schoen, J.E. Lemons, Elsevier, **2004.**

[21] F. S. Kaplan, W. C. Hayes, T. M. Keaveny, et al., S. R. Simon, editor. *Orthopedic basic science*. Columbus, OH, American Academy of Orthopedic Surgeons, **1994**, 127

[22.] T. J. Webster, C. Ergun, R.H. Doremus, et al. "Enhanced functions of osteoclast-like cells on nanophase ceramics", *Biomaterials* **2001**, 22, 1327-33

[23.] D.S. W. Benoit, K. S. Anseth, "The effect on osteoblast function of colocalized RGD and PHSRN epitopes on PEG surfaces", *Biomaterials,* 2005, 26, 5209-5220

[24] C. J. Wilson, R. E. Clegg, D. I. Leavesley et al., "Mediation of Biomaterial–Cell Interactions by Adsorbed Proteins: A Review", *Tissue Eng*, **2005** ,11, 1-18

[25] Webster TJ, Schadler LS, Siegel RW, et al. "Mechanisms of enhanced osteoblast adhesion on nanophase alumina involve vitronectin", *Tissue Eng*, **2001,** 7, 291

[26] C. Yao, V. Perla, J. McKenzie Slamovich E B, Webster T J ," Anodized Ti and Ti6AlV possessing nanometer surface features enhance osteoblast adhesion", *J Biomed Nanotechnol*, **2005**,27(1), 68 -73

[27] P. Ducheyne, P. Bianco, S. Radin et al. , P. Ducheyne, T. Kokubo, C. A. VanBlitterswijk, editors, *Bone-bonding biomaterials,* Liederdorp, the Netherlands, Reed Healthcare Communications, 1,**1992**

[28.] M. Sato, Y. H. An, E. B. Slamovich, et al., "Increased osseointegration for tantalum scaffolds coated with nanophase compared to conventional hydroxyapatite", *Int J Nanomed* (in press), **2006.**

[29.] J. E. Dalton, S. D. Cook., "In vivo mechanical and histological characteristics of HA-coated implants vary with coating vendor", *J Biomed Mater Res*, **1995,** 29, 239-245

[30.] F. Barrere, C. M. VanDerValk, R. A. Dalmeijer, et al., "*In vitro* and *in vivo* degradation of biomimetic octacalcium phosphate and carbonate apatite coatings on titanium implants.", *J Biomed Mater Res*, **2003**, 64A, 378-387

[31.] F. Barrere, P. Layrolle, C. A VanBlitterswijk, et al., "Biomimetic coatings on titanium: a crystal growth study of octacalcium phosphate", *J Mater Sci Mater Med*, **2001,** 12, 529-534

[32.] Liu Y, E. B. Hunziker, P. Layrolle, et al., "Bone morphogenetic protein 2 incorporated into biomimetic coatings retains its biological activity", *Tissue Eng*, **2004**, 10, 101-108

[33.] M. Stigter, J.Bezemer, K. DeGroot, et al., "Incorporation of different antibiotics into carbonated hydroxyapatite coatings on titanium implants, release and antibiotic efficacy", *J Control Release*, **2004**, 99, 127

[34.] T. J. Webster, R. W. Siegel, R. Bizios, "Osteoblast adhesion on nanophase ceramics", *Biomaterials*, **1999**, 20, 1221-1227

[35.] T. J. Webster, C. Ergun, R. H. Doremus, et al., "Enhanced functions of osteoblasts on nanophase ceramics", *Biomaterials*, **2000** 21, 1803-1810

[36.] T. J. Webster, C. Ergun, R. H. Doremus et al., "Enhanced functions of osteoclast-like cells on nanophase ceramics", *Biomaterials*, **2001**, 22, 1327-1333

[37.] R. L. Price, L. G. Gutwein, L. Kaledin et al., "Osteoblast function on nanophase alumina materials: influence of chemistry, phase and topography", *J Biomed Mater Res*, **2003,** 67A, 1284-1293

[38.] V. Perla, T. J, Webster, "Better osteoblast adhesion on nanoparticulate selenium—a promising orthopedic implant material", *J Biomed Mater Res*, **2005**, 75, 356-364

[39.] C.Yao, V. Perla, J. McKenzie et al., "Anodized Ti and Ti6A14V possessing nanometer surface features enhance osteoblast adhesion", *Biomed Nanotechnol*, **2005**, 1, 68-77

[40.] K. C. Popat, E. E. LearySwan, V. Mukhatyar et al., "Influence of nanoporous alumina membranes on long-term osteoblast response", *Biomaterials*, **2005***,* 26, 4516-4522

[41.] E. Palin, H. Liu, T. J Webster, "Mimicking the nanofeatures of bone increases bone-forming cell adhesion and proliferation", *Nanotechnology*, **2005,** 16, 1828-1835

[42.] M. Stigter, J. Bezemer, K. DeGroot, et al., "Incorporation of different antibiotics into carbonated hydroxyapatite coatings on titanium implants, release and antibiotic efficacy", *J Control Release*, **2004**, 99, 127-137

[43] M. Mathew and S. Takagi, "*Structures of Biological Minerals in Dental Research", J. Res. Natl. Inst. Stand. Technol*. **2001**,106, 1035–1044

[44] S. J. Kalita, S. Bose, H. L. Hosick and A. Bandyopadhyay, "$CaO–P_2O_5–Na_2O$-based sintering additives for hydroxyapatite (HAp) ceramics", *Biomaterials,* **2004**, 25(12), 2331-2339

[45.] A. F. Lemos, A. H. S. Rebelo, J. H. G. Rocha, J. M. F. Ferreira, "A Method for Simultaneously Precipitating and Dispersing nano-sized Calcium Phosphate Suspensions", *Key Engineering Materials,* **2005**, 284-286, 67-70

[46] C Loo, A. Lowery, N. Halas, J. West, "Immunotargeted nanoshells for integrated cancer imaging and therapy", *Nanolett*, **2005**, 5(4), 709-711

[47.] R. Trehin et al, "Fluoscent nanoparticle uptake for brain tumor visualization", *Neoplasia,* **2006**, 8 (4), 302-311

[48.] T Cyrus et al., "Three dimensional molecular imgaging of intramural biomarkers with targeted nanoparticles", *J Cardiovasc Magn Reson,* **2006**, 8 (3), 535-541

[49.] D Sullivan, M Ferrari, "Nanotechnology, tumor imaging- seizing an opportunity", Mol Imaging, **2004**, 3 (4) 364-369

[50.] P. Bertin et al, "Multifunctional polymeric nanoparticles for diverse bioactive agents", *J Am Chem Soc*, **2006**, 128 (13), 4168-4169

[51.] G. Orive, J.L. Pedraz, "Drug Delivery in biotechnology: present and future. *Curr Opin Biotechnol*, **2003**, 14, 659-654

[52.] G. Carinio, M. Edith, "Oral Insulin Delivery", *Ad Drug Deliv Rev*, **1999**, 35, 249-257

[53.] D. Mcallister, M. Prausnitz, "Microfabricated Microneedles for gene and drug delivery", *Annu Rev Biomed Engg*, **2000**, 2, 289-313

[54.] O M Koo, I Rubinstein, H Onyuksel, "Role of nanotechnology in targeted drug delivery and imaging: a concise review", *Nanomed Nanotechnol Biol Med*, **2005**, 1, 193-212

[55.] A. Khademhosseini, R. Langer, "Nanobiotechnology for tissue engineering and biotechnology", *Chemical Engineering Program*, **2006**, 102, 38-42

[56.] K Otilia, H Onyksel, "Role of nanotechnology in targeted delivery and imaging: a concise review", *Nanomedicine*, **2005**, 1, 193-212

[57] C. C Visser et al. "Nanoparticles bearing poly ethylene glycol- coupled transferring as gene carriers: preparation and in vitro evaluation", *Int J Pharm*, **2005**, 25, 209-305

[58.] C. P Leamon, J A Reddy "Folate targeted chemotherapy", *Adv Drug Deliv Rev*, **2004**, 80, 1127-1141

[59.] V Alvarez, L Sanz, "Antibody engineering facing new challenges in cancer therapy", *Acta Pharmacol Sin,* **2005**, 6, 641-648

[60.] R K. Majeti "Nano and micro particles as controlled drug delivery devices", *J Pharm Pharm Sci*, **2000**, 3 (2), 234-258

[61] W. Saltzman, S Baldwin, " Materials for protein delivery in tissue engineering", *Adv Drug Deliv Rev* , **1998**, 33, 71-86

[62] B. Kriwet, E. Walter, T. Kissel, "Synthesis of bioadhesive poly(acrylic acid) nano and microparticles using an inverse emulsion polymerization method for the entrapment of hydrophilic drug candidates", *Journal of Controlled Release* ,**1998**, 56 (1-3), 149-158

[63 T]. M. Allen, "Long-circulating (sterically stabilized) liposomes for targeted drug delivery ", *Trends in Pharmacological Sciences,* **1994**, 15 (7), 215

[64] A. Gabizon, A. T. Horowitz, D. Goren, D. Tzemach, H. Shmeeda, S. Zalipsky, "*In Vivo* Fate of Folate-Targeted Polyethylene-Glycol Liposomes in Tumor-Bearing Mice", *Clinical Cancer Research ,* **2003**, 9 (17), 6551-6559

[65] S. Ni, S. M. Stephenson, R. J. Lee, "Folate receptor targeted delivery of liposomal daunorubicin into tumor cells", *Anticancer Research,* **2002**, 22 (4), 2131-2135

[66] D. Sharma, T. P. Chelvi, J. Kaur, K. Chakravorty, T. K. De, A. Maitra , R. Ralhan, "Novel Taxol formulation: polyvinylpyrolidone nanoparticle-encapsulated Taxol", *Oncology Research,* **1996**, 8 (7-8), 281-287

[67] P. Kallinteri, S. Higgins, G. A. Hutcheon, C. B. St Pourcain, M. C. Garnett, "Novel functionalized biodegradable polymers for nanoparticle drug delivery systems", *Biomacromolecule,* **2005**, 6 (4), 1885

[68] M. V. Backer, R. Aloise, K. Przekop, K. Stoletov , J. M. Backer, "Molecular vehicles for targeted drug delivery", *Bioconjugate Chemistry ,* **2002**, 13 (3), 462-467

[69] J. K. Li, N. Wang , X. S. Wu, "Poly(vinyl alcohol) nanoparticles prepared by freezing–thawing process for protein/peptide drug delivery", *Journal of Controlled Release,***1998,** 56 (1-3), 117-126

[70] K. S. Soppimath, D. C. W. Tan, "pH-Triggered Thermally Responsive Polymer Core-Shell Nanoparticles for Drug Delivery", Y. Y. Yang, *Advanced Materials,* **2005**, 17 (3), 318-319

[71]M. Kullberg, K. Mann, J. L. Owens," Improved drug delivery to cancer cells: a method using magnetoliposomes that target epidermal growth factor receptors", *Medical Hypotheses,* **2005**, 64 (3), 468-470

[72.] I. V. Larina, B. M. Evers, T. V. Ashitkov, C. Bartels, K. V. Larin , R. O. Esenaliev, "Enhancement of drug delivery in tumors by using interaction of nanoparticles with ultrasound radiation.", *Technology in Cancer Research & Treatment,* **2005**, 4 (2), 217-226

[73] Y. Ogura, T. Guran, M. Shahidi, M. T. Mori, R. C. Zeimer, "Feasibility of targeted drug delivery to selective areas of the retina", *Investigative Ophthalmology & Visual Science,* **1991**, 32 (8), 2351-2356

[74] K. L. Shantha, P. Ravichandran, K. P. Rao, "Azo polymeric hydrogels for colon targeted drug delivery", *Biomaterials,* **1995,** 16 (17), 1313-1318

[75] P. M. Bummer, *Critical Reviews™ in Therapeutic Drug Carrier Systems,* **2004**, 21 (1), 1

[76] M. N. Jones, "Carbohydrate-mediated liposomal targeting and drug delivery ", *Advanced Drug Delivery Reviews,* **1994**, 13 (3), 215-250

[77] S. A. Wissing, O. Kayser and R. H. Muller, "Solid lipid nanoparticles for parenteral drug delivery"**,** *Advanced Drug Delivery Reviews,* **2004**, 56 (9), 1257-1272

[78] H. Suzuki, D. Nakai, T. Seita and Y. Sugiyama, "Design of a drug delivery system for targeting based on pharmacokinetic consideration**",** *Advanced Drug Delivery Reviews ,* **1996**, 19 (3), 335-357

[79] Y. Kaneda, "Virosomes: evolution of the liposome as a targeted drug delivery system**",** *Advanced Drug Delivery Reviews,* **2000**, 43 (2-3), 197-205

[80] I. Bala, S. Hariharan, M. Kumar, "PLGA Nanoparticles in drug delivery: The state of art", *Critical Reviews in Therapeutic Drug Carrier Systems,* **2004**, 21 (5), 387-422

[81] M. J. Cappel, J. Kreuter, "Effect of nanoparticles on transdermal drug delivery", *Journal of Microencapsulation,* **1991**, 8 (3), 369

[82] C. Chauvierre, C. Vauthier, D. Labarre, P. Couvreur, M. C. Marden , L. Leclerc, “A new generation of polymer nanoparticles for drug delivery”, *Cellular and Molecular Biology ,***2004**, 50 (3), 233-239

[83] T. K. De, A. S. Hoffman, “A Reverse Microemulsion Polymerization Method For Preparation Of Bioadhesive Polyacrylic Acid Nanoparticles For Mucosal Drug Delivery: Loading And Release Of Timolol Maleate”, *Art Cells Blood Subs Immob Biotech,* **2001**, 29 (1), 31-46

[84] M. S. Elsamaligy, P. Rohdewald, "Reconstituted Collagen Nanoparticles, a Novel Drug Carrier Delivery System.", *Journal of Pharmacy and Pharmacology*, **1983**, 35 (8), 537-539

[85] A. M. de Campos, Y. Diebold, E. L. S. Carvalho, A. Sanchez , M. J. Alonso, "Chitosan nanoparticles as new ocular drug delivery systems: in vitro stability, in vivo fate, and cellular toxicity."*Pharmaceutical Research,* **2004**, 21 (5), 803-810

[86] P. V. Finotelli, M. A. Morales, M. H. Rocha-Leao, E. M. Baggio-Saitovitch, A. M. Rossi, "Magnetic studies of iron(III) nanoparticles in alginate polymer for drug delivery applications.", *Materials Science & Engineering C-Biomimetic and Supramolecular Systems ,* **2004**, 24 (5)625-629

[87] G. F. Paciotti, L. Myer, D. Weinreich, D. Goia, N. Pavel, R. E. McLaughlin , L. Tamarkin, "Colloidal gold: A novel nanoparticle vector for tumor directed drug delivery."*Drug Delivery,* **2004**, 11 (3), 169-183

[88] G. F. Paciotti, L. D. Myer, T. H. Kim, S. Wang, H. R. Alexander, D. Weinreich , L. Tamarkin, "Colloidal gold: A novel colloidal nanoparticle vector for tumor-directed drug delivery."*Clinical Cancer Research,* **2001**, 7 (11), 3673S-3674S

[89] J. F. Chen, H. M. Ding, J. X. Wang , L. Shao, "Preparation and characterization of porous hollow silica nanoparticles for drug delivery application", *Biomaterials ,* **2004**, 25 (4), 723-727

[90] Y. Ueno, H. Futagawa, Y. Takagi, A. Ueno, Y. Mizushima, Mizushima, "Drugincorporating calcium carbonate nanoparticles for a new delivery system", *Journal of Controlled Release* **2005**, 103 (1), 93-98

[91] N. Venkatesan, J. Yoshimitsu, Y. Ito, N. Shibata, K. Takada, "Liquid filled nanoparticles as a drug delivery tool for protein therapeutics", *Biomaterials ,* **2005**, 26 (34), 7154-7163

[92] P. Legrand, G. Barratt, V. Mosqueira, H. Fessi , J. P. Devissaguet, "Polymeric nanocapsules as drug delivery systems - A review", *Stp Pharma Sciences,* **1999**, 9 (5), 411-418

[93] A. Rahman, J. Treat, J. K. Roh, L. A. Potkul, W. G. Alvord, D. Forst, P. V. Woolley, "A Phase-I Clinical-Trial and Pharmacokinetic Evaluation of Liposome- Encapsulated Doxorubicin", *Journal of Clinical Oncology,* **1990**, 8 (6), 1093-1100

[94] L. D. Mayer, M. B. Bally, M. J. Hope , P. R. Cullis, "Techniques for Encapsulating Bioactive Agents into Liposomes", *Chemistry and Physics of Lipids ,***1986**, 40 (2-4), 333-345

[95] C. R. Alving, "Delivery of Liposome-Encapsulated Drugs to Macrophages", *Pharmacology & Therapeutics,* **1983**, 22 (3), 407-424

[96]. R. Fraley, S. Subramani, P. Berg , D. Papahadjopoulos, "Introduction of Liposome-Encapsulated Sv40 DNA into Cells", *Journal of Biological Chemistry*, **1980**, 255 (21), 431-435

[97] H. M. Patel, B. E. Ryman, "Oral-Administration of Insulin by Encapsulation within Liposomes", *Febs Letters,* **1976**, 62 (1), 60-63

[98] A. Gabizon, D. Goren, A. T. Horowitz, D. Tzemach, A. Lossos , T. Siegal, "Long-circulating liposomes for drug delivery in cancer therapy: A review of biodistribution studies in tumor-bearing animals", *Advanced Drug Delivery Reviews ,***1997**, 24 (2-3), 337-344

[99] O. P. Medina, Y. Zhu, K. Kairemo, "Targeted liposomal drug delivery in cancer." *Current Pharmaceutical Design Current Pharmaceutical Design",* **2004**, 10 (24), 2981-2989

[100] P. Kaplun, L. B. Son, Y. M. Krasnopolsky , V. I. Shvets, *Voprosy Meditsinskoi Khimii*, "Liposomes and others nanoparticles as the drug delivery systems." **1999**, 45 (1), 3-12

[101] B. Rihova, "Receptor-mediated targeted drug or toxin delivery." *Advanced Drug Delivery Reviews,* **1998**, 29: (3), 273-289

[102] S. P. Vyas, A. Singh and V. Sihorkar, "Ligand-receptor-mediated drug delivery:An emerging paradigm in cellular drug targeting." *Critical Reviews in Therapeutic Drug Carrier Systems,* **2001**, 18 (1), 1-76

[103] W. Arap, R. Pasqualini, E. Ruoslahti, "Cancer treatment by targeted drug delivery to tumor vasculature in a mouse model", *Science,* **1998**, 279 (5349), 377-380

[104] L. W. Seymour, P. A. Flanagan, A. Alshamkhani, V. Subr, K. Ulbrich, J. Cassidy , R. Duncan, "Synthetic-Polymers Conjugated to Monoclonal-Antibodies - Vehicles for Tumor-Targeted Drug Delivery", *Selective Cancer Therapeutics*, **1991**, 7 (2), 59-73

[105] A. O. Eniola, D. A. Hammer, "Artificial polymeric cells for targeted drug delivery", *Journal of Controlled Release,* **2003**, 87 (1-3), 15-22

[106] C. P. Leamon, J. A. Reddy, "Folate-targeted chemotherapy", *Advanced Drug Delivery Reviews,* **2004**, 56 (8), 1127-1141

[107] M. A. Jepson, M. A. Clark, B. H. Hirst, "M cell targeting by lectins: a strategy for mucosal vaccination and drug delivery", *Advanced Drug Delivery Reviews*, **2004**, 56(4), 511-525

[108] N. Yamazaki, S. Kojima, N. V. Bovin, S. Andre, S. Gabius , H. J. Gabius, "Endogenous lectins as targets for drug delivery", *Advanced Drug Delivery Reviews,* **2000**, 43 (2-3), 225-244

[109] B. A. Gruner, S. D. Weitman, "The folate receptor as a potential therapeutic anticancer target", *Investigational New Drugs ,* **1998**, 16 (3), 205-219

[110] A. L. Jackman, D. S. Theti, D. D. Gibbs, “Antifolates targeted specifically to the folate receptor”, *Advanced Drug Delivery Reviews,* **2004**, 56 (8), 1111-1125

[111] G. T. Hermanson, *Bioconjugate Techniques*, **1996.**

[112] M. A. Rauschmann, T. A. Wichelhaus, V. Stirnal, E. Dingeldein, L. Zichner, R. Schnettler , V. Alt, "Nanocrystalline hydroxyapatite and calcium sulphate as biodegradable composite carrier material for local delivery of antibiotics in bone infections", *Biomaterials,* **2005**, 26 (15), 2677-2684

[113] K. Cheng, L. Y. Lim, "Insulin-loaded calcium pectinate nanoparticles: Effects of pectin molecular weight and formulation pH.", *Drug Development and Industrial Pharmacy,* **2004**, 30 (4), 359-367

[114] C. Sfeir, J. Bennett, P. Kumta, "Nanosized calcium phosphate particles for plasmid gene delivery", *Molecular Therapy,* **2003**, 7 (5), S225-S225

[115] T. C. Chu, Q. He, D. E. Potter, "Biodegradable calcium phosphate nanoparticles as a new vehicle for delivery of a potential ocular hypotensive agent", *Journal of Ocular Pharmacology and Therapeutics,* **2002**, 18 (6), 507-514

[116] T. C. Chu, Q. He, S. Bell, D. E. Potter, "Biodegradable calcium phosphate nanoparticles (cap) as a new vehicle for delivery of a potential anti-glaucoma agent", *Investigative Ophthalmology & Visual Science ,* **2002**, 43, U553-U553

[117] Y. Kakizawa, S. Furukawa, K. Kataoka, "Block copolymer-coated calcium phosphate nanoparticles sensing intracellular environment for oligodeoxynucleotide and siRNA delivery", *Journal of Controlled Release,* **2004**, 97 (2), 345-356

[118] T. Liu, A. Tang, G. Y. Zhang, Y. X. Chen, J. Y. Zhang, S. S. Peng , Z. M. Cai, "Calcium phosphate nanoparticles as a novel nonviral vector for efficient trasfection of DNA in cancer gene therapy", *Cancer Biotherapy and Radiopharmaceuticals ,* **2005**, 20 (2), 141-149

[119] S. Bisht, G. Bhakta, S. Mitra, A. Maitra, "pDNA loaded calcium phosphate nanoparticles: highly efficient non-viral vector for gene delivery", *International Journal of Pharmaceutics,* **2005**, 288 (1), 157-168

[120] Y. W. Yang, J. C. Yang, "Calcium phosphate as a gene carrier: Electron microscopy", *Biomaterials,* **1997**, 18 (3), 213-217

[121] F. G. E. Pautard, "Calcium-Phosphate Microspheres in Biology", *Progress in Crystal Growth and Characterization of Materials,* **1981**, 4 (1-2), 89-98

[122] P. Iooss, A. M. Le Ray, G. Grimandi, G. Daculsi , C. Merle, "A new injectable bone substitute combining poly(epsilon-caprolactone) microparticles with biphasic calcium phosphate granules", *Biomaterials ,***2001**, 22 (20), 2785

[123] S. Larsson, T. W. Bauer, "Use of injectable calcium phosphate cement for fracture fixation: A review." *Clinical Orthopaedics and Related Research,* **2002,** (395), 23-32

[124] J. P. Schmitz, J. O. Hollinger, S. B. Milam, "Reconstruction of bone using calcium phosphate bone cements: A critical review." *Journal of Oral and Maxillofacial Surgery,* **1999**, 57 (9), 1122-1126

[125] J. S. V. Albuquerque, J. V. F. Neto, J. Junior, D. O. Lima, R. Nogueira, M. H. P. da Silva, "Porous bioceramics produced with calcium phosphate nanoparticles", *Bioceramics,* **2003**, 240-2, 23-26

[126] K. Fujihara, M. Kotaki, S. Ramakrishna, "Guided bone regeneration membrane made of polycaprolactone/calcium carbonate composite nano-fibers", *Biomaterials,* **2005**, 26 (19), 4139-4147

[127] K. H. Nan, Y. J. Wang, X. F. Chen, N. R. Zhao , L. Y. Wang, "Microstructure and controllable degradation of bioglass reinforced calcium phosphate scaffolds", *High-Performance Ceramics Iii, Pts 1 and 2 ,***2005**, 280-283 ,1599

[128] M. Nilsson, E. Fernandez, S. Sarda, L. Lidgren, J. A. Planell, "Microstructure analysis of novel resorbable calcium phosphate/sulphate bone cements."*Bioceramics 14,* **2002**, 218-2, 365

[129] H. R. R. Ramay, M. Zhang, "Biphasic calcium phosphate nanocomposite porous scaffolds for load-bearing bone tissue engineering", *Biomaterials,* **2004**, 25 (21), 5171-5180

[130] M. Shirkhanzadeh, S. Sims, "Immobilization of calcium phosphate nanoclusters into alkoxy-derived porous TiO2 coatings."*Journal of Materials Science- Materials in Medicine,* **1997**, 8 (10), 595-601

[131] M. Shirkhanzadeh, "Microneedles coated with porous calcium phosphate ceramics: Effective vehicles for transdermal delivery of solid trehalose." *Journal of Materials Science-Materials in Medicine,* **2005**, 16 (1), 37-45

[132] C. C. Ribeiro, C. C. Barrias, M. A. Barbosa, "Calcium phosphate-alginate microspheres as enzyme delivery matrices", *Biomaterials,* **2004**, 25 (18), 4363-4373

[133] K. Degroot, "Clinical-Applications of Calcium-Phosphate Biomaterials – a Review", *Ceramics International,* **1993**, 19 (5), 363-366

[134] C. Montero-Ocampo, D. Villegas, L. Veleva, "Controlled potential electrodeposition of calcium phosphate on Ti6Al4V", *Journal of the Electrochemical Society, **2005***, 152 (10), C692-C696

[135] E. P. Paschalis, Q. Zhao, B. E. Tucker, S. Mukhopadhayay, J. A. Bearcroft, N. B. Beals, M. Spector ,G. H. Nancollas, "Degradation potential of plasma-sprayed hydroxyapatite-coated titanium implants", *Journal of Biomedical Materials Researc ,* **1995**, 29 (12), 1499-1505

[136] Y. Z. Yang, K. H. Kim , J. L. Ong, "Review on calcium phosphate coatings produced using a sputtering process - an alternative to plasma spraying", *Biomaterials,* **2005**, 26 (3), 327-337

[137] F. Lusquinos, J. Pou, A. Boutinguiza, F. Quintero, R. Soto, B. Leon, M. Perez-Amor, "Main characteristics of calcium phosphate coatings obtained by laser cladding."*Applied Surface Science,* **2005**, 247 (1-4), 486-492

[138] J. H. Park, Y. K. Lee, K. M. Kim , K. N. Kim, "Bioactive calcium phosphate coating prepared on H_2O_2-treated titanium substrate by electrodeposition." *Surface & Coatings Technology,* **2005**, 195 (2-3), 252-257

[139] J. W. Nah, Y. I. Jeong, C. S. Cho , S. I. Kim, "Drug-delivery system based on core-shell-type nanoparticles composed of poly(gamma-benzyl-L-glutamate) and poly(ethylene oxide)." *Journal of Applied Polymer Science,* **2000**, 75 (9), 1115-1126

[140] T. Riley, C. R. Heald, S. Stolnik, M. C. Garnett, L. Illum, S. S. Davis, S. M. King, R. K. Heenan, S. C. Purkiss, R. J. Barlow, P. R. Gellert, C. Washington, "Core-shell structure of PLA-PEG nanoparticles used for drug delivery." *Langmuir,* **2003**, 19 (20), 8428-8435

[141] K. S. Oh, K. E. Lee, S. S. Han, S. U. H. Cho, D. Kim , S. H. Yuk, "Formation of core/shell nanoparticles with a lipid core and their application as a drug delivery system." *Biomacromolecules,* **2005**, 6 (2), 1062-1067

[142] Donaldson K, Aitken R, Tran L, Stone V, Duffin R, Forrest G, "Carbon nanotubes: a review of their properties in relation to pulmonary toxicology and workplace safety", *Toxicol Appl Pharmacol,* **2006**; 92:5–22.

[143] Eerikainen H, Watanabe W, Kauppinen EI, Ahonen PP. "Aerosol flow reactor method for synthesis of drug nanoparticles", *Eur J Pharm Biopharm,* **2003**, 55, 357–360.

[144] Oberdörster G, Oberdörster E, Oberdörster J. "Nanotoxicology: an emerging discipline evolving from studies of ultrafine particles", *Environ Health Perspect,* **2005b**; 113, 823–839.

[145] Brown DM, Wilson MR, MacNee W, Stone V, Donaldson K. "Size-dependent proinflammatory effects of ultrafine polystyrene particles: a role for surface area and oxidative stress in the enhanced activity of ultrafines", *Toxicol Appl Pharmacol.* **2001**, 175, 191–199.

[146] Lam C-W, James JT, McCluskey R, Hunter RL. "Pulmonary toxicity of single-wall carbon nanotubes in mice 7 and 90 days after intratracheal instillation", *Toxicol Sci.* **2004**, **77**, 126–134.

[147] Berry JP, Arnoux B, Stanislas G, Galle P, Chretien J., "A microanalytic study of particles transport across the alveoli: role of blood platelets"*, Biomedicine,* **1977**, 27, 354–357.

[148] Nemmar A, Hoet PHM, Vanquickenborne B, Dinsdale D, Thomeer M, Hoylaerts MF," Passage of inhaled particles into the blood circulation in humans", *Circulation.* **2002**, 105, 411–414.

[149] Radomski A, Jurasz P, Alonso-Escolano D, Drews M, Morandi M, Malinski T, et al. "Nanoparticle-induced platelet aggregation and vascular thrombosis", *Br J Pharmacol.* **2005**, 146, 882–893.

[150] Yamawaki H, Iwai N, "Mechanisms underlying nano-sized air-pollution-mediated progression of atherosclerosis: carbon black causes cytotoxic injury/inflammation and inhibits cell growth in vascular endothelial cells", *Circ J.* **2006**, 70, 129–140.

[151] Cui D, Tian F, Ozkan CS, Wang M, Gao H. "Effect of single wall carbon nanotubes on human HEK293 cells*", Toxicol Lett,* **2005,**155, 73–85.

[152] Fechter LD, Johnson DL, Lynch RA, "The relationship of particle size to olfactory nerve uptake of a non-soluble form of manganese into brain", *Neurotoxicology,* **2002**, 23, 177–183.

[153] Olanow C.W., "Manganese-induced parkinsonism and Parkinson's disease", *Ann N Y Acad Sci,* **2004**, 1012, 209–223.

[154] Hussain SM, Javorina A, Schrand AM, Duhart H, Ali SF, Schlager J J, "The interaction of manganese nanoparticles with PC-12 cells induces dopamine depletion", *Toxicol Sci.,* **2006**, 92:456–463.

[155] Chen Z, Meng H, Xing G, Chen C, Zhao Y, Jia G, et al. "Acute toxicological effects of copper nanoparticles *in vivo", Toxicol Lett,* **2006**; 163, 109–120.

[156] Lomer MC, Thompson RP, Powell J J. "Fine and ultrafine particles of the diet: influence on the mucosal immune response and association with Crohn's disease", *Proc Nutr Soc,* **2002**; 61,123–130.

[157] Podolsky DK. 'Inflammatory bowel disease *", N Engl J Med.* **2002**, 347: 417–429

[158] Kim S, Lim YT, Soltesz EG, De Grand AM, Lee J, Nakayama A, et al. "Near-infrared fluorescent type II quantum dots for sentinel lymph node mapping", *Nat Biotechnol.* **2004**; 22, 93–97.

[159] Shvedova AA, Castranova V, Kisin ER, Schwegler-Berry D, Murray AR, Gandelsman VZ, "Exposure to carbon nanotube material: assessment of nanotube cytotoxicity using human keratinocyte cells", *J Toxicol Environ Health A.* **2003,** 66, 1909–1926.

[160] G Kroemer., N. Zamzami, S.A. Susin," Mitochondrial control of. Apoptosis", *Immunol. Today*, **1997**, 18, 44-49

[161] Kruman, I., Guo, Q. and Mattson, M.P., "Calcium and reactive oxygen species mediate staurosporine-induced mitochondrial dysfunction and apoptosis in PC12 cells**",** *J. Neurosci. Res.,* **1998**, 51, 293-308

[162] E O Kajander, "Nanobacteria — Propagating calcifying nanoparticles", *Lett. Appl. Microbiol.*, **2006**, 42**,** 549-552

[163]C. A. Van Blitterswijk , J. J. Grote , H. K. Koerten , W. Kuijpers The biological performance of calcium phosphate ceramics in an infected implantation site III: Biological performance of whitlockite in the noninfected and infected rat middle ear, Journal of Biomedical Materials Research, **2004**, 20 [8] 1197–1217

[164] E Lugscheider, M. Knepper, B Heimberg, A. Dekker, C.J. Kirkpatrick, "Cytotoxicity investigations of plasma sprayed calcium phosphate coatings," Journal of Materials Science: Materials in Medicine , **1994**, 5[6-7] 371-375

[165] J.R. Woodard; A.J. Hilldore; S.K. Lan, C.J. Park; A.W. Morgan, J.A. Eurell; S.G. Clark, M.B. Wheeler, R.D. Jamison, J. A.J. Wagoner,"The mechanical properties and osteoconductivity of hydroxyapatite bone scaffolds with multi-scale porosity ," Biomaterials,**2007**, 28 [1] 45-54

[166] J. Marrow; H. Imaizumi, M. Sakurai; O. Kashimoto; T Kikawa, O.Suzuki,"Comparative Study on Osteoconductivity by Synthetic Octacalcium Phosphate and Sintered Hydroxyapatite in Rabbit Bone," *Calcified Tissue International:Medicine*, **2006**, 78 [1] 45-54

[167] C. P. A. T. Klein, A. A Driessen, K,Groot de, A Hooff van den,."Biodegradation behavior of various calcium phosphate materials in bone tissue," Journal of Biomedical Materials Research, **2004**, 17 [5] 769–784

[168] S. F. Hulbert, J. C. Bohros, L. L. Hench, J. Wilson, G. Heirnke, In High Tech Ceramics. Elsevier: Amsterdam, The Netherlands, **1987**, p 189

[169] El-Ghannam A, **"**Bone reconstruction: from bioceramics to tissue engineering", *Expert Rev Med Devices*, **2005**, 2-1, 87-101

[170] L.A. Bauer, N. S. Birenbaum, G. J. Meyer**, "**Biological applications of high aspect ratio nanoparticles", *J. Mater. Chem*., **2004**, 14, 517-526

[171]A. Bigi, E. Foresti, M. Gandolfi, M. Gazzano, N. Roveri, "Isomorphous substitutions in tricalcium phosphate: the different effects of zinc and strontium", *J. Inorg. Biochem*, **1997**, 66 259–265,

[172] Y. Yokogawa, Y. Kawamoto, M. Toriyama, T. Suzuki, S. Kawamura, "Tricalcium phosphate coating on zirconia using calcium metaphosphate and tetracalcium phosphate", *J. Ceram. Soc. Jpn*, **1991**, 99 28–31

[173] R. Famery, N. Richard, P. Boch, "Preparation of and tricalcium phosphate ceramics, with and without magnesium addition"*, Ceram. Int*, **1994**, 20 327–336

[174] Y. Pan, J.L. Huang, C.Y. Shao, "Preparation of TCP with high thermal stability by solid reaction routes",. *J. Mater Sci***, 2003**, 38 1049–1056

[175] S.C. Liou, S.Y Chen, "Transformation mechanism of different chemically precipitated apatitic precursors into tricalcium phosphate upon calcinations", *Biomaterials*, **2002**, 23, 4541–4547

[176] M. Jarcho, R.L. Salsbury, M.B. Thomas, R.H. Doremus, "Synthesis and fabrication of tricalcium phosphate (whitlockite) ceramics for potential prosthetic applications", *J. Mater. Sci*., **1979**, 14 142–150

[177]M. Akao, H. Aoki, K. Kato, A. Sato, "Dense Polycrystalline tricalcium phosphate for prosthetic applications", *J. Mater Sci*, **1982**, 17, 343–346

[178] K. Itatani, T. Nishioka, S. Seike, F.S. Howell, A. Kishioka, M. Kinoshita, "Sinterability of calcium orthophosphate powder prepared by spray-pyrolysis", *J Am Ceram Soc*., **1994**, 77 [3], 801–805

[179]A.C Tas, F. Korkusus, M. Timucin, N. Akkas, "An investigation of the chemical synthesis and high-temperature sintering behavior of calcium hydroxyapatite (HA) and tricalcium phosphate (TCP) bioceramics", *J. Mater Sci. Mater. Med*., **1997**, 8, 91–96

[80] E Hayek and H Newesely, "Pentacalcium Monohydroxyorthophosphate," *Inorg. Syn.*, **1963**, 7, 63-65

[181] A. Deptula, W. Lada, T. Olzczak, A. Borello, C. Alvani, A. Dibartolomeo, "Preparation of spherical powders of hydroxyapatite by sol–gel process", *J of Non. Cryst. Solids,* **1992,** 147, 537-541

[182] H. Hattori,Y. Iwadate, "Hydrothermal Preparation of Calcium Hydroxyapatite Powders", *J Am Ceram. Soc*., **1990,** 73, 1803-1805

[183] S. Bose and S. K. Saha, “Synthesis and Characterization of Hydroxyapatite Nanopowders by Emulsion Technique”, *Chem. Mater.*, **2003,** 15 (23), 4464-4469

[184] S. Bose and S. K. Saha, “Synthesis of Hydroxyapatite Nanopowders via Sucrose-Templated Sol-Gel Method “, *J American Ceram Soc*., **2003**, 86 (6), 1055-1059

[185] P. Layrolle, A. Ito, T. Tateishi., “Sol-Gel Synthesis of Amorphous Calcium Phosphate and Sintering into Microporous Hydroxyapatite”, *J American Ceram Soc*., **1998**, 81(6), 1421-1426

[186] D.M. Liu, T. Troczynski, W.J. Tseng. "Water-based sol-gel Synthesis of Hydroxyapatite: Process Development", *Biomat*, **2001**, 22, 1721-1730

[187] D.M. Liu, T. Troczynski, W.J. Tseng. “Structural evolution of sol–gel-derived hydroxyapatite”, *Biomat*, **2002**, 23, 1679-1687

[188] Y. Han, S. Li, X Wang, X. Chen,” Synthesis and sintering of nanocrystalline hydroxyapatite powders by citric acid sol–gel combustion method “, *Mater Res Bull*, **2004**, 39, 25-32

[189] A. Destainville, E. Champion, D. Bernache-Assollant, E. Laborde, “Synthesis, characterization and thermal behavior of apatitic tricalcium phosphate**”,** *Materials Chemistry and Physics***, 2003,** 80, 269-277

[190] J. Pena, M. Vallet-Regı, “Hydroxyapatite, tricalcium phosphate and biphasic materials prepared by a liquid mix technique”, *Journal of the European Ceramic Society*, **2003**, 23, 1687-1693

[191] J.S. Bowa, S.C. Lioub, S.Y. Chen, “Structural characterization of room temperaturesynthesized nano-sized β-tricalcium phosphate," *Biomaterials*, **2004,** 25, 3155-3161

[192] M. Uota, H. Arakawa, N. Kitamura, T. Yoshimura, J. Tanaka, T. Kijima, “Synthesis of High Surface Area Hydroxyapatite Nanoparticles by Mixed Surfactant-Mediated Approach**”,** *Langmuir***, 2005,** *21*, 4724-4728

[193] D. Rautaray, S. Mandal, M. Sastry, "Synthesis of Hydroxyapatite Crystals Using Amino Acid-Capped Gold Nanoparticles as a Scaffold**",** *Langmuir***, 2005,** *21*, 5185-5191

[194] G.K. Lim, J. Wang, S.C. Nag and L.M. Gan," Formation of nanocrystalline hydroxyapatite in nonionic surfactant emulsions", *Langmuir*, **1999**, *15*, 7472-7477

[195] G.K. Lim, J. Wang, S.C. Nag and L.M. Gan, "Nanosized hydroxyapatite powders from microemulsions and emulsions stabilized by a biodegradable surfactant", *J Mater. Chem*, **1999**, 9, 1635- 1639

[196] M. Cao,Y. Wang, C. Guo, Y. Qi, C. Hu, "Preparation of ultrahigh –aspect- ratio hydroxyapatite nanofibers in reverse micelles under hydrothermal conditions",

Langmuir, **2004,** 20, 4784-4786

[197] Y. Sun, G. Guo, D. Tao, Z. Wang, "Reverse microemulsion-directed synthesis of hydroxyapatite nanoparticles under hydrothermal conditions"*,Journal of Physics and Chemistry of Solids*, **2007**, 68, 373-377

[198] Y. Wu, S. Bose, "Nanocrystalline hydroxyapatite: micelle templated synthesis and characterization", *Langmuir*, **2005,** 21(8), 3232-3237

[199] Atkins P W. *Physical chemistry*, 5th ed. New York: W.H. Freeman, **1994**

[200] SAS 9.1, The SAS Institute. The SAS System for Windows Release 9.1, SAS Inst., Cary, NC, **2003**

[201] R.Z. Legeros, *In Calcium Phosphates in Oral Biology and Medicine;* Edited by Myers, H.M., Karger, Switzerland, **1991**, 85.

[202] J.C. Elliott, *In Structure and chemistry of the apatites and other calcium orthophosphates*, *Studies in Inorganic Chemistry*, Elsevier, Netherlands, **1994,** l8, p112.

[203] M. Vallet-Regı, J Pena, I Izquierdo-Barba, "Synthesis of β-tricalcium phosphate in layered or

powdered forms for biomedical application", *Solid State Ionics*, **2004**, 172, 445-449

[204] Tripathy, S.K.; Black, H.B.; Goldwasser, E.; Leiden, J.M. "Immune responses to transgene-encoded proteins limit the stability of gene expression after injection of replication-defective adenovirus vectors", *Nat Med*. **1996**, 5, 545-550

[205] Zelphati, O.; Nguyen, C.; Ferrari, M.; Felgner, J.; Tsai, Y.; Felgner, P.L. "Stable and monodisperse lipoplex formulations for gene delivery", *Gene Ther*. **1998,** 5, 1272-1282

[206] Schmidt, H. T.; Gray, B. L.; Wingert, P. A.; Ostafin, A. E. "Assembly of Aqueous-Cored Calcium Phosphate Nanoparticles for Drug Delivery", *Chem. Mater*. **2004**, 16; 4942-4947

[207] Yang, J.; Lee, J.; Kang, J.; Lee, K.; Suh, J.S.; Yoon, H.G.; Huh, Y.M.; Haam, S. "Hollow Silica Nanocontainers as Drug Delivery Vehicles", *Langmuir*. **2008**, 24; 3417-3421

[208] Chen, C.C.; Lin, Y.P.; Wang, C.W.; Tzeng, H.C.; Wu, C.H..; Chen, Y.C.; Chen, C.P.; Chen, L.C.; Wu,Y.C. "DNA-Gold Nanorod Conjugates for Remote Control of Localized Gene Expression by near Infrared Irradiation", *J. Am. Chem. Soc*. **2006**, 128, 3709-3715

[209] Salem, A.K.; Searson, P.C.; Leong, K.W. "Multifunctional nanorods for gene delivery", *Nature Materials*, **2003**, 2, 668-671

[210] Lim, I.I.S.; Ouyang, J.; Luo, J.; Wang, L.; Zhou, S.; Zhong, C. J. "Multifunctional Fullerene-Mediated Assembly of Gold Nanoparticles**",** *Chem. Mater*. **2005**, 17, 6528-6531

[211] Joshi, H.M.; Bhumkar, D. R..; Joshi, K.; Pokharkar, V.; Sastry, M. "Gold Nanoparticles as Carriers for Efficient Transmucosal Insulin Delivery ", *Langmuir* **2006**, *22,* 300.-305

[212] Krueger, A. "New Carbon Materials: Biological Applications of Functionalized Nanodiamond Materials", *Chem. Eur. J.* **2008**, 14, 1382-1390

[213] Fuertes, A. B.; Matra, S.; Teresa V.S.; Pedro, T. "Synthetic Route to Nanocomposites Made Up of Inorganic Nanoparticles Confined within a Hollow Mesoporous Carbon Shell", *Chem. Mater.* **2007**, 19*,* 5418-5423

[214] Fuertes, A. B.; Teresa, V.S.; Marta, S. *J "*Fabrication of Monodisperse Mesoporous Carbon Capsules Decorated with Ferrite Nanoparticles",. *Phys. Chem. C* **2008**, 112*,* 3648-3654

[215] Liu, C.; Zhang, Z. J., "Size-Dependent Superparamagnetic Properties of Mn Spinel Ferrite Nanoparticles Synthesized from Reverse Micelles", *Chem. Mater*. **2001**, 13, 2092-2096

[216] Xu, P. Z.; Lu, G. Q. "Layered double hydroxide nanomaterials as potential cellular drug delivery agents", *Pure Appl. Chem.* **2006**, 78, 1771-1779

[218] Sokolova, V. V.; Radtke, I.; Heumann, R.; Epple, M. "Effective transfection of cells with multi-shell calcium phosphate-DNA nanoparticles", *Biomaterials*. **2006**, 27, 3147-3153

[219] Habibovic, P.; Barrere, F.; Van Blitterswijk, C. A.; De Groot, K.; Layrolle, P. "Biomimetic hydroxyapatite coating on. metal implants", *J Am. Chem. Soc.* **2002**, 3, 517-522

[220] Gorbunoff, M. J., "The interaction of proteins with hydroxyapatite. I. Role of protein charge and structure", *Anal. Biochem*. **1984**, 136, 425-432

[221] Zambonin, G.; Camerino, C.; Greco, G.; Patella, V.; Moretti, B.; Grano, M., "Hydroxyapatite coated with hepatocyte growth factor (HGF) stimulates human osteoblasts in vitro", *J Bone Joint Surg [Br]*. **2000**; 82B, 457-460

[222] Okubo, Y.; Bessho, K.; Fujimura, K.; Kusumoto, K.; Ogawa, Y.; Iizuka, T. "Osteogenesis by Recombinant Human Bone Morphogenetic Protein-2 at Skeletal Sites", *Clin. Orthop*. **2000**; 375, 295-301

[222] Ono, I.; Ohura, T.; Murata, M.; Yamaguchi, H.; Ohnuma, Y.; Kuboki, Y., "A study on bone induction in hydroxyapatite combined with bone morphogenetic protein", *Plast Reconstr Surg.* **1992**; 90, 870-879

[223] K.I. Jntema, W.J.M. Heuvelsland, C.A.M.C. Dirix, A.P. Sam, "HA microcarriers for biocontrolled release of protein drugs", *Int. J. Pharm*., **1994**, 112, 215-224

[224] T.Y. Liu; S. Y. Chen, D.M. Liu, S. C. Liou, "On the study of BSA-loaded calcium-deficient hydroxyapatite nano-carriers for controlled drug delivery", *J Controlled Release*, **2005**,107, 112-121

[225] Matsumotoa, T.; Okazakib, M.; Inouec, M.; Yamaguchic, S., Kusunosec, T.; Toyonagaa, T.; Hamadaa,Y.; Takahashi, J. "Hydroxyapatite particles as a controlled release carrier of protein", *Biomaterials*. **2004**, 25, 3807-3812

[226] Jung , U.W.; Choi, S.Y.; Pang, E.K.; Kim, C.S.; Choi, S.H.; Cho, K.S. "The effect of varying the particle size of beta tricalcium phosphate carrier of recombinant human bone morphogenetic protein-4 on bone formation in rat calvarial defects", *J. Periodontol*.**2006**, *77*, 765-772

[227] Yuan, H.; de Bruijn, J.D., Zhang, X.; van Blitterswijk, C.A.; de Groot, "Use of an osteoinductive biomaterial as a bone morphogenetic protein carrier", *J. Mater. Sci. Mater. Med.* **2001**, *12*, 761-766

[228] Matsushita, N.; Terai, H.; Okada,T.; Nozaki, K.; Inoue, H.; Miyamoto, S.; Takaoka, K. *J "*A new bone-inducing biodegradable porous beta-tricalcium phosphate", *Biomed Mater Res*. **2005**, *70A*, 450-458

[229] Sun, J.S.; Lin, F. H.; Wang, Y. J.; Huang, Y. C.; Chueh, S. C.; Hsu, F. Y. "Collagen-Hydroxyapatite/Tricalcium Phosphate Microspheres as a Delivery System for Recombinant Human Transforming Growth Factor-β 1", *Artificial Organs*, **2003**,27, 605

[230] Figge, J., Rossing, T. H. and Fencl, V., "The total serum proteins in acid-base equilibria", *J. Lab. Clin. Med.,* **1991**, 117, 453-467

[231] Peters, T. Jr. "Serum Albumin", *Adv. Protein Chem.*37; **1985**, 161-245

[232] Patterson, J.E., and Geller, D.M., "Bovine microsomal albumin: amino terminal sequence of bovine proalbumin", *Biochem. Biophys. Res. Commun.* **1977**, 74, 1220-1226

[233] He, X. M. and Carter, D. C., "Atomic structure and chemistry of human serum albumin", *Nature,* **1992**, 358, 209-215

[234] McGillivray, R.T.A., Chung, D.W. and Davie, E.W, "Biosynthesis of bovine plasma proteins in a cell-free system. Amino-terminal sequence of preproalbumin"; *Eur. J. Biochem.,* **1979***,* 98, 477-485

[235] Peters, T. Jr, "Evidence of intermediate compounds in serum albumin synthesis", *J Biol Chem*. **1953**; 200(1):461-470.

[236] Foster, J. F., In "*Albumin Structure, Function and Uses*" (V. M. Rosenoer, M. Oratz, and M. A. Rothschild, eds), **1977**, 53, Pergamon, Oxford.

[237] Rezwan, K., Studart, A.R., Vo1ro1s, J. Gauckler, L. J. "Change of ζ Potential of Biocompatible Colloidal Oxide Particles upon Adsorption of Bovine Serum Albumin and Lysozyme.", *J. Phys. Chem. B***. 2005**, 109*,* 14469 -14474

[238] Tse-Ying Liu, San-Yuan Chen, Dean-Mo Liu, Sz-Chian Liou. "On the study of BSA-loaded calcium-deficient hydroxyapatite nano-carriers for controlled drug delivery", *Journal of Controlled Release,* **2005**,107, 112–121

[239] Yaowalak Boonsongrit, Hiroya Abe, Kazuyoshi Sato, Makio Naito, Masahiro Yoshimura, Hideki Ichikawa, Yoshinobu Fukumori. "Controlled release of bovine serum albumin from

hydroxyapatite microspheres for protein delivery system", *Materials Science and Engineering B*, **2008**, 148, 162–165

[240] D. Magne, P. Pilet, P. Weiss, G. Daculsi, "Fourier transform infrared microspectroscopic investigation of the maturation of nonstoichiometric apatites in mineralized tissues: a horse dentin study", *Bone*, **2001**, 29 (6), 547-552

[241] G.Daculsi, R. Z. LeGeros and D. Mitre, "Crystal dissolution of biological and ceramic apatites", **2007**, 45 (2), 95-103

[242] A.H. Shankar and A.S. Prasad, Zinc and immune function, the biological basis of altered resistance to infection, *Am J Clin Nutr*,**1998**,. 68**,** 447–463.

[243] Kanzaki N, Onuma K, Treboux G, Tsutsumi S, Ito A. Inhibitory effect of magnesium and zinc on crystallization kinetics of hydroxyapatite (0 0 0 1) face. J Phys Chem B **2000**, 04, 4189–4194.

[244] Natascha Brandes, Petra B. Welzel, Carsten Werner, Lothar W. Kroh Adsorption-induced conformational changes of proteins onto ceramic particles: Differential scanning calorimetry and FTIR analysis. *Journal of Colloid and Interface Science*, **2006**, 299, 56-69

[245] Baron R, Neff L, Louvard D, Courtoy PJ, "Cell-mediated extracellular acidification and bone resolution", *J Cell Biol*, **1985**; 101:2210–2222.

[246] Baron R.,"Molecular mechanism of bone resolution by osteoclast", *Anat Rec*, **1989**, 224, 317–324.

[247] J. S. Bow, S. C. Liou, S. Y. Chen, "Structural characterization of room-temperature synthesized nano-sized *β*-tricalcium phosphate" *Biomaterials*, **2004**, 25, 3155-3161

[248] M. Vallet-Regı, J. Pena, Izquierdo-Barba, I., "Synthesis of β-tricalcium phosphate in layered or powdered forms for biomedical applications", *Solid State Ionics*, **2004**, 172, 445-449

[249] Karen Fu, Kai Griebenow, Lisa Hsieh, Alexander M. Klibanov , Robert Lang, "FTIR characterization of the secondary structure of proteins encapsulated within PLGA microspheres", *Journal of Controlled Release*, **1999**, 58, 357–366

[250] Tatsuo Maruyama, Shinji Katoh, Mitsutoshi Nakajima, Hiroshi Nabetani, Thomas P. Abbott, Atsushi Shono and Kazumi Satoh, "FT-IR analysis of BSA fouled on ultrafiltration and microfiltration membranes", *Journal of Membrane Science*, **2001**, 192, (1-2), 201-207

[251] I. Mayer, H. Cohen , J.C. Voegel, F.J.G. Cuisinier, Synthesis, characterization and high temperature analysis of Al-containing hydroxyapatites. *Journal of Crystal Growth*, **1997**, 172, 219-225

[252] Cullity BD.Elements of X-ray diffraction, 2nd ed.Reading, MA: Addison-Wesley; 1978

[253] *International Centre for Diffraction Data.* Calcium phosphate hydroxide.Card No. 09-0432, Joint Committee on Powder Diffraction Standards, Newtown Square, NJ, **1998**

[254] Laurence C. Chow, Limin Sun,"Properties of Nanostructured Hydroxyapatite Prepared by a Spray Drying Technique", *J. Res. Natl. Inst. Stand. Technol*., **2004**, 109, 543-551

[255] J. Thomas Webster, A. Elizabeth, Massa-Schlueter, Jennifer L. Smith, B. Elliot Slamovich, "Osteoblast response to hydroxyapatite doped with divalent and trivalent cations", *Biomaterials*, **2004**, 25, 2111-2121

[256] Suzuki T, Hatsushika T, Hayakawa Y., "Synthetic hydroxyapatites employed as inorganic cation-exchangers", *J Chem Soc Faraday Trans*, **1981**, 77, 1059–1062.

[257] K.Ohta, H.Monma, J.Tanaka, H.Eda "Interaction between hydroxyapatite and proteins by liquid chromatography using simulated body fluids as eluents", *Journal of Materials Science: Materials in Medicine*, **2002**, 13 (7), 633-637

[258] K. Kandori, M. Saito, H. Saito, A. Yasukawa, T. Ishikawa, "Adsorption of protein on non-stoichiometric calcium–strontium hydroxyapatite", *Colloids Surf, A Physicochem. Eng.Asp*, **1995**, 94, 225–230.

[259] V. Hlady, H. Furedi-Milhofer, Absorption of HAS on precipitated hydroxyapatite, *J. Colloid Interface Sci*., **1979**, 69 460– 467.

[260] T. Matsumoto, M. Okazaki, M. Inoue, Y. Hamada, M. Taira, J. Takahashi, Crystallinity and solubility characteristics of hydroxyapatite adsorbed amino acid, *Biomaterials*, **2002**, 23 2241– 22

[261] CA van Blitterswijk, JJ Grote, W Kuypers, CJG Blok-van Hoek and WTh Daems, Bioreactions at the tissue/hydroxyapatite interface. *Biomaterials* , **1985**, 6**,** 243–251

[262] Nery EB, LeGeros RZ, Lynch KL, Lee K, "Tissue response to biphasic calcium phosphate ceramic with different ratios of HA/ β-TCP in periodontal osseous defects", *J Periodontol*, **1992**; 68, 729 –735.

[263] M. Jarcho , "Retrospective analysis of hydroxyapatite development for oral implant applications", *Dent. Clin. North Am.,* **1992,** 36, 19 -26

[264] Groot K de. Bioceramics consisting of calcium phosphate salts. Biomater, **1980**, 1, 47-50.

[265] Lin FH, Lin CC, Lu HC, Huang YY, Wang CY, Lu CM. Sintered porous DP-bioactive glass and hydroxyapatite as bone substitute. *Biomaterials*, **1984**;15**,** 1087-1098

[266] J. Dumbleton, M. T. Manley, "Hydroxyapatite-Coated Prostheses in Total Hip and Knee Arthroplasty ", *J. Bone Joint Surg. Am.* A, **2004**, 86**,** 2526 -2540

[267] C. A. Van Blitterswijk, J. J. Grote ,W. Kuypers, W. T. H. Daems and K. de Groot "Macropore tissue ingrowth: a quantitative and qualitative study on hydroxyapatite ceramic", *Biomaterials,* **1986, 7,** 137 -143

[268] M.A. Meyers, A. Mishra, D.J. Benson, "Mechanical properties of nanocrystalline materials", *Progress in Materials Science*, **2006**, 51, 427–556

[269] S. A. Catledge, M. D. Fries,Y. K. Vohra , W. R. Lacefield ,J. E. Lemons, S. Woodard, R. Venugopalan, "Mechanical Properties and Microarchitecture of Nanoporous Hydroxyapatite Bioceramic Nanoparticle Coatings on Ti and TiN", *J. Nanosci. Nanotechnol ,* **2002, 2,** 293-297

[270] Masanori Adachi, Nobukazu Wakamatsu,Yutaka Doi, " Superplastic Deformation In Carbonate Apatite Ceramics Under Constant Compressive Loading for Near-Net-Shape Production of Bioresorbable Bone Substitutes", Dental Materials Journal, **2008**, 27(1), 93-98

[271] Chen IW, Wang XH., "Sintering dense nanocrystalline ceramics without final-stage grain growth", *Nature*, **2000**, 404, 168–171.

[272] Bykov Y, Eremeev A, Egorov S, Iranov V, Khrustov Y, Sorokin A., "Sintering of nanostructural titanium oxide using millimeterwave radiation", *Nanostruct Mater*, **1999**;12,115–118.

[273] Lee YI, Lee J-H, Hong S-H, Kim D-Y. "Preparation of nanostructured TiO_2 ceramics by spark plasma sintering", *Mater Res Bull*, **2003**, 38, 925–930.

[274] Shen Z, Peng H, Liu J, Nygren M., "Conversion from nano- to micron-sized structures: experimental observations", *J Eur Ceram Soc*, **2004**, 24, 3447–3452.

[275] Anselme K. "Osteoblast adhesion on biomaterials", *Biomaterials*, **2000**, 21, 667–681.

[276] Anderson Jm, Gristina AG, Hanson SR, Harker LA, Johnson RJ, Merritt K, Naylor PT, Schoen FJ., "Host reactions to biomaterials and their evaluation", In: Ratner BD, Hoffman AS, Schoen FJ, Lemons JE, editors. Biomaterials Science: *An Introduction to Materials in Medicine*. London: Academic Press; **1996**, p 165–214

[277] Deligianni DD, Katsala ND, Koutsoukos PG, Missirlis YF., "Effect of surface roughness of hydroxyapatite on human bone marrow cell adhesion, proliferation, differentiate and detachment strength", *Biomaterials*, **2001**, 22, 87–96.

[278] J.E Hilliard, "Estimating grain size by the intercept method", *Metal Progr*, **1964**, 85, 99-102

[279] Anstis GR, Chantikul P, Lawn BR, Marshall DB., "A critical evaluation of indentation techniques for measuring fracture toughness: I, direct crack measurement", *J Am Ceram Soc*, **1981**, 64, 533

[280] J.L. Li, L.J. Wang, G.Z. Bai and W. Jiang, "Microstructure and mechanical properties of in situ produced TiC/C nanocomposite by spark plasma sintering", *Scripta Materialia*, **2005**, 52 (9), 867-871

[281] C. J. van Oss, R.F. Giese Jr and R. J. Good, "Reevaluation of the Surface Tension Components and Parameters of Polyacetylene from Contact Angles of Liquids", *Langmuir,* **1990**, 6, 1711-1713

[282] J. J. Bozzola and R. D. Lonnie, *Electron Microscopy: Principles and Techniques for Biologists*.edited Jones and Bartelett Publishers, Boston, **1992**.

[283] W. Xu, H. Baribault, E. D. Adamson, "Vinculin knockout results in heart and brain defects during embryonic development. *Development* ", *Biomaterials,* **1998**, 125, 327 -327

[284] D. Rokusek, C. Davitt, A. Bandyopadhyay, S. Bose and H.L. Hosick, "Interaction of human osteoblasts with bioinert and bioactive ceramic substrates", *J. Biomed*. *Mater. Res,* **2005**, *75A*, 588-594

[285] J. E. Aubin, F. Liu, The osteoblast lineage, In; J.P Bilezikian , L. G Raisz , G. A. Rodan, editors. *Principles of Bone Biology.* San Diego: Academic Press, **1996**, 51-95

[286] E. Zammir, B. Geiger, "Molecular complexity and dynamics of cell-matrix adhesions", *J. Cell Science,* **2001**,114, 3583-3590